HYBRID APPROACHES TO MAGNETIC RESONANCE THERMOMETRY USING THE PROTON RESONANCE FREQUENCY SHIFT AND THE SPIN-LATTICE RELAXATION TIME T_1

by

Mahamadou Diakité

A dissertation submitted to the faculty of
The University of Utah
in partial fulfillment of the requirements for the degree of

Doctor of Philosophy

in

Physics

Department of Physics and Astronomy

The University of Utah

December 2013

The University of Utah Graduate School

STATEMENT OF DISSERTATION APPROVAL

The dissertation of Mahamadou Diakité

has been approved by the following supervisory committee members:

Brian T. Saam	, Chair	6/20/2013 Date Approved
Dennis L. Parker	, Member	6/20/2013 Date Approved
Eun-Kee Jeong	, Member	6/20/2013 Date Approved
Eugene Mishchenko	, Member	6/24/2013 Date Approved
Wayne Springer	, Member	6/25/2013 Date Approved

and by David B. Kieda , Chair/Dean of

the Department/College/School of Physics and Astronomy

and by David B. Kieda, Dean of The Graduate School.

ABSTRACT

Minimally invasive thermal therapy under Magnetic Resonance Imaging (MRI) guidance is becoming popular with several applications in the process of getting FDA approval. The ability to determine in near real-time the temperature map of a tumor and its surrounding tissue makes MR thermometry very attractive and well suited for thermal treatment. The proton resonance frequency shift (PRF) is currently the gold standard method for temperature monitoring using MRI. However, its incapacity to measure temperature in fatty tissue limits the scope of its applicability. The spin lattice relaxation time T_1, on the other hand, has shown good temperature sensitivity and works well in all types of tissues.

In this dissertation, we have addressed a number of challenges currently affecting MRI thermometry. A non-CPMG Turbo Spin Echo (TSE) sequence has been implemented to monitor the temperature rise due to the high RF power deposition inherent to this sequence at high field (3T and higher). This new implementation allows TSE sequences to be used safely without altering their high contrast properties which make them appealing in clinical settings.

Tissue damage assessment during thermal therapy is critical for the safety of the patient. We have developed a new hybrid PRF-T_1 sequence that has the capability to provide simultaneously in near real-time the temperature map and T_1 information, which is a good indication of the state of the tissue. The simplicity and the real-time

capability of the newly developed sequence make it an ideal tool for tissue damage assessment.

Temperature monitoring during thermal therapy in organs with large fat content have been hindered by the lack of an MRI thermometry method that can provide simultaneous temperature in fat and aqueous tissue. A new sequence and acquisition scheme have been developed to address this issue.

In sum, this dissertation proposed several pulse sequence implementation techniques and an acquisition scheme to overcome some of the limitations of MR thermometry.

In memory of

Ibrahim Diakité

We will miss you! Forever….

CONTENTS

LIST OF TABLES

LIST OF FIGURES

LIST OF ACRONYMS

DC	Analog to Digital Converter
CEM	Cumulative Equivalent Minutes
CPMG	Call-Purcell-Meiboom-Gill
DFA	Double Flip Angle
DFT	Discrete Fourier Transform
Emf	Electromotrice Force
EPI	Echo Planar Imaging
ESWL	Extracorporeal Shockwave Lithotripsy
ETL	Echo Train Length
FA	Flip Angle
FID	Free Induction Decay
FOV	Field of View
FSE	Fast Spin Echo
FT^{-1}	Inverse Fourier Transform
FUS	Focused Ultrasound Surgery
GRAPPA	Generalized Autocalibrating Partially Parallel Acquisitions
GRE	Gradient Recall Echo
IGT	Image Guided Therapy
IR	Inversion Recovery
MRA	Magnetic Resonance Angiography
MRgHIFU	Magnetic Resonance guided High Intensity Focus Ultrasound

MRI	Magnetic Resonance Imaging
MRM	Magnetic Resonance in Medicine
MS	Multiple Sclerosis
MT	Magnetization Transfer
NMR	Nuclear Magnetic Resonance
PAT	Parallel Acquisition Technique
PD	Proton Density
PPM	Parts per Million
PRF	Proton Resonance Frequency
PSD	Phase-Sensitive Detection
RARE	Rapid Acquisition with Relaxation Enhancement
RF	Radio Frequency
ROI	Region of Interest
SAR	Specific Absorption Rate
SE	Spin Echo
SI	Signal Intensity
SLR	Shinnar-Le Roux
SNR	Signal to Noise Ratio
SOS	Sum of Squares
SPGR	Spoiled Gradient Echo
SR	Saturation Recovery
TE	Echo Time
TI	Inversion Time
TR	Repetition Time
TSE	Turbo Spin Echo
VFA	Variable Flip Angle

ACKNOWLEDGEMENTS

I would like to take this opportunity to express my deep gratitude and respect to my thesis and research advisor, Professor Dennis L. Parker. He has helped me become an independent scientist and inspired me every day through his hard work while I was a PhD student.

My sincere thanks must also go to the members of my thesis committee: Professor Brian T. Saam, Professor Eun-kee Jeong, Professor Wayne Springer, and Professor Eugene Mishchenko for generously taking their time to offer comments and suggestions to improve my work.

This thesis would not have been possible without the help of my colleagues on the HIFU team, namely Dr Nick Todd, Dr Allison Payne, Henrick Odéen, Yi Wang, Josh Coon, and Josh De Bever. I would like also to express my sincere gratitude to everybody at the Advanced Center for Imaging Research (UCAIR) who has contributed in one way or another to this thesis and all my friends. A particular thanks goes to Jackie Hadley from the physics department for her constant support and encouragement during all these years.

Finally, there are no right words to convey my deep and sincere gratitude to my family: my mom, my dad, my sister, and my beloved late brother. Thank you for your unconditional support.

CHAPTER I

PRINCIPLES OF MAGNETIC RESONANCE IMAGING

1.1 Introduction

Temperature monitoring of minimally invasive therapeutic intervention under Magnetic Resonance Imaging (MRI) guidance has been under active investigation for nearly two decades (1,2). The noninvasive nature of MRI in conjunction with the lack of ionizing radiation and the ability to image in any orientation with high spatial and temporal resolution make it one of the potentially attractive modality for real-time feedback thermal therapy. Since the infancy of temperature monitoring under MRI guidance, various MR parameters have been investigated for their temperature dependence such as: the proton density (3-5), the spin lattice relaxation time T_1 of the water proton (2,6-13), the spin-spin relaxation time T_2 of the water proton (14,15), the diffusion coefficient which describes the thermal Brownian motion of molecules in a medium (16-19), the magnetization transfer (20,21), and the proton resonance frequency (PRF) shift of the water proton (22-27). Chapter 2 gives a brief overview of some of the thermometry methods, but for more detailed description of these temperature measurement techniques and other historical milestones of MRI temperature monitoring, the reader is referred to the review by Rieke et al. (28) and Quesson et al. (29). Although these techniques have shown their capabilities of measuring the temperature during thermal exposure, they present individually some potential limitations

in terms of their temperature sensitivity (accuracy), their temporal resolution, and their tissue dependence. In fact, adequate temperature monitoring requires that the MR temperature maps have spatial resolution to accurately measure the induced temperature distribution, high temporal resolution to track changes in regions where the temperature is rapidly increasing, sufficient volume coverage to image everywhere where thermal energy may be deposited, and their applicability to all kinds of biological specimens.

Among the MRI temperature measurement techniques listed above, the PRF and the T_1 techniques have emerged as leading approaches because of their reliability, their relative high temporal and spatial resolutions, and their ease of implementation. Furthermore, combining PRF and T_1 can be used to overcome some of the limitations of the individual techniques such as PRFs incapacity to measure temperature in fat, which poses significant problems for treatment of organs that contain large amounts of fat such as breast and skin. However, the temperature sensitivity of T_1 has been measured for a number of fatty tissues, and has been found to be approximately linear with the temperature (15,30). Similarly T_1 of the tissue, which is related to the translational and rotational rates of water, can be used as an intrinsic probe for investigating structural change in tissue at high temperature.

Therefore, the goal of this dissertation is to present novel pulse sequence implementations and new acquisition schemes to overcome some of the limitations of the PRF and the T_1 techniques. Also, the spatial resolution and the temporal resolution have been improved for the 3D volume coverage during MR temperature imaging. The outline of the chapters of this dissertation is presented as follows:

- The remainder of Chapter 1 is an overview of the basic concepts of nuclear magnetic resonance (NMR) and the principle of magnetic resonance imaging. First, the

quantum mechanical description of atomic nuclei is presented from the description of a spin in a static field to Bloch equations. Then, the classical treatment is used to describe the MRI theory.

- Chapter 2 is focused on MR thermometry methods; particularly a general overview of the PRF and T_1 temperature measurement techniques are described. Special attention is paid to the acquisition and the implementation of these techniques as well as their capabilities and limitations.
- Chapter 3 is devoted to the basic concepts of High-Intensity Focused Ultrasound (HIFU). The theories (physic) of the propagation of the sound wave in conjunction with the biological effect of HIFU are presented.
- Chapter 4 demonstrates the feasibility of the PRF-based thermometry using a modified turbo spin echo sequence. This simple sequence modification allows any turbo spin echo sequence to be used safely and prevents the temperature change due to the Specific Absorption Rate (SAR) to exceed a threshold temperature set by the user of this sequence.
- Chapter 5 introduces the results of the irreversible change in the T_1 temperature dependence with thermal dose using the PRF-T_1 technique. The results demonstrate that the change of spin lattice relaxation time T_1 is reversible with temperature for low thermal dose (thermal dose $\leq$ 240 cumulative equivalent minutes [CEM] 43°C) and irreversible with temperature after significant accumulation of thermal dose in ex vivo chicken breast tissue. They also suggest that the hybrid PRF-T_1 method may be a potentially powerful tool to investigate the extent and mechanism of heat damage of biological tissues.

- In Chapter 6, a new approach for simultaneous PRF temperature mapping in aqueous tissue and T_1 mapping in fat is described. These results represent a step forward toward real-time temperature monitoring during thermal therapy in organs that contain large amounts of fat such as breast.
- Finally, Chapter 7 presents a summary of this dissertation and proposes new directives and suggestions for future works.

1.2 Overview of NMR Physics and Imaging

1.2.1 Historical Perspectives of MRI

The concept of nuclear magnetic resonance has its origins in the discovery of the spin nature of the proton. Based on the work of Stern and Gerlach from the early 1920s, Rabi and its group worked on the spin of the proton and its interaction with a magnetic field in the 1930s (31). With the basic understandings in hand in 1946, Felix Bloch and Edward Purcell extended independently the early quantum mechanical concepts to a measurement of an effect of the precession of the spins around a magnetic field. They explained many of the theoretical and experimental details of NMR as we know them today. For this work, they shared the Nobel Prize in physics in 1952.

However, it could be argued that MRI had its real beginnings in 1973 with the publication of the seminal papers by Paul Lauterbur (32) and Peter Mansfield (33). They proposed and showed that the difference in frequency components of the signal could be separated to give spatial information about the object. They were awarded the Nobel Prize in Medicine for their discoveries in 2003. Furthermore, Raymond Damadian (1971) brought the attention to the tumors' detection by noting the difference in relaxation times between

healthy tissues and tumors (34). Later, a Swiss physical chemist Richard R. Ernst proposed a technique that enables high-resolution 2D study of larger molecules. With its refinement, many others scientists extended its work by proposing 2D (35), and eventually 3D Fourier imaging methods. He earned the Nobel Prize in Chemistry in 1991 for his work in Fourier transform NMR spectroscopy. MRI had therefore begun. The whole body MRI was demonstrated by Raymond Damadian in 1977. For more historical and review references, the reader is referred to the Encyclopedia of Nuclear Magnetic Resonance (Volume 1, Historical Perspectives).

Since then, MRI has been a successful imaging modality due to its ability to noninvasively acquire high-resolution images of the internal structure of subjects without the use of ionizing radiation. Furthermore, many improvements have been made in the MRI field; from the hardware to the software and different acquisition schemes have been developed to increase the spatial and temporal resolution of the images. The next section gives both quantum and classical description of NMR physics from the simple resonance theory to the signal formation and detection.

1.2.2 Quantum Mechanical Description

It is possible to use either the quantum or the classical description of the resonance phenomena. In general, all substances are magnetic; therefore, they do have the capacity to interact with magnetic fields. The interaction energy is expressed in function of the nuclear magnetic moment $\vec{\mu}$. The Hamiltonian is given by:

$$\mathcal{H} = -\vec{\mu} \cdot \vec{B} \qquad [1.1]$$

where $\vec{B}$ is the applied external magnetic field. A fundamental symmetry theorem (Wigner-Eckart theorem of quantum mechanics) requires that the intrinsic angular momentum $\vec{I}$ and the nuclear magnetic moment are proportional to each other:

$$\vec{\mu} = \gamma \vec{I} \qquad [1.2]$$

The proportionality constant γ is called the magnetogyric ratio (also called the gyromagnetic ratio). The gyromagnetic ratio is specified in unit of $\left[\frac{\text{rad}}{\text{s}\cdot\text{T}}\right]$. Note that γ can be either positive or negative and its values are established experimentally. In Table 1.1 are given the values of γ for selected nuclei.

Furthermore, Pieter Zeeman, a Dutch physicist, in 1897 has demonstrated in a seminal paper that any spin state of the nucleus with quantum number $\vec{I}$ may be represented as a superposition of the 2I+1 eigenstates $|\text{I}, \text{m}\rangle$. Thus, the Zeeman eigenstates $|\text{I}, \text{m}\rangle$ form a finite basis for the representation of the spin operator $\vec{I}$ with dimension 2I+1. This phenomenon is known as the Zeeman effect. Also, the nature of the Zeeman splitting depends critically on the strength of the applied external magnetic field B_{ext} in comparison to the internal field B_{int} that gives rise to spin-orbital coupling. If $\text{B}_{\text{ext}} \ll \text{B}_{\text{int}}$, then fine structure dominates, whereas if $\text{B}_{\text{ext}} \gg \text{B}_{\text{int}}$, then the Zeeman effect dominates. Therefore, for the remainder of this dissertation, we assume that $\text{B}_{\text{ext}} \gg \text{B}_{\text{int}}$.

Hence, by applying the magnetic field B_0 along the z-direction and using the Zeeman eigenstates $|\text{I}, \text{m}\rangle$ of $\vec{\text{I}}$, it follows:

$$\mathcal{H}|\text{I}, \text{m}\rangle = -\hbar\gamma B_0 m|\text{I}, \text{m}\rangle \qquad [1.3]$$

Table 1.1: Selected atomic nuclei common in human body with their gyromagnetic ratio and their spins.

Atomic Nucleus	Gyromagnetic ratio $\frac{\gamma}{2\pi}$ [MHz/T]	Spin quantum number
^{1}H	42.58	1/2
^{23}Na	11.27	3/2
^{31}P	17.25	1/2
^{17}O	-5.77	5/2
^{19}F	40.08	1/2

Therefore, the allowed energies are:

$$E_m = -\hbar\gamma B_0 m \qquad [1.4]$$

where $m = -I,\ -I+1, \ldots\ldots\ldots,\ I-1,\ I$ and $I = 0,\ \frac{1}{2}, 1,\ \frac{3}{2}, \ldots$

For simplicity, let us consider a system whose nuclei possess spin $\frac{1}{2}$. Hence, the energy levels and the eigenstates are given in Figure 1.1.

The Zeeman eigenstates are equally spaced and the energy difference between adjacent states is:

$$\Delta E = \hbar\gamma B_0 = \hbar\omega_0 \qquad [1.5]$$

where

$$\omega_0 = \gamma B_0 \qquad [1.6]$$

The fact that the resonance frequency is independent of Planck's constant suggests that the result is also describable by a classical picture.

In MRI, the magnetic resonance is usually produced by applying an alternating magnetic field perpendicular to the static field, B_0. Let us apply the alternating magnetic field as a

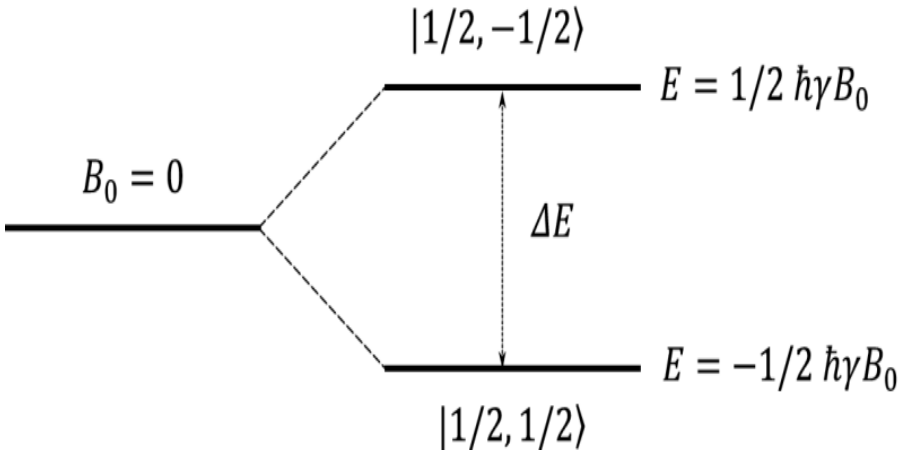

Figure 1.1: The Zeeman energy levels of a spin one-half system in an external magnetic field, B_0.

small perturbation along the x-direction. Therefore, the Hamiltonian is:

$$\mathcal{H}_1^x = -\hbar\gamma B_1^x I_x \cos(\omega t) \qquad [1.7]$$

Hence, the matrix element of the Hamiltonian is given by:

$$\langle I', \mathrm{m}'|\mathcal{H}_1^x|I, \mathrm{m}\rangle = -\hbar\gamma B_1^x cos\omega t \, \langle I', \mathrm{m}'|I_x|I, \mathrm{m}\rangle \qquad [1.8]$$

It is convenient at this point to introduce the "ladder operators" commonly known as the raising and lowering operators:

$$\begin{cases} I^+ = I_x + iI_y \\ I^- = I_x - iI_y \end{cases} \qquad [1.9]$$

where:

$$\begin{cases} I^+|I, \mathrm{m}\rangle = \sqrt{I(I+1) - m(m+1)}|I, \mathrm{m}+1\rangle \\ I^-|I, \mathrm{m}\rangle = \sqrt{I(I+1) - m(m-1)}|I, \mathrm{m}-1\rangle \end{cases} \qquad [1.10]$$

Solving for I_x in equation [1.9] one obtains:

$$I_x = \frac{1}{2}(I^+ + I^-) \qquad [1.11]$$

Hence, from the definition of the raising and lowering operator we obtain:

$$\langle I', \mathrm{m}'|\mathcal{H}_1^x|I, \mathrm{m}\rangle \qquad [1.12]$$
$$= -\frac{\hbar\gamma B_1^x cos\omega t}{2}\Big(\sqrt{I(I+1) - m(m+1)}\,\langle I', \mathrm{m}'|I, \mathrm{m}+1\rangle$$
$$+ \sqrt{I(I+1) - m(m-1)}\,\langle I', \mathrm{m}'|I, \mathrm{m}-1\rangle\Big)$$

Equation [1.12] vanishes unless **the selection rules** for *I* and m are satisfied:

$$\begin{cases} I = I' \\ \mathrm{m}' = \mathrm{m} \pm 1 \end{cases} \qquad [1.13]$$

Consequently, the allowed transitions are only between adjacent energy levels.

For $= \frac{1}{2}$, equation [1.12] reduces to :

$$\left\langle \frac{1}{2}, -\frac{1}{2}\middle|\mathcal{H}_1^x\middle|\frac{1}{2}, \frac{1}{2}\right\rangle = -\frac{\hbar\gamma B_1^x cos(\omega t)}{2} \qquad [1.14]$$

From the time-dependent perturbation theory, one can derive the probability per second $\left(P_{|\frac{1}{2},-\frac{1}{2}\rangle\to|\frac{1}{2},\frac{1}{2}\rangle}\right)$ that $\mathcal{H}_1^x$ induces a transition from a state $|\frac{1}{2}, -\frac{1}{2}\rangle$ to a state $|\frac{1}{2}, \frac{1}{2}\rangle$.

$$P_{|\frac{1}{2},-\frac{1}{2}\rangle\to|\frac{1}{2},\frac{1}{2}\rangle} = \frac{2\pi}{\hbar}\left|\left\langle \frac{1}{2}, -\frac{1}{2}\middle|\mathcal{H}_1^x\middle|\frac{1}{2}, \frac{1}{2}\right\rangle\right|^2 \delta\left(E_{|\frac{1}{2},-\frac{1}{2}\rangle} - E_{|\frac{1}{2},\frac{1}{2}\rangle} - \hbar\omega\right) \qquad [1.15]$$

Equation [1.15] reduces to:

$$P_{|\frac{1}{2},-\frac{1}{2}\rangle\rightarrow|\frac{1}{2},\frac{1}{2}\rangle} = \frac{\pi}{2}\left(\gamma B_1^x cos(\omega t)\right)^2 \delta(\omega_0 - \omega) \qquad [1.16]$$

Therefore, the transition probability vanishes unless the perturbation field is tuned exactly to ω_0. Hence, the resonance phenomenon occurs only if the applied magnetic field B_1^x perpendicular to the static magnetic field B_0 is tuned to the frequency $\omega_0 = \gamma B_0$. This resonance frequency is known as Larmor frequency.

1.2.3 Classical Description

Classical treatment usually describes the macroscopic behavior of the fundamental constituents of the matter. Atoms with an odd number of protons or neutrons possess a nuclear magnetic moment $\vec{\mu}$, and therefore exhibit the magnetic resonance phenomenon. A classical argument for the existence of $\vec{\mu}$ is twofold:

a) A nucleus such as a proton has an electrical charges *e* and a mass *m*.

b) It rotates around its own axis if it has nonzero spin. Therefore, it creates a magnetic field around itself that is analogue to the field surrounding a microscopic bar magnet.

The magnitude of this magnetic moment can be computed in a straightforward manner as described below.

For simplicity, let us assume the charge *e* is moving in circular path of radius *r* with period T. The system can be treated as a current loop of area *A* and carrying current *i*, thus:

$$\mu = iA \qquad [1.17]$$

Since $i = \frac{e}{cT}$, we get:

$$\mu = \frac{e\pi r^2}{cT} \qquad [1.18]$$

Furthermore, by using the fundamental relationship of particle physics: $\mu = \gamma J$ where the classical angular momentum can be derived as:

$$J = mvr = m\frac{2\pi r^2}{T} \qquad [1.19]$$

and comparing the expression of μ and J, one obtains: $\gamma = \frac{e}{2mc}$. This expression of γ shows that the gyromagnetic ratio varies in function of the charge and the mass of the nuclei under investigation, as previously shown in Table 1.1.

Now, let us describe the collective behavior of an ensemble of N_I spins placed in an external strong magnetic field B_0 applied along the z-direction. For simplicity, we will be considering a nucleus whose spin is $\frac{1}{2}$.

Consider $\overrightarrow{M}$, a macroscopic magnetization vector such as:

$$\overrightarrow{M} = \sum_{n=1}^{N_I} \vec{\mu}_n = \left(\sum_{n=1}^{N_I} \mu_n^x\right)\vec{\imath} + \left(\sum_{n=1}^{N_I} \mu_n^y\right)\vec{\jmath} + \left(\sum_{n=1}^{N_I} \mu_n^z\right)\vec{k} \qquad [1.20]$$

where μ_n^x, μ_n^y and μ_n^z are the projections of $\vec{\mu}_n$ along the axis of the Cartesian coordinate system $(\vec{\imath}, \vec{\jmath}, \vec{k})$. Note that $\overrightarrow{M} = 0$ in the absence of an external magnetic field because of the random orientation of the microscopic magnetic moments. In equation [1.20], the transverse components add to zero because of their random phase while $\overrightarrow{M}$ precesses about the z-axis. Hence, equation [1.20] reduces to:

$$\overrightarrow{M} = \left(\sum_{n=1}^{N_I} \mu_n^z\right)\vec{k} \qquad [1.21]$$

Based on the quantum mechanical description of the previous section, it has been shown that a system of N_I spins in an external magnetic field B_0 can take one of two possible orientations with respect to the z-axis. The energy difference between the two quantum states $\left(|\frac{1}{2},-\frac{1}{2}\rangle, |\frac{1}{2},\frac{1}{2}\rangle\right)$ is:

$$\Delta E = E_{|\frac{1}{2},-\frac{1}{2}\rangle} - E_{|\frac{1}{2},\frac{1}{2}\rangle} = \hbar\omega_0 \qquad [1.22]$$

(see equation [1.5]).

However, the Boltzmann relationship relates the spin population difference of the two spin states to their energy difference:

$$\frac{N_{|\frac{1}{2},\frac{1}{2}\rangle}}{N_{|\frac{1}{2},-\frac{1}{2}\rangle}} = exp\left(\frac{\Delta E}{k_B T}\right) \qquad [1.23]$$

where

$N_{|\frac{1}{2},\frac{1}{2}\rangle}$: number of spins in the state $|\frac{1}{2},\frac{1}{2}\rangle$

$N_{|\frac{1}{2},-\frac{1}{2}\rangle}$: number of spins in the state $|\frac{1}{2},-\frac{1}{2}\rangle$

k_B: Boltzmann constant ($1.38\cdot10^{-23}JK^{-1}$)

T: Absolute temperature of the spin system

In practice, $\Delta E \ll k_B T$ (high-temperature approximation); therefore, the right side of equation [1.23] can be expanded in power series and one can consider only the first two terms:

$$\frac{N_{|\frac{1}{2},\frac{1}{2}\rangle}}{N_{|\frac{1}{2},-\frac{1}{2}\rangle}} \approx 1 + \frac{\hbar\omega_0}{k_B T} \qquad [1.24]$$

Hence,

$$N_{|\frac{1}{2},\frac{1}{2}\rangle} - N_{|\frac{1}{2},-\frac{1}{2}\rangle} \approx N_I \frac{\hbar\omega_0}{2k_B T} \quad [1.25]$$

Equation [1.21] can be thus expressed in function of the magnetic moments of the two spins population as:

$$\vec{M} = \left(\sum_{n=1}^{N_I} \mu_n^z\right)\vec{k} = \left(\sum_{n=1}^{N_{|\frac{1}{2},\frac{1}{2}\rangle}} \frac{1}{2}\gamma\hbar - \sum_{n=1}^{N_{|\frac{1}{2},-\frac{1}{2}\rangle}} \frac{1}{2}\gamma\hbar\right)\vec{k} \quad [1.26]$$

$$= \frac{1}{2}\left(N_{|\frac{1}{2},\frac{1}{2}\rangle} - N_{|\frac{1}{2},-\frac{1}{2}\rangle}\right)\gamma\hbar\vec{k}$$

Therefore at equilibrium, the bulk magnetization vector is oriented parallel to the z-axis and points in the same direction and its magnitude is:

$$|\vec{M}| = \frac{\gamma^2\hbar^2 B_0 N_I}{4k_B T} \quad [1.27]$$

This result can be generalized to any nucleus with spin s as follows:

$$|\vec{M}| = \frac{\gamma^2\hbar^2 B_0 N_I I(I+1)}{3k_B T} \quad [1.28]$$

At this point, we assume that the spin system has reached the thermal equilibrium and the bulk magnetization is represented by $\overrightarrow{|M|} = M_0^z$.

The time-dependent behavior of the bulk magnetization in the presence of an applied magnetic field $B_1(t)$ perpendicular to the static magnetic field B_0 is well described quantitatively by the Bloch equation.

1.2.4 Bloch Equation

Bloch's equation describes the motion of a magnetization within an external magnetic field as well as the relaxation phenomena. The general form of Bloch's equation is given by:

$$\frac{d\vec{M}}{dt} = \vec{M} \times \gamma\vec{B} - \frac{M_x\vec{\imath} + M_y\vec{\jmath}}{T_2} - \frac{(M_z - M_0^z)}{T_1}\vec{k} \qquad [1.29]$$

where T_1 and T_2 are time constants characterizing the relaxation process of a spin system after it has been disturbed from its thermal equilibrium state and $\vec{B}$ includes the various magnetic fields applied. In the present discussion, we are interested only in the behavior of $\vec{M}$ during the application of an external magnetic field $B_1(t)$. Hence, we will drop the last two terms of equation [1.29] for now. Note that this treatment is also valid when the duration of the radio frequency (RF) is short compared to T_1 and T_2. Therefore, equation [1.29] takes a simpler form:

$$\frac{d\vec{M}}{dt} = \vec{M} \times \gamma\vec{B} \qquad [1.30]$$

To fully take advantage of this equation, let us rewrite the above equation in the rotating frame. Let us consider two reference frames: a stationary reference frame or laboratory reference frame $(\vec{\imath}, \vec{\jmath}, \vec{k})$ and a rotating reference frame $(\vec{\imath'}, \vec{\jmath'}, \vec{k'})$ about the z-axis with an angle (ωt) (see Figure 1.2).

The rotating frame can be expressed in function of the stationary frame as follows:

$$\begin{cases} \vec{\imath'} = \cos(\omega t)\,\vec{\imath} - \sin(\omega t)\,\vec{\jmath} \\ \vec{\jmath'} = \sin(\omega t)\,\vec{\imath} + \cos(\omega t)\,\vec{\jmath} \\ \vec{k'} = \vec{k} \end{cases} \qquad [1.31]$$

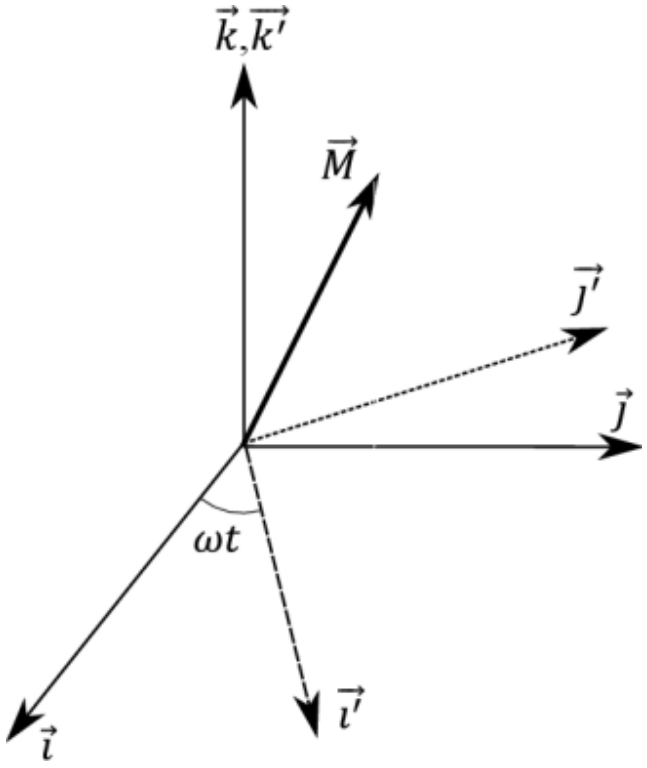

Figure 1.2: Rotation about the z-axis.

Thus, the time derivatives of the unit vector of the rotating frame are given by:

$$\begin{cases} \frac{\mathrm{d}\vec{\imath'}}{\mathrm{dt}} = -\omega\vec{k} \times \vec{\imath'} \\ \frac{\mathrm{d}\vec{J'}}{\mathrm{dt}} = -\omega\vec{k} \times \vec{J'} \\ \frac{\mathrm{d}\vec{k'}}{\mathrm{dt}} = -\omega\vec{k} \times \vec{k'} \end{cases} \quad [1.32]$$

The vector $\vec{\mathrm{M}}$ on Figure 1.2 can be decomposed in its scalar components in the two reference frames as follows:

$$\vec{M} = M_x\vec{\imath} + M_y\vec{J} + M_z\vec{k} \quad [1.33]$$

$$\vec{M} = \vec{M}_{rot} = M_x\vec{\imath'} + M_y\vec{J'} + M_z\vec{k'} \quad [1.34]$$

According to equations [1.32], the time derivative of the $\vec{M}$ vector in the rotating frame can be written as:

$$\frac{d\vec{M}_{rot}}{dt} = \frac{dM_{x'}}{dt}\vec{\imath}' + \frac{dM_{y'}}{dt}\vec{J}' + \frac{dM_{z'}}{dt}\vec{k}' + M_{x'}\frac{d\vec{\imath}'}{dt} + M_{y'}\frac{d\vec{j}'}{dt} + M_{z'}\frac{d\vec{k}'}{dt} \qquad [1.35]$$

$$= \frac{\partial \vec{M}_{rot}}{\partial t} - \omega\vec{k} \times \vec{M}_{rot}$$

Hence:

$$\frac{\partial \vec{M}_{rot}}{\partial t} = \gamma\vec{M}_{rot} \times \vec{B}_{rot} + \omega\vec{k} \times \vec{M}_{rot} = \gamma\vec{M}_{rot} \times \left(\vec{B}_{rot} - \frac{\omega}{\gamma}\vec{k}\right) \qquad [1.36]$$

We may rewrite equation [1.36] as:

$$\frac{\partial \vec{M}_{rot}}{\partial t} = \gamma\vec{M}_{rot} \times \vec{B}_{eff} \qquad [1.37]$$

$\vec{B}_{eff}$ is the effective magnetic field that the net magnetic moment (bulk magnetization vector) experiences in the rotating frame. The explicit form of this effective field is given by:

$$\vec{B}_{eff} = \left(B_0 - \frac{\omega}{\gamma}\right)\vec{k}' + B_1(t)\vec{\imath}' \qquad [1.38]$$

On resonance $\omega = \gamma B_0$; thus, the first term of equation [1.38] vanishes. Therefore, $\vec{B}_{eff}$ points in the direction of the $\vec{\imath}'$ unit vector. Equation [1.37] becomes:

$$\frac{\partial \vec{M}_{rot}}{\partial t} = \gamma\vec{M}_{rot} \times B_1(t)\vec{\imath}' \qquad [1.39]$$

The solutions of the above equation show that the bulk magnetization vector in the presence of a rotating RF field is forced to rotate around the axis of the RF field with angular velocity: $\vec{\omega} = -\gamma \vec{B}_1$.

1.2.5 Relaxation Times

When an ensemble of spins is exposed to an external static magnetic field for a long time, the spin system reaches a state of thermal equilibrium. Therefore, the populations in the Zeeman states are given by the Boltzmann distribution, at the temperature of the molecular environment.

RF pulses disturb the equilibrium of the spin system; thus, the spin populations after a pulse deviate from their thermal equilibrium values.

Relaxation is the process by which equilibrium is regained, through interaction of the spin system with the thermal molecular environment. The relaxation processes are divided in two types:

- spin-lattice relaxation or longitudinal relaxation time (T_1).
- spin-spin relaxation or transverse relaxation time (T_2).

1.2.5.1 Spin-lattice Relaxation Time T_1

For a spin $\frac{1}{2}$ system, the relaxation is caused by a fluctuating magnetic field at the site of the nuclear spins which is the direct consequence of the thermal motion of the molecules. The dominant relaxation mechanisms include the dipole-dipole interaction, the chemical shift anisotropy, and the spin rotation. However, in most experimental cases, one can be dominant over other mechanisms depending on the molecule or nucleus of interest. For spin

greater than $\frac{1}{2}$, the dominant relaxation mechanism is the interaction between the nuclear electric quadrupole and the electric field gradient (quadrupole $\gg$ dipole-dipole > chemical shift anisotropy > spin-rotation).

Now let us examine how the spin state population is affected by these relaxation mechanisms. For simplicity we still consider a system with two Zeeman states $|\alpha\rangle$ and $|\beta\rangle$ (see Figure 1.3).

We can write the differential equations for the change of the population in the two states as follows:

$$\begin{cases} \frac{dp_{|\alpha\rangle}}{dt} = p_{|\beta\rangle} W_{|\beta\rangle\rightarrow|\alpha\rangle} - p_{|\alpha\rangle} W_{|\alpha\rangle\rightarrow|\beta\rangle} & [1.40] \\ \frac{dp_{|\beta\rangle}}{dt} = p_{|\alpha\rangle} W_{|\alpha\rangle\rightarrow|\beta\rangle} - p_{|\beta\rangle} W_{|\beta\rangle\rightarrow|\alpha\rangle} & [1.41] \end{cases}$$

where $p_{|\alpha\rangle}$ and $p_{|\beta\rangle}$ represent the fractional occupation of states $|\alpha\rangle$ and $|\beta\rangle$, respectively. The normalization condition requires that: $\sum_n p_{|n\rangle} = 1$. $W_{|\alpha\rangle\rightarrow|\beta\rangle}$ denotes the transition probability per unit time from state $|\alpha\rangle$ to state $|\beta\rangle$. We will denote the reverse transition by $W_{|\beta\rangle\rightarrow|\alpha\rangle}$.

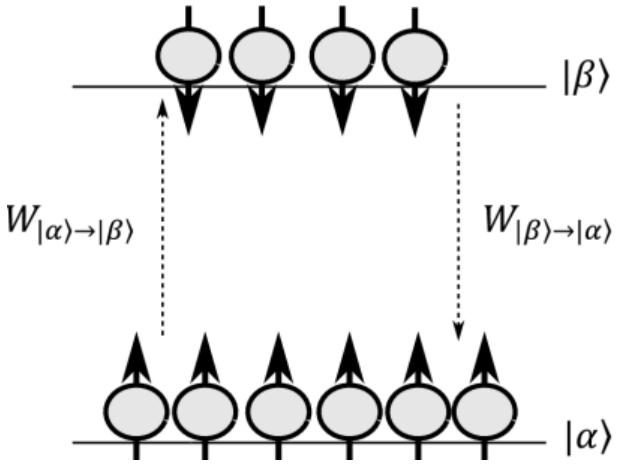

Figure 1.3: Populations distribution at thermal equilibrium.

From equation [1.26], one can deduce that the longitudinal magnetization vector is proportional to the difference in the spin state populations and is given as:

$$M_z = \xi\left(p_{|\alpha\rangle} - p_{|\beta\rangle}\right) \quad [1.42]$$

where $\xi = \frac{\gamma\hbar N_I}{2}$. As a result, the equation of motion is described as:

$$\frac{dM_z}{dt} = \xi\left(\frac{dp_{|\alpha\rangle}}{dt} - \frac{dp_{|\beta\rangle}}{dt}\right) \quad [1.43]$$

By substituting equations [1.40] and [1.41], one gets:

$$\frac{dM_z}{dt} = 2\xi\left(p_{|\beta\rangle}W_{|\beta\rangle\to|\alpha\rangle} - p_{|\alpha\rangle}W_{|\alpha\rangle\to|\beta\rangle}\right) \quad [1.44]$$

In practice, the probability of inducing a transition from the lower energy state to the higher energy state is different from the transition of the higher energy state to the lower energy state. This is also verified by the fact that the spin system obeys the Boltzmann distribution at the equilibrium state. Therefore, the Boltzmann distribution is only stable if the probability $W_{|\alpha\rangle\to|\beta\rangle} < W_{|\beta\rangle\to|\alpha\rangle}$. As a consequence, the flow of population at equilibrium state in the two directions must equal:

$$p^{eq}_{|\alpha\rangle}W_{|\alpha\rangle\to|\beta\rangle} = p^{eq}_{|\beta\rangle}W_{|\beta\rangle\to|\alpha\rangle} \quad [1.45]$$

where $p^{eq}_{|\alpha\rangle}$ and $p^{eq}_{|\beta\rangle}$ are the fractional occupation of state $|\alpha\rangle$ and state $|\beta\rangle$ at the thermal equilibrium state. Equation [1.45] is also called the principle of detailed balance. The fractional occupations of the states are given by the Boltzmann distribution:

$$\begin{cases} \mathrm{p}_{|\alpha\rangle}^{eq} = \dfrac{e^{-\frac{E_{|\alpha\rangle}}{KT}}}{Z} \\ \mathrm{p}_{|\beta\rangle}^{eq} = \dfrac{e^{-\frac{E_{|\beta\rangle}}{KT}}}{Z} \end{cases} \quad [1.46]$$

where $E_{|\alpha\rangle}$ and $E_{|\beta\rangle}$ are the energies of the states $|\alpha\rangle$ and $|\beta\rangle$.

$$Z = \sum_{n} e^{-\frac{E_n}{KT}} \quad [1.47]$$

is the partition function or sum of the states.

Using the high-temperature approximation, equations [1.46] can be reduced to:

$$\begin{cases} \mathrm{p}_{|\alpha\rangle}^{eq} \cong \dfrac{1}{2}\left(1 + \dfrac{1}{2}\mathbb{R}\right) \\ \mathrm{p}_{|\beta\rangle}^{eq} \cong \dfrac{1}{2}\left(1 - \dfrac{1}{2}\mathbb{R}\right) \end{cases} \quad [1.48]$$

where $\mathbb{R} \overset{\text{def}}{\cong} \frac{\hbar\gamma B_0}{k_B T}$.

Hence, by substituting equations [1.48] into equation [1.45] we can express the transition probability as function of a mean transition probability W per unit time between the states.

$$\begin{cases} W_{|\alpha\rangle\to|\beta\rangle} = W\left(1 - \dfrac{1}{2}\mathbb{R}\right) \\ W_{|\beta\rangle\to|\alpha\rangle} = W\left(1 + \dfrac{1}{2}\mathbb{R}\right) \end{cases} \quad [1.49]$$

Using the normalization condition, equations [1.49], and equation [1.42], we obtain:

$$\frac{dM_z}{dt} = -2W(M_z - 1) \quad [1.50]$$

The solution of the above equation is thus given by:

$$M_z(t) = (M_z^0 - 1)e^{-2Wt} + 1 \qquad [1.51]$$

From this equation, we can conclude that:

$$T_1 = \frac{1}{2W} \qquad [1.52]$$

Therefore, the spin-lattice relaxation time is equal to twice the mean transition probability per unit time between the states. This mean transition probability can be derived for the random field model from first principles (see Principles of Magnetic Resonance by Slichter) as:

$$W = \frac{1}{2}\gamma^2\langle B_1^2(t)\rangle \Im(\omega_0) \qquad [1.53]$$

where $B_1(t)$ is the radio frequency field applied along the x'-axis in the rotating frame and $\Im(\omega_0)$ is the spectral density function. The spectral density function is defined as twice the Fourier transform of the autocorrelation function $\mathbb{G}(\tau)$:

$$\Im(\omega) = 2\int_0^\infty \mathbb{G}(\tau)e^{-i\omega\tau}\,d\tau = 2\int_0^\infty \left(e^{-\frac{|\tau|}{\tau_c}}\,e^{-i\omega\tau}\right)d\tau \qquad [1.54]$$

where τ_c is the correlation time of the fluctuation of the local magnetic field in the x′-axis. Therefore, the rate of the spin-lattice relaxation time is given by:

$$\frac{1}{T_1} = \gamma^2\langle B_1^2(t)\rangle \frac{\tau_c}{1 + (\omega_0\tau_c)^2} \qquad [1.55]$$

The plot of the spin-lattice relaxation time verses the correlation time is shown in Figure 1.4.

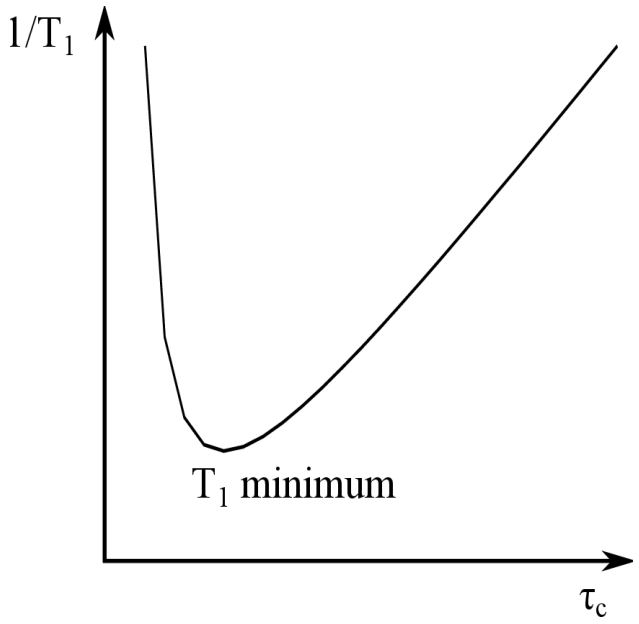

Figure 1.4: Spin-lattice relaxation time as function of the correlation time for random field fluctuation.

In most NMR experimental situations near room temperature, the T_1 is close to the T_1 minimum. As a result, the small value of T_1 permits increased number of signal averaging in a given duration and thus increased signal-to-noise ratio (SNR). Also, for systems with short correlation times, namely small molecules in nonviscous solutions, the spin-lattice relaxation time increases with temperature (36).

The liquid-like ^{1}H T_1 relaxation mechanism observed in biological tissue involves both intramolecular and intermolecular dipolar interactions of macromolecules and water molecules. The general form is given by:

$$\frac{1}{T_1} = \frac{3}{10}\left(\frac{\hbar\gamma^2}{r^3}\right)^2\left(\frac{\tau_c}{1+\omega_0^2\tau_c^2} + \frac{4\tau_c}{1+4\omega_0^2\tau_c^2}\right) \qquad [1.56]$$

where *r* is the distance between the dipoles.

Similarly, the spin-spin relaxation time (T_2) was found to be:

$$\frac{1}{T_2} = \frac{3}{20}\left(\frac{\hbar\gamma^2}{r^3}\right)^2\left(3\tau_c + \frac{5\tau_c}{1+\omega_0^2\tau_c^2} + \frac{2\tau_c}{1+4\omega_0^2\tau_c^2}\right) \quad [1.57]$$

The detailed derivation of equations [1.56] and [1.57] can be found in the following references (6,37). Moreover, equations [1.56] and [1.57] show that the spin-lattice relaxation value is close to the value of the spin-spin relaxation time when the correlation time is short. These two relaxation times have larger difference when the correlation time becomes longer and T_1 is always greater than T_2.

In practice, the relaxation times are temperature-dependent. This is because the random field fluctuations originate from the molecular environment, and also the correlation time τ_c is a function of temperature. The correlation time is inversely proportional to temperature T according to Debye theory (38): $\tau_c \propto \frac{1}{T}$.

Furthermore, at the Larmor frequency the term $\omega_0\tau_c \ll 1$, which implies that:

$$\frac{1}{T_1} \propto \tau_c \propto \frac{1}{T} \quad [1.58]$$

Hence, T_1 is linearly proportional to the temperature when $\omega_0\tau_c \ll 1$. The effect of temperature on T_1 depends on the location of the correlation with respect to the minimum of T_1 (see Figure 1.4). For a system with long correlation times, such as large molecules which tumble slowly, increasing the temperature of the sample generally reduces the spin-lattice relaxation time constant T_1. Inversely, for small molecules which tumble very rapidly (short correlation times), such as free water (the correlation time is about 10^{-12}), T_1 values increase with temperature.

1.3 MR Signal Detection Concepts

A spin system in a static magnetic field B_0 at which we apply a perturbing, transient RF field perpendicular to the static field direction is described by equation [1.39]. In scalar form, we have:

$$\begin{cases} \dfrac{dM_{x'}}{dt} = 0 \\ \dfrac{dM_{y'}}{dt} = \gamma B_1(t) M_{z'} \\ \dfrac{dM_{z'}}{dt} = -\gamma B_1(t) M_{y'} \end{cases} \quad [1.59]$$

A closed-form solution to the above equations set and under the initial conditions: $M_{x'}(0) = M_{y'}(0) = 0$ and $M_{z'}(0) = M_z^0$ are given by:

$$\begin{cases} M_{x'}(t) = 0 \\ M_{y'}(t) = M_z^0 \sin\left(\int_0^t \gamma B_1(t')dt'\right) \\ M_{z'}(t) = M_z^0 \cos\left(\int_0^t \gamma B_1(t')dt'\right) \end{cases} \quad [1.60]$$

These solutions indicate that the effect of the applied RF field at the resonance frequency is a precession of the bulk magnetization about the axis of the applied magnetic field in the rotating frame. The next question is how to convert this rotating magnetization to electric signal.

The fundamental signal in an MR experiment comes from the detection of the electromotive force (*emf*) induced in any coil by the precessing spin's magnetic flux of the transverse bulk magnetization. The *emf* induced in a coil by a changing magnetic flux can be calculated by Faraday's law of induction:

$$emf = -\frac{d\phi}{dt} = -\frac{d}{dt}\left(\int \vec{B}_{receive} \cdot d\vec{S}\right) \quad [1.61]$$

where ϕ is the flux through the coil. $\vec{B}_{receive}$ is the magnetic field created by the current density induced in the conducting loop by a changing flux. $\vec{B}_{receive}$ opposes the changes induced by the external field and this is referred to as Lenz's law. $d\vec{S}$ is a unit vector perpendicular to the loop surface element dS.

The above equation can be furthermore transformed using the principle of reciprocity to obtain:

$$V(t) = emf = -\frac{d}{dt}\left(\int d^3r\, \vec{M}(\vec{r},t) \cdot \vec{B}_{receive}(\vec{r})\right) \quad [1.62]$$

The *emf* or voltage *V(t)* induced in the receiver coil is often regarded as the raw NMR signal. Since the transverse magnetization vector precesses at the Larmor frequency, thus the detected signal *V(t)* is a high-frequency signal which can be problematic for electronic circuitries. Therefore, *V(t)* is moved to a low-frequency band using the so-called phase-sensitive detection (PSD) or signal demodulation method. The signal demodulation consists of multiplying the received voltage *V(t)* by a reference sinusoidal signal $(2\cos(\omega_0 t))$ and then low-pass filtering it to remove the high-frequency component. Hence, the output of the PSD is a low-frequency signal. A major drawback with this detection scheme is the difficulty to determine from the received signal whether the transverse bulk magnetization vector is rotating clockwise or counterclockwise. To overcome this problem, a second PSD system is used which has a $\frac{\pi}{2}$ phase shift relative to the first, namely $2\sin(\omega_0 t)$. This detection scheme is known as quadrature detection and it is commonly used in modern MRI system. The schematic of the signal demodulation steps are described in Figure 1.5.

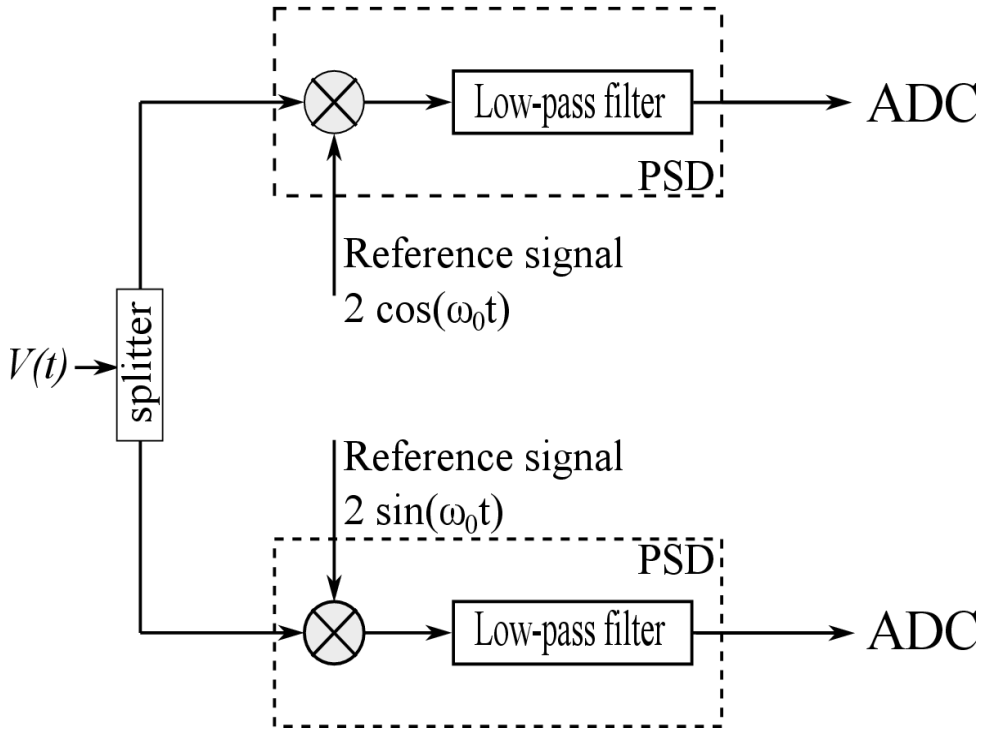

Figure 1.5: Diagram of the phase-sensitive detection scheme

Furthermore, it can be shown (39) that the final output of the quadrature detector obeys the following signal expression:

$$S(t) = \int B_{r,xy}(r) M_{xy}(r,0) e^{-i\Delta\omega(r)t} d^3r \qquad [1.63]$$

where $B_{r,xy}$, M_{xy} are the transverse components of the receiver magnetic field and the bulk magnetization at a location *r*, respectively. Δω is the spatially dependent resonance frequency in the rotating frame.

Moreover, if the receiver coil has a homogeneous reception field over a region of interest (ROI), as it is often the case, equation [1.63] can be reduced to:

$$S(t) = \int M_{xy}(r,0) e^{-i\Delta\omega(r)t} d^3r \qquad [1.64]$$

1.4 Basic Pulse Sequences

We begin with some general assumptions underlying the discussion throughout this section:

- First, we assume that the RF pulse is applied instantaneously so that the pulse interval is treated as zero, during which either of T1 and T_2 relaxation does not occur.
- Second, we ignore any imperfections in excitation and reception so that the signal equation is described by equation [1.64].

Under these assumptions, we start the study of the signal by considering a simple, though important, RF field application scheme during MRI experiments. The first is a single RF excitation pulse applied uniformly to the sample. The second is a pair of RF pulses, i.e, the excitation pulse followed by another pulse whose purpose is to help recover via an echo, some of the signal lost due to T_2 relaxation mechanism. The third is another form of echo signal frequently used in MRI and generated using time-varying gradient magnetic fields.

1.4.1 Free Induction Decay (FID)

The simplest MRI experiment is the detection of a global signal from a sample in a static magnetic field after the application of a single RF pulse. The total time-varying coherent magnetic field derived from the transverse bulk magnetization would induce a small *emf* in any RF coil properly oriented to detect the corresponding flux change. This experiment is called the free induction decay or FID. The sequence diagram is given in Figure 1.6.

FID signal is the most basic form of transient signal from a spin system after the application of an excitation pulse. The signal equation of a FID resulting from an α pulse is:

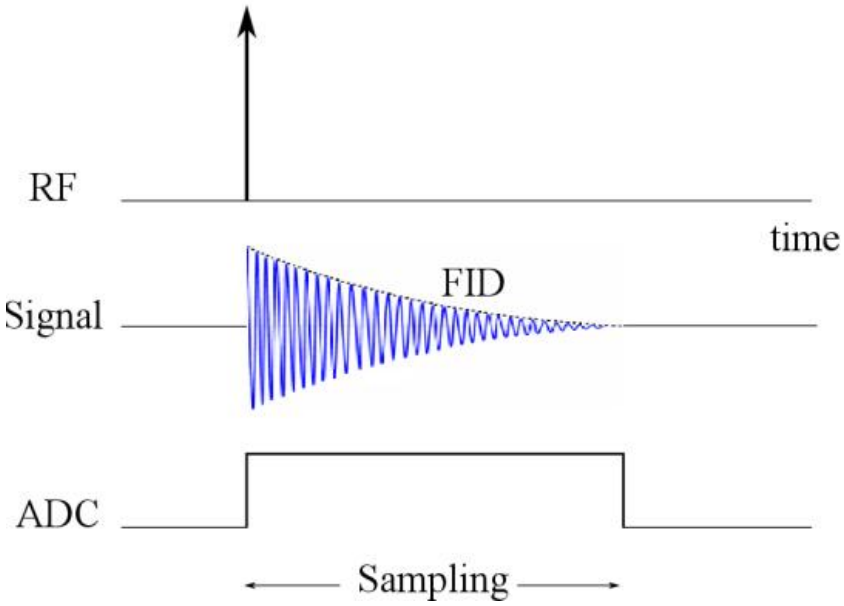

Figure 1.6: FID sequence diagram. ADC (Analog-to-Digital Converter) is the device used to sample the signal over time.

$$S(t) = sin\alpha \int_{-\infty}^{+\infty} \rho(\omega) e^{-\frac{t}{T_2(\omega)}} e^{-i\omega t} d\omega \qquad t \geq 0 \qquad [1.65]$$

where $\rho(\omega)$ is the spectral density function which determines the characteristics of the FID signal. For a spin system with a single spectral component resonating at frequency ω_0, equation [1.65] can be reduced to:

$$S(t) = M_z^0 \sin\alpha \; e^{-i\omega_0 t} \, e^{-\frac{t}{T_2}} \qquad [1.66]$$

The T_2 decay occurs when both the sample and the magnetic field to which the sample is exposed are perfectly homogeneous. When the field is inhomogeneous with the local field distribution ΔB_0, a new time constant T_2^* is used, such as:

$$\frac{1}{T_2^*} = \frac{1}{T_2} + \gamma \Delta B_0 \qquad [1.67]$$

1.4.2 Spin Echo (RF Echo)

One of the major distinctions between an FID signal and an echo signal is the signal shape. The echo signal shape consists of two sides: the FID signal mirror image shape and the FID signal shape. One side is from the refocusing phase of the transverse magnetization and the other side is from the dephasing period. The echo signal can be generated either by multiple RF pulses (RF echoes) or by the field gradient reversal (gradient echo). For simplicity, we will describe the RF echo derived from just two RF pulses. The latter is known as a spin echo and was first observed by Erwin Hahn in 1950. Figure 1.7 gives a schematic description of the spin echo formation from a pair of RF pulses 90°-180°.

The FID produced by the 90^o RF pulse is quickly dephased because of the field inhomogeneities (ignoring the gradient fields) and completely vanishes at $t = \tau$, as shown by Figure 1.7. Note that the initial FID signal does not have to totally vanish before the 180^o refocusing pulse. After the 180^o pulse, the transverse magnetization starts to grow gradually and reaches the maximum amplitude at $t = 2\tau$. The mechanism responsible of the FID decay after the 90^o excitation pulse is the same which is responsible for the formation of the echo at $t = 2\tau$. Furthermore, one can describe intuitively the action of the RF pulses on the spin system that will result in the formation of the spin echo in the rotating reference frame. For simplicity, we assume that the excitation pulse (90^o) is applied along the x'-axis, the refocusing pulse (180^o) is applied along the y'-axis, and the spin system is composed of multiple isochromats, which precess at different frequencies. The pictorial description of the spin evolution during the spin echo formation is described in Figure 1.8.

The signal equation of the spin echo created by an arbitrary two RF pulses (α_1 and α_2) can be derived in the straightforward manner and is expressed as:

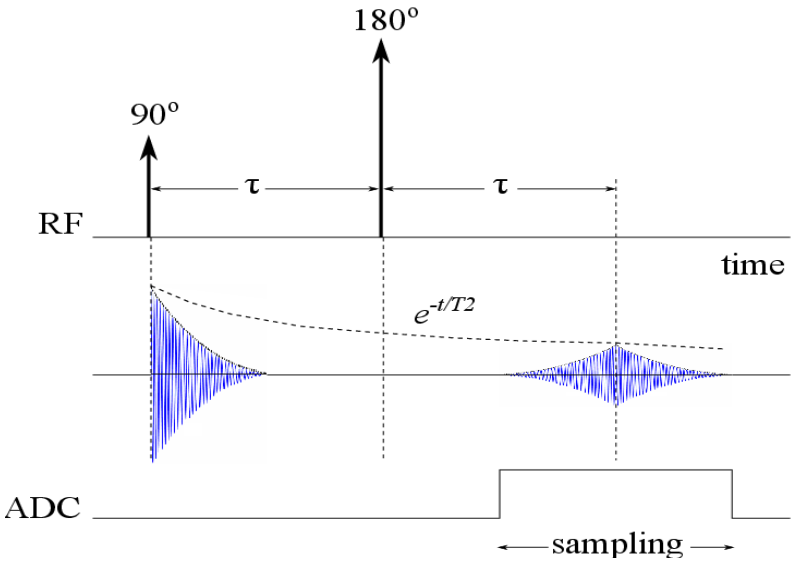

Figure 1.7: Diagram of the spin echo produced by a pair 90° - 180° RF pulses.

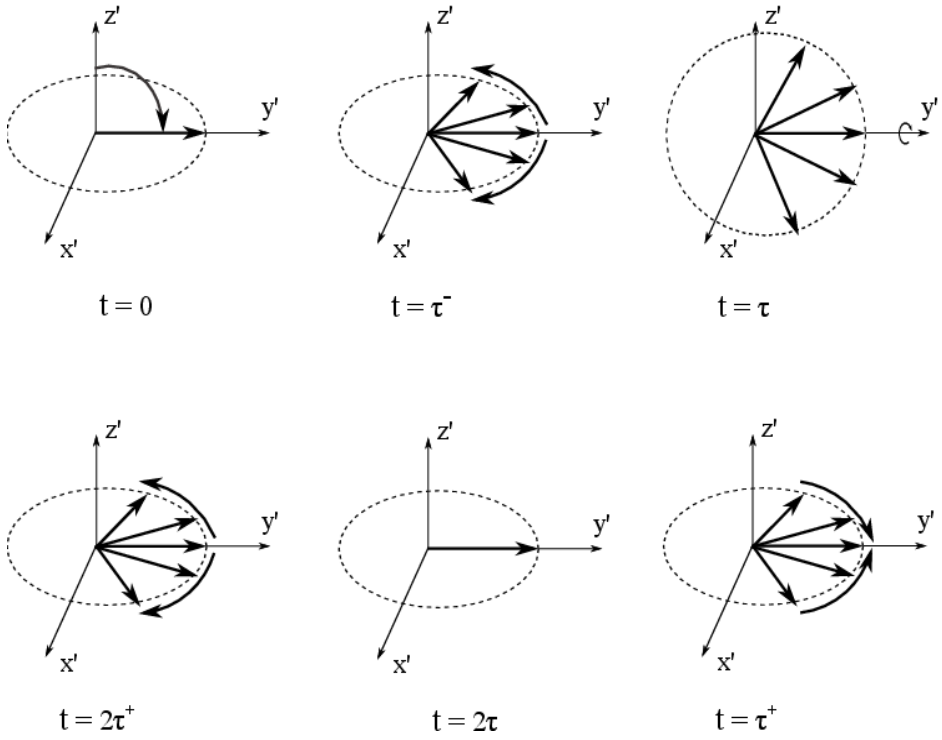

Figure 1.8: Schematic of the spin echo formation. At $\boldsymbol{t = 0}$, the longitudinal bulk magnetization rotates in the transverse plane. At $\boldsymbol{t = \tau^-}$, the spin system begins to fan out because of precessional frequency differences between the isochromats. At $\boldsymbol{t = \tau}$, all the spins are rotated by 180° around the y'-axis. At $\boldsymbol{t = \tau^+}$, the spins continue to rephase gradually and eventually rephase at $\boldsymbol{t = 2\tau}$. The phase coherence of the spins is altered at time $\boldsymbol{t > 2\tau}$.

$$S(t) = sin\alpha_1 sin^2\left(\frac{\alpha_2}{2}\right)\int_{-\infty}^{+\infty}\rho(\omega)e^{-\frac{t}{T_2(\omega)}}e^{-i\omega(t-TE)}d\omega \quad [1.68]$$

where TE is the echo time. For the above example (90^o – 180^o pulse train), equation [1.68] reduces to:

$$S(t) = \int_{-\infty}^{+\infty}\rho(\omega)e^{-\frac{t}{T_2(\omega)}}e^{-i\omega(t-TE-\frac{\pi}{2})}d\omega \quad [1.69]$$

It is also possible to analyze the echoes produced by multiple RF pulses using the extended phase graphs. The extended phase graph is a graphical representation of the phase evolution of the magnetization components, so that each echo can be revealed pictorially before even deriving their respective signal equations. For more information about the extended phase graphs, the reader is referred to Woessner's paper (40).

1.4.3 Gradient Echoes

The mechanism of the gradient echo formation is that a gradient field can dephase and rephase the signal in controlled fashion. A gradient echo occurs when the net phase $\phi(x,y,z,t) = 0$. After applying an RF pulse, the spins in different locations (x,y,z) will acquire different phases given by:

$$\phi(x,y,z,t) = \gamma\int_0^t \vec{G}(\tau)\cdot\vec{r}\,d\tau \quad [1.70]$$

where $\vec{\mathrm{G}}(\tau) = \mathrm{G_x}\vec{\imath} + \mathrm{G_y}\vec{\jmath} + \mathrm{G_z}\vec{k}$ and $\mathrm{G_x} = \frac{\partial \mathrm{B_{G,z}}}{\partial \mathrm{x}}, \mathrm{G_y} = \frac{\partial \mathrm{B_{G,z}}}{\partial \mathrm{y}}, \mathrm{G_x} = \frac{\partial \mathrm{B_{G,z}}}{\partial \mathrm{z}}$

$\mathrm{B_{G,z}}$ is the z-component of a gradient field $\vec{\mathrm{B}}_\mathrm{G}$ which is, in MRI context, a special kind of inhomogeneous field that varies linearly along the three directions ($\vec{\imath}, \vec{\jmath}, \vec{k}$).

Figure 1.9 depicts the gradient-echo pulse sequence.

In the presence of B_0 field inhomogeneities, the signal loss increases much faster over T_2 time and the spins will partially rephased at the echo time. As a result, the amplitude of the gradient echo signal carries a T_2^*-weighting, which is one of the main difference between the gradient echo and the RF echo (T_2-weighting).

1.5 Selective Excitation

There are two types of spatial localization methods: selective excitation and spatial encoding. These two localization methods use the gradient fields provided in modern MRI systems where the shapes and forms can be adjusted independently. If $B_1$is applied to a sample in the presence of the static magnetic field B_0, then all spins are at the same resonance frequency;

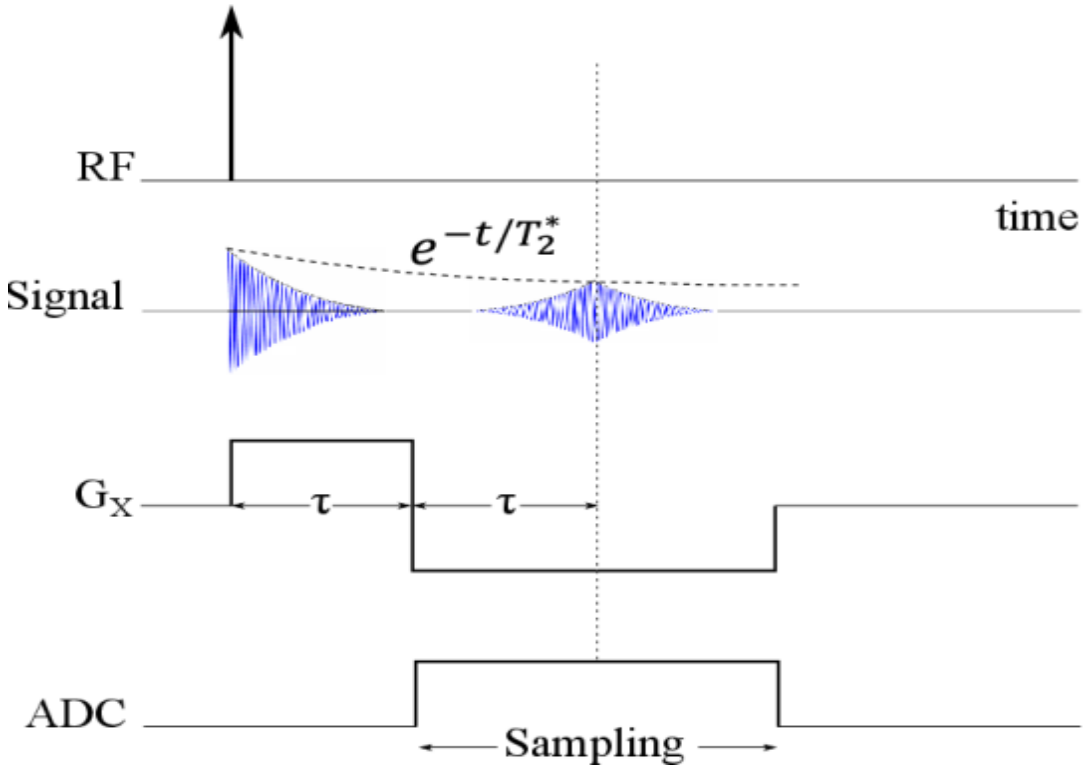

Figure 1.9: Timing diagram of the formation of the gradient echo.

thus, the excitation is nonselective since all spins are tipped. Therefore, some form of 3D imaging must be performed, which is usually time consuming unless image contrast or spatial resolution is compromised. Consequently, it is desirable to reduce the 3D imaging to 2D imaging by exciting a plane instead of the entire volume of the sample. Such a selective excitation is performed by applying an additional linear gradient field along the slice selection direction in addition to B_1 and B_0. In practice, the gradient field has to be sufficiently large to be able to excite a thin slice.

An amplitude-modulated RF pulse is characterized by an excitation frequency ω_{rf} and an envelope $B_1^e(t)$ as follows:

$$B_1(t) = B_1^e(t)e^{-i\omega_{rf}t} \qquad [1.71]$$

where $B_1^e(t) = Asinc(\pi\Delta f t)$ and $\Delta f = \frac{\gamma}{2\pi} G_z \Delta z$.

To excite a plane, say, perpendicular to the z-axis of thickness Δz, the gradient G_z must be turned on during the RF excitation. Since B_1 is applied at the Larmor frequency ω_0 for excitation to occur, therefore, B_1 must now possess a temporal frequency bandwidth that matches the bandwidth of resonance frequencies of spins in the slice of interest. Figure 1.10 gives an illustration of different gradient strengths G_z mapping a sinc-pulse to the corresponding slices thickness Δz.

Note that to have a perfect rectangular excitation profile, the sinc-pulse has to have infinite duration. In practice, the pulse has to be truncated to a finite duration resulting in a nonuniform excitation profile across the slice and also in excitation of spins in the adjacent slices. The latter phenomenon results in an artifact in the image and is known as the cross-talk artifact. In practice, many other slice-selective pulses are used to minimize the cross-talk

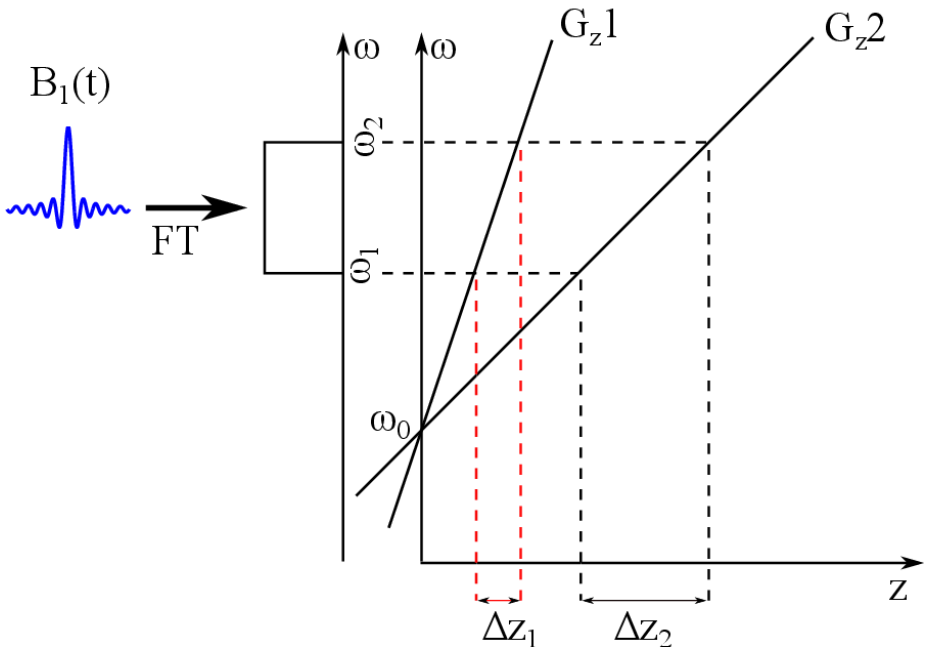

Figure 1.10: Selective excitation. Mapping using different gradient strengths to the corresponding slices thickness for a rectangular slice profile.

artifact in the images such as the hyperbolic secant pulse, a custom designed Shinnar-Le Roux selective excitation pulse (SLR) among others.

1.6 Spatial Encoding (K-Space)

Equation [1.64] can be written in one dimension as a function of the spectral density as:

$$S(t) = \int \rho(x) e^{-i\Delta\omega(x)t} dx \qquad [1.72]$$

If the magnetic field that a sample experiences after an excitation is B_0 plus the linear gradient field ($G_x x$), the above signal equation becomes:

$$S(t) = \int \rho(x) e^{-i\gamma(B_0 + G_x x)t} dx \qquad [1.73]$$

Hence, the signal is said to be frequency-encoded because it oscillates with frequency: $\omega(x) = \gamma(B_0 + G_x x)$ which is linearly related to the spatial position *x* and G_x is called the frequency encoding gradient. Similarly, in 2D, the oscillation frequency of the signal is given by: $\omega(x,y) = \gamma\big(B_0 + G_x x + G_y y\big)$ where G_y is the phase encoding gradient.

By making some simple change of variables in equation [1.73] in 2D, one can deduce that:

$$S\big(k_x, k_y\big) = \iint m(x,y) e^{-i2\pi\left(k_x(t)x + k_y(t)y\right)} dx\, dy \qquad [1.74]$$

where: $m(x,y) = \rho(x,y)e^{-i\gamma B_0}$ and

$$k_x(t) = \frac{\gamma}{2\pi}\int_0^t G_x(t')dt' \qquad [1.75]$$

$$k_y(t) = \frac{\gamma}{2\pi}\int_0^t G_y(t')dt' \qquad [1.76]$$

Hence, $S(k_x, k_y)$ is the Fourier Transform (FT) of the image $m(x,y)$. In other words, $S(k_x, k_y)$ is the frequency spectrum of the MR image. This frequency space is known as k-space. The name k-space was introduced in MRI in 1979 by Likes (41). The k-space coordinates (k_x, k_y) define the so-called sampling trajectory of k-space. Furthermore, it can be seen from equations [1.75] and [1.76] that the form and shape of the gradient do not affect the k-space trajectories, as long as the areas under the curves remain the same. Figure 1.11 shows the timing diagrams and the corresponding k-space trajectories of two commonly used pulse sequences: the gradient echo and the spin echo sequences. These k-space trajectories are referred to as Cartesian k-space filling.

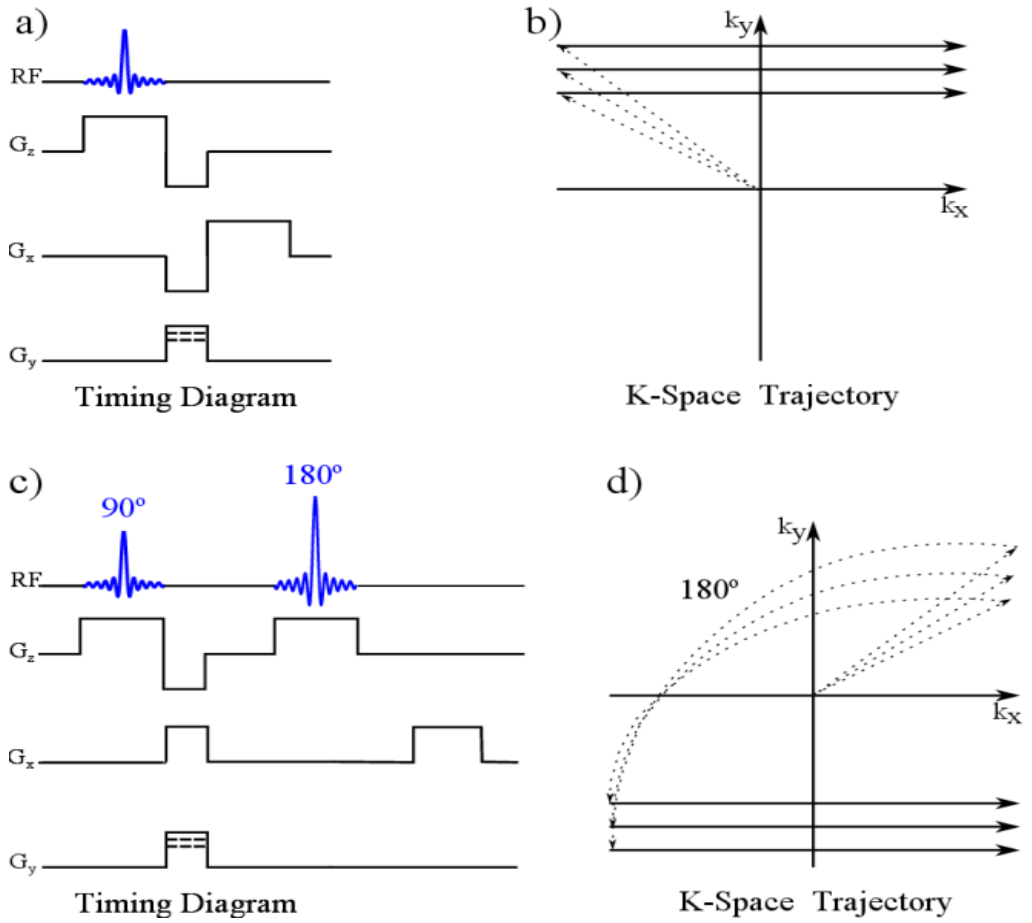

Figure 1.11: Examples of timing diagram and k-space trajectory. a-b) Timing diagram and the corresponding k-space trajectory of the gradient recall echo (GRE) sequence. c-d) Timing diagram and k-space trajectory of the spin echo (SE) sequence.

1.7 Sampling Requirements of K-Space Signal in 2D Fourier Transform Imaging

According to equation [1.74], a faithful k-space signal would be derived if an accurate integration can be carried out and if the signal could be measured continuously for a very long time. In practice, several factors prevent the continuous data collection over all k-space, such as the signal sampling which must be carried out within a finite time length and also the spin relaxation phenomena which will wipe out the signal after a certain time period. In actuality, the data collected will be a truncated and discretized version of $S(k_x, k_y)$. Hence,

it becomes essential to understand the impact of the use of the Discrete Fourier Transform (DFT) upon the resulting images. In fact, sampling of k-space is a multidimensional problem, but one can treat sampling along each dimension separately, thus reducing it to one–dimensional sampling problem.

One-dimensional sampling of the function $m(x)$ can be modeled by multiplying the function by a comb function $\frac{1}{\Delta}\text{Ш}\left(\frac{1}{\Delta}\right)$ where $\text{Ш}\left(\frac{1}{\Delta}\right)$ is an infinite string of equally spaced delta functions separated by Δ, the sampling period. Hence, the sampling version of $m(x)$ is given by:

$$\widehat{m}(k_x) = m(k_x) \cdot \frac{1}{\Delta k_x}\text{Ш}\left(\frac{k_x}{\Delta k_x}\right) = \sum_{n=-\infty}^{n=+\infty} m(n\Delta k_x)\delta(k_x - n\Delta k_x) \qquad [1.77]$$

Therefore, the MR image is extracted by taking the Inverse Fourier transform (FT^{-1}) of equation [1.77] as follows:

$$\widehat{M}(x) = FT^{-1}\{\widehat{m}(k_x)\} = \frac{1}{\Delta k_x}\sum_{n=-\infty}^{n=+\infty} M\left(x - \frac{n}{\Delta k_x}\right) \qquad [1.78]$$

From the above equation, one can deduce that the final image is formed by the replicated versions of the image itself, and the replications are separated by the sampling rate: $\frac{1}{\Delta k_x}$. If the sampling rate is too low, then the replications will overlap, resulting in a condition known as aliasing. The minimum sampling rate that avoids aliasing is called the Nyquist rate. If we assume that an object being imaged is bounded by a rectangular field of view of widths FOV_x and FOV_y, as shown in Figure 1.12, thus, to avoid aliasing, the following conditions must be satisfied:

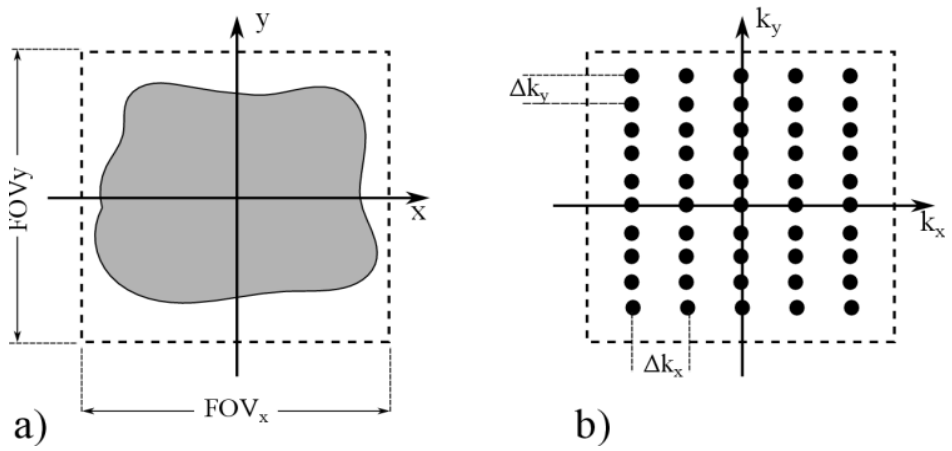

Figure 1.12: Field of view and k-space mapping. a) Illustration of an object within the field of view (FOV_x, FOV_y). b) Corresponding k-space map.

$$\Delta k_x \leq \frac{1}{FOV_x} \text{ and } \Delta k_y \leq \frac{1}{FOV_y} \quad [1.79]$$

In practice, the aliasing artifact can be avoided by oversampling the signal along a given direction. This technique is applied automatically in the readout direction. However, oversampling in the phase encoding direction will increase the scan time. Hence, the remaining alternative will be to eventually increase FOV_y or to decrease the residual signal outside the FOV by using surface coils or saturation bands.

CHAPTER II

MAGNETIC RESONANCE THERMOMETRY

2.1 Introduction

The temperature dependency of MRI parameters and the attractive properties of MRI, such as its noninvasiveness, lack of ionizing radiation, and the ability to image in any scan orientation with good spatial and temporal resolution, make it an ideal tool for temperature mapping during a thermal therapy. The temperature-dependent MR-measured parameters are:

- spin-lattice relaxation time T_1,
- proton resonance frequency shift,
- proton density,
- diffusion coefficient,
- magnetization transfer effect.

Whereas temperature effects on these parameters have been well described previously, the first report of temperature mapping by MRI appeared in 1983 (2) and was based on the longitudinal relaxation time T_1. Since then, many other MR temperature imaging methods have been proposed with different levels of temperature sensitivity, spatial and temporal resolutions.

In this chapter, the MR thermometry methods are reviewed and compared in terms

of their temperature sensitivity, linearity with temperature, acquisition, speed, and accuracy. The most common methods (PRF and T_1) are covered in detail whereas the less common methods are treated briefly for completeness.

2.2 T_1 Relaxation Time of Water Protons

We have shown in Chapter I section 1.2.2.1 that the spin-lattice relaxation time is proportional to temperature via the rotational and translational correlation times. These correlation times for the bound water hydrogen can be defined as:

$$\tau = A \cdot exp\left(\frac{E_\alpha}{k_B T}\right) \quad [2.1]$$

where A is a constant, E_α is the activation energy of the relaxation process, k_B is the Boltzmann constant and T is the absolute temperature. As a consequence, T_1 is a function of the temperature:

$$T_1 \propto \exp\left(-\frac{E_\alpha}{k_B T}\right) \quad [2.2]$$

More detail about the derivation of the above equation is found in Bottomley et al. (8). For small temperature variations, T_1 is linearly dependent on temperature and both T_1 and its temperature dependency vary from tissue to tissue. This can be easily explained by the fact that T_1 is sensitive to the dynamic structure and amount of water in biological system. The linear temperature dependency of T_1 can be expressed as:

$$T_1 = T_1(T_{ref}) + \lambda(T - T_{ref}) \quad [2.3]$$

where $\lambda = \frac{dT_1}{dT}$ is the thermal coefficient which is determined empirically for each tissue, and T_{ref} is the reference temperature. The temperature dependency of T_1 was found to be in the order of 1%/^{o}C (10), with 1.4%/^{o}C in bovine muscle (11), 1-2%/^{o}C in liver (12), and 1.79-3%/^{o}C in fat (-CH_2-, CH_3-) (42).

2.2.1 T_1 Measuring Methods in MRI

The methods enumerated below are not necessary an exhaustive list of the T_1 mapping methods; rather, they show some of the most common methods used to measure T_1 in MRI.

2.2.1.1 Inversion Recovery Method

The gold standard method for T_1 quantification in MRI is the inversion recovery (IR) method. The IR pulse sequence comprises a 180^o RF pulse followed by a readout module, e.g., a GRE or Spin echo readout, which is delayed by a time TI, called inversion time. In its application, a series of IR images are acquired from the same location, each with a different inversion time (TI) while keeping all others parameters identical. To avoid signal saturation, the repetition time TR must exceed four times the maximum T_1 of the sample of interest. Under this condition, T_1 can be extracted from the plot of the pixel intensity of a series of images versus TI using a Levenberg-Marquardt (43) nonlinear fitting to the signal equation given by:

$$M_z(TI) = M_0\left(1 - 2e^{-\frac{TI}{T_1}}\right) \qquad [2.4]$$

Furthermore, the saturation recovery (SR) pulse sequence is often used to avoid the step of negating the signals prior to the zero-crossing point. A typical saturation pulse sequence

consists of multiple 90^o pulses separated by short repetition times (TR). The residual longitudinal magnetization that develops during each TR period is dephased by a spoiler applied along the slice selection direction. In that case, the equation to fit is:

$$M_z(TR) = M_0\left(1 - e^{-\frac{TR}{T_1}}\right) \quad [2.5]$$

T_1 quantification using SR or IR with conventional spin echo pulse sequence requires long acquisition time as full relaxation is a prerequisite for each TI measurement. Therefore, alternative methods have been developed to shorten the acquisition time. One method to overcome the lengthy acquisition time is to sample the longitudinal magnetization after the 180^o inversion pulse by applying a set of small flip angle RF pulses α_n (n $= 0, 1, 2 \ldots .$ N) separated in time by a period τ during each repetition time. The timing diagram of the Look and Locker pulse sequence is depicted in Figure 2.1.

This technique was first described by Look and Locker (44) in 1970. In this approach, a separate phase encoding gradient of the same value is used for each α_n RF pulse and the transverse magnetization is completely spoiled before each α_n RF pulse. Consequently, T_1 can be obtained from the longitudinal recovery curve of N different pixel intensities at the inversion times TI of (0, τ, 2τ, 3τ, …., $N\tau$). The fast sampling capability of a large set of points on the recovery curve has made this method very popular for in vivo T_1 measurements.

2.2.1.2 Double Flip Angles Method

The measurement of T_1 using the variable flip angles method has been around since 1974 (45) and has shown the capability to quantify T_1 in very short time with approximately the

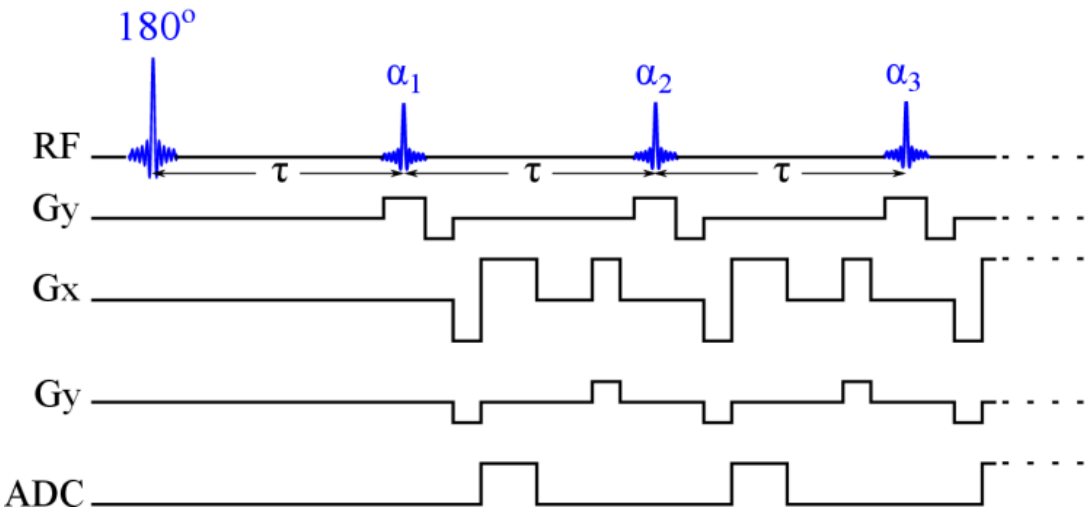

Figure 2.1: Pulse sequence diagram of the fast IR acquisition of multiple images after single 180° inversion pulse. The repetition time TR = N$\boldsymbol{\tau}$.

same accuracy as the IR and SR methods. The method exploits the T_1 dependency of the signal equation of a steady state spoiled gradient echo (SPGR) sequence:

$$SI_\alpha = M_0 \frac{1 - E_1}{1 - E_1 \cos(\alpha)} \sin(\alpha) E_2 \qquad [2.6]$$

where $E_1 = exp\left(-\frac{TR}{T_1}\right)$ and $E_2 = exp\left(-\frac{TE}{T_2^*}\right)$

With TR kept constant, one can linearize the above equation as follows:

$$\frac{SI_\alpha}{sin(\alpha)} = E_1 \frac{SI_\alpha}{tan(\alpha)} + M_0(1 - E_1)E_2 \qquad [2.7]$$

The plot of $\frac{SI_{\alpha_n}}{sin(\alpha_n)}$ verses $\frac{SI_{\alpha_n}}{tan(\alpha_n)}$ $(n = 1, 2, \ldots.)$ yields a linear curve of the form:

$$\frac{SI_{\alpha_n}}{sin(\alpha_n)} = slope \frac{SI_{\alpha_n}}{tan(\alpha_n)} + y\_intercep \qquad [2.8]$$

From the slope of the above equation, T_1 can be estimated by linear regression as:

$$T_1 = -\frac{TR}{\ln(slope)} \quad [2.9]$$

In the early days of the development of this method, without relying on any specific constraint on the different parameters, one might elect to simply acquire data for a uniform range of flip angles (46-48). Later, it was realized that the same T_1 precision could be achieved by just choosing two optimum flip angles (49,50). In fact, Deoni et al. (49) have demonstrated for a particular (TR/T_1) combination that T_1 variance can be minimized for a set of two flip angles (α_1, α_2) such as:

$$SI_{\alpha_1} = SI_{\alpha_2} = 0.71 * SI_{\alpha_E} \quad [2.10]$$

SI_{α_E} is the signal intensity at Ernst angle. Furthermore, they derived an analytical solution for the two ideal flip angles to be:

$$\alpha_{1,2} = \cos^{-1}\left(\frac{f^2 E_1 \pm (1 - E_1)\sqrt{1 - f^2}}{1 - E_1^2(1 - f^2)}\right) \quad [2.11]$$

with $f = \frac{SI_{\alpha_1}}{SI_{\alpha_E}} = \frac{SI_{\alpha_2}}{SI_{\alpha_E}}$.

The same results were later achieved by Schabel et al. (51) with $f = \sqrt{2}/2$ using the propagation of error method in conjunction with the theoretical signal equation for the spoiled gradient echo pulse sequence. Although in theory, the optimal flip angles for computing T_1 with high precision can be calculated for any (TR/T_1) combination, the spatial variation in flip angle due to the RF field inhomogeneity is unfortunately one of the main sources of error.

Inhomogeneity in the RF field can be caused by many factors. High B_0 field strengths make the RF wavelength shorter. For example, at 3T, inhomogeneity ranging from 30 to 50% has been observed (52). Also, a shorter wavelength causes the RF field to interact with the subject (tissue dielectric effect), causing even more inhomogeneity. The distance from the transmit coil can also affect the RF field inhomogeneity.

There are a few strategies commonly used to minimize RF pulse profile errors such as:

- ✓ 3D acquisition scheme: In 3D, RF inhomogeneity errors can be tolerated if the region of interest is centered in the excited 3D slab where the slice profiles are almost ideal or if the slab-select gradient is turned off.
- ✓ Custom-designed SLR or fast passage adiabatic pulses can be used.
- ✓ B_1 field mapping is the most common method used for reducing the errors induced by RF field inhomogeneity and has been investigated by many authors (52-59) under a variety of acronyms.

2.3 Proton Resonance Frequency Shift

The proton resonance frequency shift is the most common and attractive MR thermometry method. The excellent linearity and near nonindependence of tissue type (except for fat), as well as good temperature sensitivity, make it the preferred MR thermometry method for a wide variety of thermal applications at mid- and high field strength. First observed by Hindman in 1966 (22) while studying the intermolecular forces and hydrogen bond formation between water molecules, PRF was later implemented and applied in MRI by Ishihara et al. (60) and De Porter et al. (24,25).

The chemical shift in water-based tissue exposed to a uniform magnetic field B_0 arises

because of the electrons in the outer atomic shells, and in the chemical bonds holding the water molecule together. In fact, the external magnetic field causes the electrons to circulate within their atomic orbital, thus creating a current density. This induced current density according to Faraday's law of magnetic induction will create its own magnetic field at the location of the nucleus that opposes the applied external field B_0. Therefore, the nucleus is partially shielded from the external field by its surrounding electrons.

The precession frequency of a given atomic nucleus is proportional to the local field that it experiences; therefore, the Larmor frequency is dependent on the location of the nucleus in the molecule and its electronic structure. As a result of the nuclear shielding, the resonance frequency becomes:

$$\omega = \gamma B_{loc} = \gamma B_0(1 - \sigma) \qquad [2.12]$$

where σ represents the shielding constant.

The effect of the dependence of the Larmor frequency on the local electronic environment is called the chemical shift in diamagnetic materials such as water, the Knight shift in metal and semiconductors, and the paramagnetic shift in paramagnetic substance.

In practical applications, it is convenient to express the chemical shift in terms of the ratio of the Larmor frequency and a reference frequency of the spectrometer as follows:

$$\delta = \frac{\omega - \omega_{ref}}{\omega_{ref}} \cdot 10^6 \qquad [2.13]$$

where δ is a dimensionless parameter in parts per million (ppm) and w_{ref} is the frequency of the reference nucleus corresponding to the exact center of the NMR spectrum.

Furthermore, one can express δ as function of the shielding constant by substituting the

frequencies by their expressions in equation [2.13]:

$$\delta = \frac{\sigma_{ref} - \sigma}{1 - \sigma_{ref}} \cdot 10^6 \approx \left(\sigma_{ref} - \sigma\right) \cdot 10^6 \qquad [2.14]$$

The above equation is derived under the assumption that $\sigma_{ref} \ll 1$. Note, one can deduce from equation [2.14] that an increase of the value the chemical shielding constant will reduce δ.

2.3.1 Temperature Dependence of PRF

In a water molecule, as the temperature increases, the hydrogen bonds stretch, bend, and break (22,27,61), leading to a stronger electron screening of the hydrogen nucleus. In practice, the shielding constant σ is caused by the chemical shift as well as the susceptibility effect. For now, we will only consider the dominant effect which is the chemical shift and the susceptibility effect will be discussed in a later section. The average shielding constant σ of pure water varies approximately linearly with temperature:

$$\sigma(T) = \alpha \cdot T \qquad [2.15]$$

where α is the chemical shift coefficient and was found to be about $-1.03 \pm 0.02 \cdot 10^{-8}/℃$ over a wide range in temperature varying from $-15℃$ to $100℃$ (22).

Therefore, one can compute the phase from equation [2.12] as follows:

$$\phi(T) = \omega \cdot TE = \gamma B_0 (1 - \alpha \cdot T) \cdot TE \qquad [2.16]$$

where TE is the echo time of the sequence used to acquire the images. Consequently, the temperature dependent change is measured by acquiring one or more images as baseline

images, which are subtracted from dynamic images acquired during the heating or cooling phase. Hence, the phase difference is given by:

$$\phi(T) - \phi(T_{ref}) = \alpha\gamma B_0 TE(T - T_{ref}) \quad [2.17]$$

which is proportional to the temperature-dependent PRF change and therefore can be converted to temperature change as:

$$\Delta T = T - T_{ref} = \frac{\phi(T) - \phi(T_{ref})}{\alpha\gamma B_0 TE} \quad [2.18]$$

2.3.2 Pulse Sequence Optimization

The phase is usually extracted from the images acquired using any fast gradient-echo sequences with RF-spoiling and where the contribution of the stimulated echoes is reduced to zero. RF-spoiling is necessary when short TR is used in conjunction with flip angle close to the optimal flip angle such as Ernst angle which provides the maximum signal intensity (better SNR). Unlike the gradient-echo sequences, the spin echo sequence or any variant of the spin echo sequences that obey the Call-Purcell-Meiboom-Gill (CPMG) conditions are not suitable for PRF temperature measurement; instead, a non-CPMG spin echo sequence with asymmetric echo (62) can provide the PRF temperature with a relatively good sensitivity. Although, the latter can be used for PRF temperature measurement; the most efficient and accurate pulse sequence used for PRF temperature measurement remains the spoiled gradient echo sequence.

In a GRE sequence, the temperature-dependent phase change $SNR_{\Delta\phi}$ is given by:

$$SNR_{\Delta\phi} = \frac{|\Delta\phi(T)|}{SD_{\Delta\phi}} \quad [2.19]$$

where $\Delta\phi(T)$ is the phase change and $SD_{\nabla\phi}$ is the standard deviation of the phase change. The phase images are reconstructed on the pixel-by-pixel basis by taking arctangent of the ratio of the imaginary and real images. This nonlinear operation results in a certain distribution of phase noise which is well described in (63). Hence, the standard deviation for the phase noise is given by:

$$SD_{\Delta\phi} = \begin{cases} \frac{SD_{SI}}{SI} & if\ SI \gg SD_{SI} \\ \sqrt{\frac{\pi^2}{3}} & if\ SI = 0 \end{cases} \quad [2.20]$$

where SD_{SI} is the standard deviation for the magnitude image noise and *SI* is the signal intensity of the magnitude image. Equation [2.20] shows, for $SI \gg SD_{SI}$, that the phase noise is inversely proportional to the SNR of the reconstructed magnitude image (63, 64). Therefore, equation [2.19] is proportional to the signal intensity as follows:

$$SNR_{\Delta\phi} \propto |\Delta\phi(T)| \cdot SI \quad [2.21]$$

Since the GRE signal intensity is a function of the tissue parameters such as: spin density ρ, T_1, and T_2^* as well as the sequence parameters (TE, TR, and the flip angle), thus the dependence of $SNR_{\Delta\phi}$ on TE can be written as:

$$SNR_{\Delta\phi} \propto TE \cdot e^{-\frac{TE}{T_2^*}} \quad [2.22]$$

Differentiating the above equation with respect to TE and setting the result to zero yields:

$$TE = T_2^* \quad [2.23]$$

which is the optimal TE value for better temperature-dependent phase imaging (65-67).

2.3.3 Temperature Imaging Using PRF

In MRI, the temperature information created using the PRF shift method is computed from the phase difference images on the pixel-by-pixel basis according to equation [2.18]. The phase difference allows the elimination of invariably unwanted contributions such as the gradient eddy current due to system imperfections, the chemical shift, and the magnetic susceptibility variations. These phase difference images can be calculated in two different ways:

1) One can create the phase of the individual images using the arctangent operation and then simply subtracting the base-line image from the subsequent dynamic images acquired during the heating. Actually, this technique presents a major problem that arises when the phase difference between the base-line image and the current image exceeds $\pm 2\pi$ and then phase wraparound appears. It is most likely that this will happen during a thermal procedure; therefore, it is crucial to use an unwrapping algorithm for computing the correct temperature map. Although two-dimensional phase unwrapping is in general a difficult problem, a description of a large number of different methods has been presented (68). Instead of this technique, it is convenient to compute the complex images first, before applying the arctangent operation to the ratio of the imaginary and real parts. In the remainder of this dissertation, this technique will be referred to as the complex phase subtraction.

2) To avoid the problem of the phase wraparound, the complex phase subtraction computes the phase difference between adjacent time frame images (67) as described by equation [2.24].

   Let Z_i be the complex-valued image pixel of the i^{th} time frame. Hence, the phase difference between the complex-valued image pixels i^{th} *and* $(i+1)^{th}$ is given by:

$$\Delta\phi = \arg(Z_i Z_{i+1}^*) = \arctan\left(\frac{Im(Z_i Z_{i+1}^*)}{Real(Z_i Z_{i+1}^*)}\right) \quad [2.24]$$

   where Im and $Real$ represent the imaginary and the real part of a complex number. Furthermore, equation [2.24] can be expressed in terms of the real and imaginary components of the image pixels:

$$\Delta\phi = arctan\left(\frac{Real(Z_{i+1})Im(Z_i) - Real(Z_i)Im(Z_{i+1})}{Real(Z_i)Real(Z_{i+1}) + Im(Z_i)Im(Z_{i+1})}\right) \quad [2.25]$$

   Finally, the total phase change from the reference to the current time frame is computed by adding together the phase change between adjacent time frames.

2.3.4 Factors Affecting PRF Accuracy

Although PRF method is a very reliable method for providing temperature with a good accuracy during a thermal procedure, its temperature accuracy can be corrupted by a number of factors such as the external field drift, the susceptibility changes, and the motion of the targeted sample. A brief description of these effects and how they influence the accuracy of the temperature is given in this section.

2.3.4.1 External Field Drifts

A drift of the external field is indubitably one of the effects that are associated with the limitation of the imaging hardware. The resulting extra phase shift causes incorrect reading of the temperature during thermal procedure and thereby affects the temporal stability of the PRF method. Therefore, a correction for the external field drift has to be made to obtain a correct temperature measurement. However, the extra phase shift created by a spatially uniform external field drift can be measured with a reference phantom that remains at a fixed temperature (69). In practice, the phase drift is not always uniform; therefore, a correction for linear phase drift can be applied by fitting a linear plane to at least three reference phantoms or several control regions (24).

2.3.4.2 Susceptibility Effect

The variation of the local magnetic field B_{loc} at the site of the nucleus with temperature is in general due to two different physical phenomena: the chemical shift and the susceptibility effect (70,71), and can be approximated by the following expression:

$$B_{loc}(T) \cong \left(1 - \frac{2\chi(T)}{3} - \sigma(T)\right) B_0 \qquad [2.26]$$

where σ is the chemical shift constant, and χ is the volume magnetic susceptibility which is also function of temperature. For the temperature range used in thermal therapy, the chemical shift constant as well as the susceptibility constant can be approximated as linearly related to temperature. However, if the above expression of B_{loc} is used to calculate the phase change in equation [2.17] and thus the temperature change, an important complication will arise from the fact that the change of the local magnetic field with temperature is also due to the

temperature dependence of the susceptibility constant. It has been shown that the susceptibility change with temperature is about $0.0026\,ppm/℃$ in pure water, $0.0016\,ppm/℃$ for muscle tissue in the temperature range of 30 to 45℃ (25), and from fat tissues where a large range of values have been reported starting from 0.0039 to 0.0094 ppm/^{o}C (25,72,73). However, whereas the temperature sensitivity of the chemical shift is significantly higher and nearly constant for all tissue types except the adipose tissue, the temperature dependence of the susceptibility is tissue-type dependent (74). The susceptibility also changes with the orientation and the geometry of the heat-delivery device and its associated heat pattern (75).

Because of the relative high temperature sensitivity of the chemical shift in tissue with high water content such as muscle tissue, the temperature dependence of the susceptibility constant does not have a significant effect on the thermometry applications. The errors induced by the susceptibility effect are less than 10% of the temperature variation (25). That is the reason why most implementations of PRF thermometry in aqueous tissue assume only the temperature change due to the chemical shift constant. However, temperature change due to the susceptibility effect becomes important when a large quantity of fat is present in a given sample, since the temperature dependence in fatty tissue is almost completely determined by the susceptibility effects. Therefore, a good fat suppression technique is required before computing PRF temperature map. However, fat suppression does not completely eliminate the effect of the fat susceptibility change on the PRF temperature in the voxels containing only aqueous tissue since the change has already occurred before the separation.

2.3.4.3 Effect of Motion

The PRF temperature measurement as described in equation [2.18] uses the phase difference between a base-line image acquired when no heating has been yet performed and a current image during the heating. The phase subtraction requires that the location of the complex-valued image pixel does not change from the reference image to the subsequent images acquired during the heating process, i.e., no motion during the acquisition of the different images. If motion is present between the acquisitions of the images, the images are not registered to the base-line and artifacts happen in the temperature images. This can be a very problematic issue for the application of the PRF method since many of the target areas for thermometry are in the abdomen, where motion is constantly present. The motions present are the respiratory motion, the blood flow, the heart motion, peristalsis, etc…

For example, motion of the liver has an average amplitude of 1.3 cm during normal breathing (76). However, the motion artifacts can be reduced by rapid imaging, triggering, and multiple breath holds. The latter can be very cumbersome to produce artifact-free temperature maps since the actual treatment durations in thermal therapy vary on the order of several minutes. To overcome the respiratory motions, others have used conventional respiratory gating in animals under anesthesia and mechanical respiration (77,78). Furthermore, a referenceless PRF method has been also proposed to reduce the effect of the motion on the PRF temperature (79). In addition to respiratory motion, thermal coagulation can also lead to structural changes and deformation of the treated area in the tissue (80,81), and this can be observed even in ex vivo experiment without any other source of motion present.

In summary the PRF temperature monitoring during in vivo thermal treatment can be

very challenging with the potential existence of these sources of motion. Actually, a lot of efforts have been put into the development of new motion insensitive imaging sequences and reconstruction algorithms to reduce or even eliminate the motion artifacts of the PRF temperature.

2.4 Proton Density

The proton density (PD) represents a quantitative distribution of the number of protons per unit tissue. It is linearly dependent on the equilibrium nuclear magnetization M_0, which is inversely proportional to the absolute temperature (3) according to equation [1.28]:

$$\mathrm{PD} \propto \mathrm{M_0} = \frac{\gamma^2 \hbar^2 \mathrm{N_I I(I+1) B_0}}{3\mathrm{k_B}} \cdot \frac{1}{\mathrm{T}} \qquad [2.27]$$

where $\mathrm{N_I}$ is the number of nuclear spin per unit volume, k_B is the Boltzmann's constant, and I is the quantum number of the spin system under investigation (I = ½ for hydrogen atom).

In an early work, Kamimura et al. proposed the use of the PD to quantify temperature in a copper sulfate solution (82). Young et al. (20) and Chen et al. (5) respectively studied the temperature dependency of the PD in muscle tissue and both muscle and adipose tissue. The temperature sensitivity of the proton density is small, about $-0.30 \pm 0.01\%/℃$ (4) between 37℃ and 80℃, therefore requiring high SNR, i.e., an SNR of 100 is required for 3℃ temperature uncertainty (5). In practice, the PD image is produced by selecting appropriate scan parameters such as a long TR ($TR \gg T_1$, typically about 10 seconds (28)) and short TE ($TE << T_2$) to minimize the effects of $\mathrm{T_1}$ and $\mathrm{T_2}$. The required long acquisition time and the low temperature sensitivity have made the PD method less useful for real-time applications.

2.5 Diffusion Coefficient

The temperature dependence of the diffusion coefficient is derived on the basis of the Stokes-Einstein relationship between viscosity and the translational self-diffusion coefficient D. The relationship is exponential and can be approximated as:

$$D \approx e^{-\frac{E_a(D)}{k_B T}} \quad [2.28]$$

where $E_a(D)$ is the activation energy of the molecular diffusion of water, k_B is the Boltzmann's constant, and T is the absolute temperature. Furthermore, temperature changes induce viscosity and diffusion coefficient changes, which can be calculated by differentiating equation [2.28] with the assumption that the activation energy is independent of temperature:

$$\frac{dD}{D} \approx \frac{E_a(D)}{k_B T^2} dT \quad [2.29]$$

From the above equation, a temperature map T can be deduced from two diffusion images: a reference image (D_0, T_0) and a dynamic image (D, T) acquired during the heating such as:

$$\frac{1}{T} = \frac{1}{T_0} - \frac{k_B}{E_a(D)} \ln\left(\frac{D}{D_0}\right) \quad [2.30]$$

The diffusion coefficient can be measured using MRI on the basis of the signal attenuation observed in the presence of a pair of strong mutually counteracting gradients. This was first demonstrated by Stejskal et al. in a seminal paper published in 1965 (17). Figure 2.2 illustrates a conventional "Stejskal-Tanner" spin echo pulse sequence.

The contrast in MRI associated with diffusion of water in tissue comes from additional dephasing accumulated by randomly moving spins along the direction of the diffusion

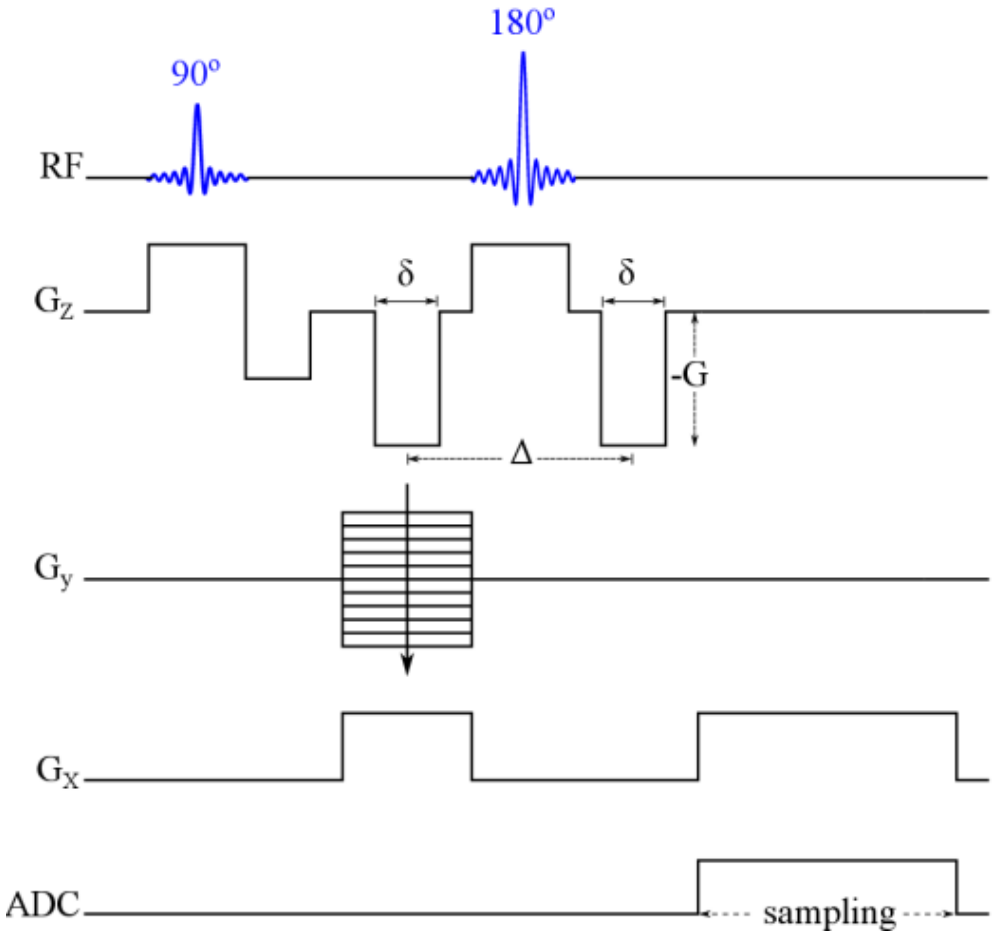

Figure 2.2: Timing diagram of the Stejskal-Tanner spin echo pulse sequence. The diffusion gradients are applied along the slice selection direction.

gradients and results in a Gaussian distribution of displacement. Therefore, an attenuation of e^{-bD} is observed where $b = -\gamma^2 G^2 \delta^2 \left(\Delta - \frac{\delta}{3}\right)$.

The temperature sensitivity of the diffusion method is about 2%/°C. Despite its good temperature sensitivity (21,83-86), practical issues such as relative long acquisition time and high sensitivity to motion may limit the real-time feasibility of the method in vivo. However, fast imaging sequence such as single-shot echo planar imaging (EPI) (87) and line-scanning techniques (18) have been used to reduce the acquisition time and the motion sensitivity. Another complication in vivo arises when the tissue condition changes, which results in the

nonlinearity of the diffusion coefficient with temperature. Therefore, the state of the tissue, the presence of lipid, and many more issues are to be considered when using the diffusion method to evaluate the temperature. For more information, the reader is referred to the well-detailed description of the diffusion method in (28,29).

2.6 Magnetization Transfer

In MRI, the magnetization transfer (MT) effect was accidentally discovered by Wolff et al. (88), while attempting to perform a spin transfer experiment by selective saturation of urea or carbamide ($CO(NH_2)_2$) looking for small signal suppression in water. Instead, they found a significant loss of image intensity, which is now known as MT, from the proton signal in tissue independently of the specific offset frequency of the RF pulse.

In general, protons in macromolecules are not visible in MRI because of their very short T_2^* relaxation time. However, coupling between the molecular protons and the mobile or 'liquid' protons allows the spin state of the macromolecular protons to influence the spin state of the liquid protons through exchange processes. Therefore, the saturation of the macromolecular spins can be transferred to the liquid spins, depending on the rate of the exchange between the two spin populations, and hence can be detected with MRI (89). MT techniques use a spectrally selective RF pulse to saturate protons in macromolecules and water molecules that are bound to macromolecules. This results in a decrease of MR signal in areas of macromolecules affected by magnetization transfer.

One universally agreed upon MT application is in magnetic resonance angiography (MRA) (90); the second major application is in the characterization of white matter disease in the brain such as multiple sclerosis (MS) (91-93). Since the MT exchange processes is

also temperature-dependent, it can potentially be used for temperature measurements (20,21). However, the sensitivity of MT with temperature appears limited and strongly tissue-dependent.

In conclusion, we have covered several MRI thermometry methods in this chapter. Each of the method presented herein has different temperature sensitivity and different temporal resolution which rendered some of the methods more popular than others. Among these MRI thermometry methods, PRF and T_1 appear very promising because of their temperature sensitivity and relatively high temporal resolution. However, all these methods suffer from motion artifacts; thus, fast pulse sequences in conjunction with efficient acquisition schemes need to be developed to overcome some of the limitations of the individual method.

CHAPTER III

HIGH INTENSITY FOCUSED ULTRASOUND: PHYSICS AND EFFECTS ON TISSUE

3.1 Introduction

As early as 1954, Lindstrom (94) and Fry (95) have conducted the first application of HIFU in humans by producing elevated acoustic intensities in vivo by focusing ultrasound energy in the manner analogous to the way that a converging optic lens focuses a light beam. Two decades later, the application of HIFU in clinical setting was again investigated, but at lower intensities for treating tumor (96). Although the concept was to induce elevated temperature (~ 43^{o}C) to the tissue at the location of the tumor for an extended time (~ 1 hour), this strategy did not work because of the lack of a noninvasive temperature measurement technique that allowed real-time feedback control of the delivered acoustic energy to the tumor. However, in 1980, the development of extracorporeal shockwave lithotripsy (ESWL) (97) led to the first clinical application of HIFU in 1984 for the treatment of kidney stones. In 1990, the treatment of tumor with HIFU resurfaced again with the development of MR thermometry. MR thermometry methods such as PRF can be used to guide and monitor a thermal treatment using HIFU to ensure that the desired region (tumor) is treated with minimal damage to the surrounding healthy tissue.

Ultrasound is a very versatile tool that has been used in therapeutic treatment, lithotripsy,

and targeted drug delivery. This chapter will describe the basic physics of ultrasound as well as its effect on biological tissue.

3.2 Basic Ultrasound Physics

3.2.1 Proprieties of Ultrasound Wave

Sound is a mechanical energy that is transmitted by pressure waves through a medium. Unlike electromagnetic radiation such as light and x-ray, mechanical pressure waves require an elastic deformable medium such as air, water, tissue, bone, etc. The periodic changes of the pressure of the medium are created by forces acting on the molecules, hence creating an oscillation about their mean unperturbed positions. There are several kinds of sound waves: infrasound, audible sound, ultrasound, and hypersound. Table 3.1 lists the typical frequency ranges of the different sound waves.

Furthermore, waves are divided into two types: longitudinal and transverse. Longitudinal waves are those in which molecules or particles oscillate back and forth along the direction of propagation of the wave energy. Ultrasound waves in liquid and tissue are longitudinal. In contrast, transverse waves are those in which the motion of the particles is perpendicular to the direction of propagation of the wave energy. Bone is the only biological tissue that does

Table 3.1: Typical frequency ranges of sound waves and their sources.

Designation	Range	Example
Infrasound	0 to 16 Hz	Seismic waves
Audible sound	16 Hz to 20 kHz	Speech, music
Ultrasound	20 kHz to 10 GHz	Bats, dolphins, navigation, and medicine
Medical Ultrasound	1 MHz to 15 MHz	Image Guided Therapy (IGT) system
Hypersound	10 GHz to 1 THz	Acoustic microscopy

not severely attenuate the propagation of such of transverse waves, which are sometimes referred to as shear waves or stress waves. The propagation of longitudinal waves through a medium creates regions of varying particle density: compression zones and rarefaction zones. Figure 3.1 illustrates the motion of these particles as function of time as the ultrasound wave propagates through the medium.

The propagation of the ultrasound wave does not generate a flow of particles; instead, the wave is transmitted over long distance because of the neighbor-to-neighbor interaction. This sinusoidal displacement of a medium can be represented by the following equation:

$$A(t) = A_0 \sin(2\pi f t) \qquad [3.1]$$

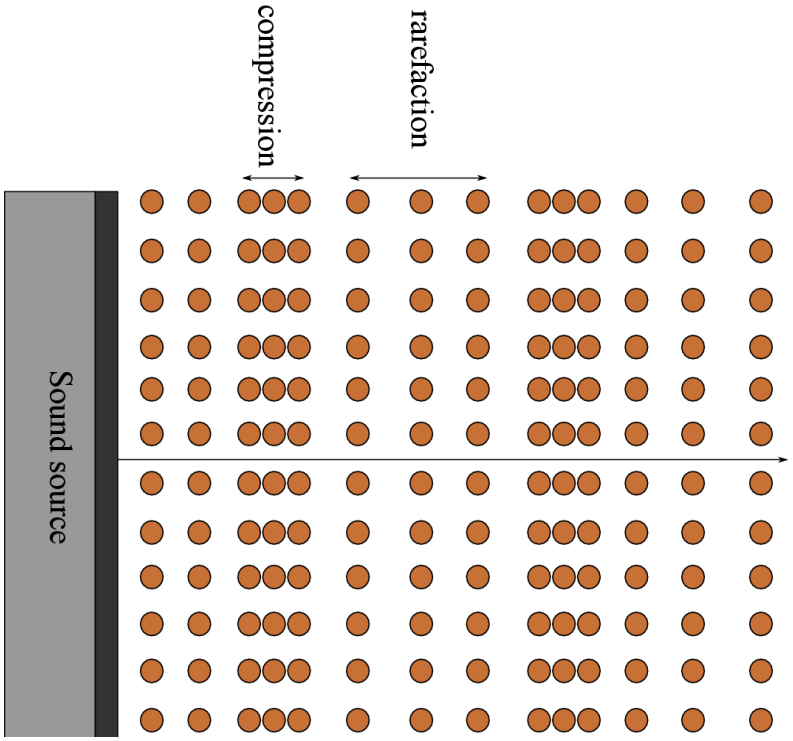

Figure 3.1: Particles density along a longitudinal path of the sound wave. Regions of high density (compression zone) and low density (rarefaction zone) alternate.

where A_0 is the peak displacement amplitude, f is the frequency, and t is the time. Hence, the particle's velocity in the medium is obtained by taking the derivative of equation [3.1]:

$$V(t) = V_0 \cos(2\pi f t) \quad [3.2]$$

where $V_0 = 2\pi f A_0$, the maximum amplitude of velocity.

However, it is important to note that the velocity of the particles in the medium is different from the acoustic velocity. Acoustic velocity c is the speed at which a wavefront propagates through the medium, which depends on the density and the compressibility of the medium as follows:

$$c = \frac{1}{\sqrt{\kappa \rho}} \quad [3.3]$$

where ρ is the density (mass of the medium per unit volume), and κ is the compressibility (fractional decrease in volume when pressure is applied to the medium). Furthermore, the acoustic velocity can be expressed as a function of the frequency (f) and the wavelength (λ) (98):

$$c = f\lambda \quad [3.4]$$

In most soft tissues, the average speed of sound is about 1540 m/s. In fat and lung tissue, ultrasound travels slower with velocities of 1480 m/s and 650 m/s, respectively. Bone has a speed of sound ranging between 1800 to 3700 m/s (99). Moreover, the speed of the sound slightly increases with temperature in soft tissues, except in fatty tissue where the speed of the sound decreases with increased temperature (99).

Ultrasound intensity, also known as acoustic power density, is a variable of interest and

can be defined as the time-average rate at which work per unit area is done across any plane through which sound is propagating. The time-average intensity is given by:

$$I = \frac{P_0^2}{2\rho c} \quad [3.5]$$

where P_0 is the pressure peak amplitude.

From the above equation, one can deduce the ultrasonic power, which is an average over one cycle period, as:

$$W_0 = I \cdot a \quad [3.6]$$

where a is the cross-sectional area of the beam.

3.2.2 Ultrasound Source: Transducer

Ultrasound in medical application requires frequencies in approximately the megahertz range as indicated in Table 3.1. Producing such ultrasonic waves requires a source known as a transducer. A transducer is any device that can transform one kind of energy into another. The transducer used to produce ultrasound transforms electric energy (electrical signal) to mechanical energy (ultrasound beam) and vice versa. The physics underlying the transducer construction relies on a phenomenon first studied by Pierre Curie in the 1880s known as the piezoelectric (pressure electric) effect (100). This effect is commonly found in crystals that have electric dipoles. If the crystalline materials are heated above the Curie temperature, the dipoles are released and can change orientation. Then, the transducer is ‘poled’ with an external electric field, causing the dipoles to align in a common direction. When cooled down, the crystal has maximum piezoelectric activity. For the detailed description of the

construction of the transducer, the reader is referred to (100).

When a voltage is applied to the piezoelectric element, the dipoles twist to align themselves with this electric field, thereby thickening the crystal. If the polarity is reversed, the dipoles will twist back in the opposite direction, thus creating a decrease in the crystal thickness. As a result of the expansion and the contraction of the crystal, a mechanical vibration is created that will transmit a mechanical wave into the nearest medium.

3.3 Interactions of Ultrasound with Tissue

The interactions of ultrasound with tissue are very similar to the wave behavior of light beams, such as reflection, refraction, absorption, etc. Most of these interactions (except absorption) reduce the ultrasound beam intensity by merely redirecting the energy of the beam. In the following subsections, we will describe some of these interactions with are relevant to the basic understanding of the interaction of the ultrasound beam with tissue.

3.3.1 Reflection

In ultrasound physics, the quantity that is similar to the momentum in classical physics is called the acoustic impedance. The acoustic impedance (Z) is a measure of the resistance of the sound passing through a medium. It is defined as the product of the particle density (ρ) times velocity (c):

$$Z = \rho c \qquad [3.7]$$

A difference in acoustic impedance or impedance mismatch between two media is the cause of the reflection of some of the incident beam. If the impedances are equal, the sound will be readily transmitted from one medium to another without any discontinuity. The angle of

incidence of the ultrasound beam is the same as the angle of reflection. Figure 3.2 illustrates the reflection of an ultrasound beam at the interface of two media.

For a perpendicular angle of incidence, the reflection coefficient, which is the ratio of the reflected pressure amplitude to incident pressure amplitude, is given by equation [3.8].

$$R = \left(\frac{Z_2 - Z_1}{Z_2 + Z_1}\right)^2 \qquad [3.8]$$

3.3.2 Refraction

The refraction of the ultrasound beam obeys Snell's law, which is given by

$$\frac{c_i}{c_t} = \frac{\sin\theta_i}{\sin\theta_t} \qquad [3.9]$$

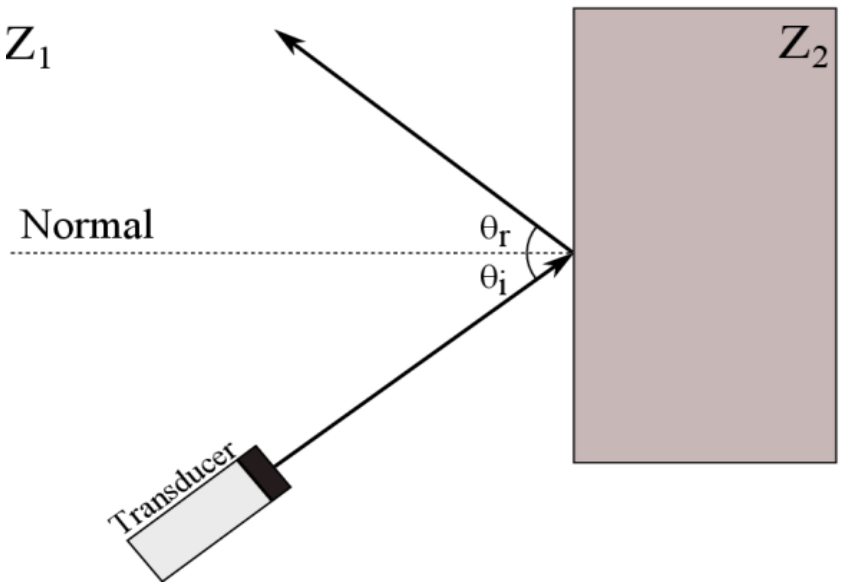

Figure 3.2: Reflection of ultrasound beam at the interface between two media with impedances Z_1 and Z_2, respectively. The angle of incidence $\boldsymbol{\theta_i}$ is equal the angle of reflection $\boldsymbol{\theta_r}$.

where c_i and c_t are the velocities of the ultrasound wave in the incident and transmitted media, respectively, and θ_i and θ_t are the incident and transmitted angles as defined in Figure 3.3. The transmission coefficient can be obtained from the reflection coefficient as follows:

$$T = 1 - R = \frac{4Z_2Z_1}{(Z_2 + Z_1)^2} \quad [3.10]$$

Figure 3.3 shows the ultrasound beam path from medium 1 to medium 2.

3.3.3 Absorption

Absorption is the process whereby the acoustic energy is transformed to other forms of energy, particularly heat. This process is the principal force driving the application of ultrasound in therapeutic medicine. The absorption of the ultrasonic beam is a function of the

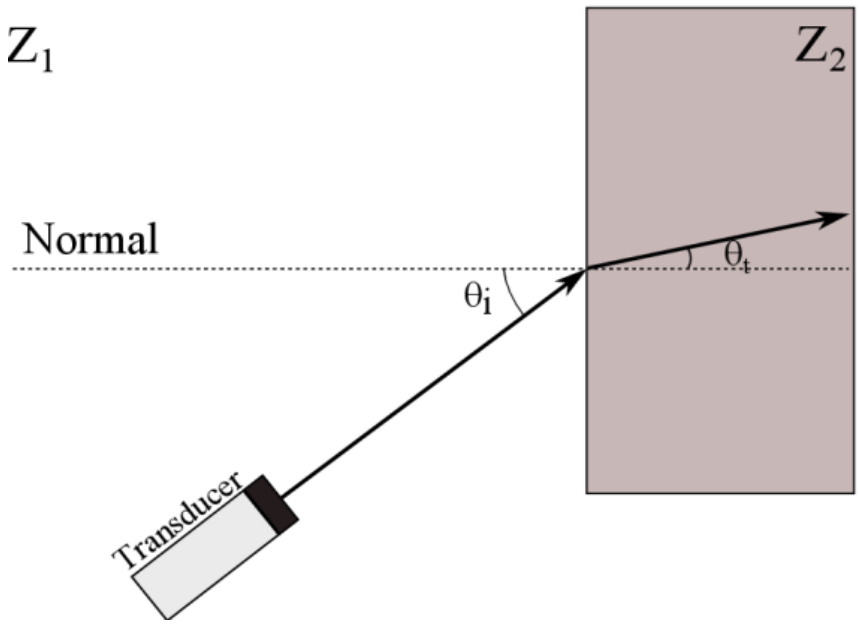

Figure 3.3: Ultrasound beam is transmitted from medium 1 to medium 2. The velocity of the sound is greater in medium 1 than medium 2.

sound frequency, the viscosity, and the relaxation time of the medium. The relaxation time herein refers to the rate at which the molecules return to their equilibrium position after being displaced by the ultrasound wave force and the viscosity is the ability of the molecules to move past one another, which is usually accompanied by a production of heat due to the friction between molecules. Increased frequency generates more heat, since the molecules have to move more often, and thereby, the drag caused by the friction will create more heat. The absorption of ultrasonic beam in tissue follows an exponential function:

$$P = P_{max} e^{(-\alpha x)} \qquad [3.11]$$

where P is the peak pressure amplitude of the beam at depth x, P_{max} is the initial peak pressure of the beam, and α is the pressure absorption coefficient. The absorption coefficient depends on the frequency of the ultrasound beam and the medium. Equation [3.11] can be rewritten as a function of the attenuation coefficient (a), which is the sum of the absorption coefficient (α) and the scattering coefficient (a_s). In biological tissues, the absorption losses were found to dominate total attenuation (99,101).

Phased-array transducers are often used in HIFU applications because they allow electronic steering of the beam inside the tissue regions. The description of the mechanism of focusing a phase-array transducer is beyond the scope of this dissertation.

In summary, HIFU is a noninvasive modality that can target a deep-seated tumor with minimal damage to the surrounding tissue. Ultrasound physics is well understood and can be used to manufacture efficient transducers. Although there is much more to the theory of ultrasound physics then can be covered here, understanding of these basic principles is sufficient for understanding the works presented in this dissertation.

CHAPTER IV

MODIFIED TURBO SPIN ECHO SEQUENCE-BASED THERMOMETRY

*This chapter is based on a paper titled "*Modified Turbo Spin Echo Sequence Based Thermometry*" authored by Mahamadou Diakite, Rock Hadley, and Dennis L. Parker. The paper was submitted to the journal of Magnetic Resonance in Medicine (MRM) in June 2011.*

4.1 Abstract

The purpose of this study was to show the feasibility of proton resonance frequency shift-based thermometry using a modified Turbo Spin Echo sequence. The Turbo Spin Echo sequence is known to have high specific absorption rate that may cause tissue heating. It is therefore of interest to try to measure temperature with the Turbo Spin Echo sequence. Despite the obvious advantage of Turbo Spin Echo in terms of speed and high signal-to-noise ratio, the implementation of imaging procedures that rely on induced phase (flow, chemical shift) are more difficult because of the required maintenance of the Carr-Purcell-Meiboom-Gill conditions in Turbo Spin Echo. Hence, we present a modified Turbo Spin Echo sequence to generate phase maps, in which the proton resonance frequency shift is detected. The sequence was tested by acquiring images from a heated agarose gel phantom during the cooling phase. We measured the temperature change caused by the high specific

absorption rate of the Turbo Spin Echo sequence by imaging a homemade phantom with conductivity adjusted to mimic the conductivity properties of most biological tissue. The calibration experiment shows a good correlation between the fiberoptic temperature reading and the phase change. Since the time offset τ between the echo time and the time of the spin echo is less T_2^* of our phantom, we predicted a relatively noisy temperature map. However, we have shown that the modified Turbo Spin Echo sequence can be used to monitor temperature and could be used to quantify heating effects in suspect Turbo Spin Echo studies.

4.2 Introduction

The Turbo Spin Echo (TSE) sequence also known as RARE (Rapid Acquisition with Relaxation Enhancement) or FSE (Fast Spin Echo) has become increasingly popular for clinical diagnosis. Its superior image quality and short scan time compared to the conventional spin echo sequence makes it the favorite sequence for T_2-weighted imaging (31,102). However, one of the major drawbacks of the TSE sequence is its high RF power deposition. The specific absorption rate (SAR) of TSE sequence can be particularly high because multiple RF pulses are played out over a very short time. Therefore, with the recent developments in high field ($B_0 \geq 3T$) imaging, SAR management becomes a particularly important issue.

Homogeneous tissue models have long shown that the SAR varies approximately as the square of both the field strength B_0 and the sample radius, with maximum local SAR and heating at the surface (103). In fact, the mechanism for heating is the induction of eddy currents due to the nonzero conductivity of tissue according to Faraday's law. Thus, when the

SAR exceeds the thermal regulation capability of the tissue, temperature of the tissue will rise. Therefore, with the potential for temperature rise of the tissue associated with the usage of the TSE sequence, it would be advantageous to use TSE sequences for MRI thermometry.

Several MRI properties exhibit temperature dependence and have been used in MRI thermometry, such as T_1 relaxation time, the diffusion coefficient of water, and the proton resonance frequency shift (28,104). Among these techniques, the PRF method possesses many attributes that are advantageous for temperature mapping. It has good temperature sensitivity, linearity, reversibility with temperature during heating and cooling, and is easy to implement. The PRF thermal coefficient α has been shown to be independent of tissue type when measured ex vivo (105). It is also generally assumed that the water PRF shift to lower frequency with higher temperature is caused by rupture, stretching, or by a small amount of bending of the hydrogen bonds. Hence, these shifts are evidence of an increased average shielding constant of the proton (24,25,60). The fast gradient echo sequence and its variants are the most commonly used sequences for PRF shift-based thermometry. This is because the gradient reversal in fast gradient echo sequences refocuses only those spins that have been dephased by the action of the gradient itself; dephasing of spins due to magnetic field inhomogeneities is not reversed. In spin echo sequences, the spins are reversed by the 180^o pulse, and thus the SNR ratio is higher.

Despite the obvious advantages of TSE in terms of speed and high SNR, the implementation of imaging procedures that rely on an induced phase shift (flow, chemical shift) are more difficult because of the requirement of the CPMG conditions in TSE (106-108).

In this work, we present a modified TSE sequence to generate a phase map, in which the

proton resonance frequency shift is detected.

4.3 Materials and Methods

Spin echo sequences are primarily designed to be less sensitive to off-resonance effects, such as B_0-field inhomogeneity and tissue magnetic susceptibility variation. Thus, their readout windows are most commonly centered on the peak of the spin echo to reduce sensitivity to off-resonance effects. This symmetry condition prevents the usage of TSE sequences in MRI thermometry.

In principle, any spin echo-based technique can be used to measure temperature if the readout is made asymmetric such that the center of the gradient echo in the readout is shifted away from the time of the spin echo. In that case, the frequency offset due to the temperature change will cause a non-zero temperature dependent phase at the time of the gradient echo. This phase shift, $\Delta\phi$, will equal the frequency shift times the time offset τ:

$$\Delta\phi = \gamma\alpha B_0 \tau \Delta T \qquad [4.1]$$

where γ is the gyromagnetic ratio, α is the PRF-thermal coefficient, B_0 is the main magnetic field, and ΔT is the temperature difference.

The PRF shift method relies on the subtraction of a baseline phase image acquired before heating from subsequent phase images that are acquired during the course of the heating experiment. Thus, phase-image subtraction is necessary to exclude nonthermal contribution to the phase, such as phase change due to B_0 field inhomogeneities, and leaving only the spatially resolved phase-shift attributable to temperature-induced shift in the PRF.

The proposed sequence, depicted in Figure 4.1, is a modified TSE sequence that is rendered sensitive to off-resonance.

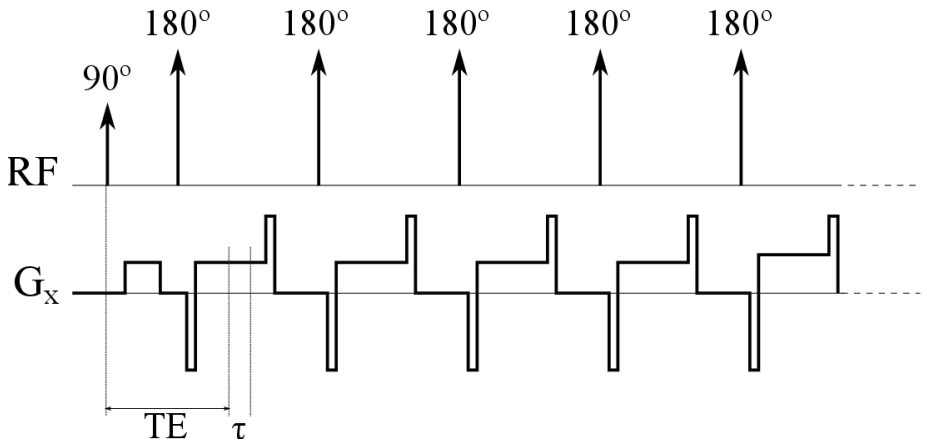

Figure 4.1: Modified Turbo Spin Echo sequence as implemented at 3T. The readout gradient lobe has been modified such as the echo is shifted by $\boldsymbol{\tau}$ away from the time of the spin echo.

4.4 Calibration Experiments

We verified experimentally the linear relationship between the phase change $\Delta\phi$ and the temperature change ΔT via calibration experiments. The calibration experiments were performed by continuously acquiring images from a heated agarose gel phantom during the cooling phase and a twin agarose gel phantom at room temperature used as a reference phantom. The phantom was uniformly heated in a water bath up to 70°C. The two agarose gel phantoms were taped together with an insulating Styrofoam block placed between them to prevent heat transfer between the phantoms, and they were placed within the 16 channel Siemens head coil (Siemens Medical Solutions, Erlangen, Germany). To validate our MR measurements, fiberoptic temperature probes (OpSens, Inc, Quebec, Canada) were positioned in the agarose gel phantoms during the data acquisition. Phase images of the reference phantom were used to correct for the B_0-field drift during the data processing. All MR imaging was performed on the Siemens TIM TRIO 3T MRI scanner (Siemens Medical Solutions, Erlangen, Germany) with the following parameter sets: repetition time TR = 3000 ms, echo time TE = 61 ms, time offset τ = 2.2 ms, 180° refocusing pulse, turbo factor of

129, image matrix = 256x129 and 2.4x1.2x3 mm resolution. Figure 4.2 shows a plot of phase change versus temperature change from a 5x4 voxel ROI near the tip of the temperature probe.

4.5 Heating Experiments

The goal of the heating experiment was to determine the temperature change induced within a phantom by the high SAR of the TSE sequence. For this purpose, a 2 liter phantom was made with the following recipe: 1.5 liter of H_2O, 160 ml of n-propanol, 7.2 g of NaCl, 2.5 g of $CuSo_4$, and 56 g of agarose. The above solution had a conductivity of 0.008 S/cm which satisfactorily mimicked the conductivity properties of most tissue (109). The copper sulfate is mainly used to shorten the relaxation time of the solution. The combination of these solutes also resulted in a solution with a T_1 of less than 200 ms at 3T. A 5.5x5.5 cm^2 resonating coil loop with no cable attached and no passive decoupling such that the loop was resonating during both transmit and receive, taped against the side of the phantom, was used

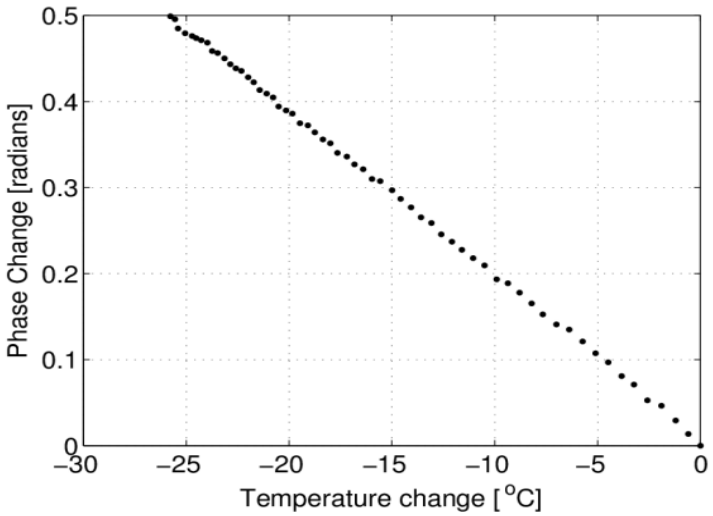

Figure 4.2: Calibration curve of the modified TSE sequence. Plot of MR phase change versus temperature change. The absolute temperatures were acquired using a fiberoptic temperature probe.

to focus RF energy from the transmit coil into the phantom near the resonating coil loop. The coil loop had no measurable effect on the phase difference used for temperature measurements. MR images were acquired with the same parameter sets as the calibration experiment except the image matrix, which was reduced to 256x126, the turbo factor was 7, and the scan time was 30 minutes and 26 seconds for 32 measurements. Figure 4.3 shows the temperature maps of a single slice after the first and the last measurement.

4.6 Data Processing

For this work, all MR image reconstruction and postprocessing were performed off-line. Phase difference images were calculated using MATLAB (version 7.8.0.347 (R2009a), Math-works, Inc, Natick, MA) running on a standalone desktop computer. To avoid phase wraparound errors that would occur at sufficiently high temperature, a phase difference image $\Delta\phi_i$ was constructed on a pixel-by-pixel basis from each image, i, acquired during the heating cycle such as:

$$\Delta\phi_i = tan^{-1}\left(\frac{Real(SI_i)\cdot Im(SI_{i+1}) - Real(SI_{i+1})\cdot Im(SI_i)}{Real(SI_{i+1})\cdot Real(SI_i) + Im(SI_{i+1})\cdot Im(SI_i)}\right) \qquad [4.2]$$

where $Real$ and Im are the real and imaginary components of the complex image SI. For continuous heating experiments where images are acquired in very closed interval from each other, this technique prevents the phase difference from exceeding $\pm 2\pi$. However, the temporal history of each pixel was examined and compensated when 2π discontinuities of the phase difference images were encountered. Magnitude images were used as masks to remove background noise in the phase and temperature images.

Figure 4.3: Temperature maps. a) Single slice after the first measurement. b) Same slice after the last measurement.

In the calibration experiments, a 3x3 region of interest (ROI) adjacent to the fiberoptic temperature probes was chosen in the phase images of the phantoms to evaluate the phase difference corresponding to the temperature change obtained from the fiberoptic probes. The PRF-thermal coefficient α was calculated from the linear regression coefficient according to equation [4.1]. The linear regression coefficient was derived from linear regression analysis between the temperature change obtained from the fiberoptic reading and the temperature-induced phase difference of the average of the ROIs.

4.7 Results

Images of the phantoms were continuously acquired every 2 minutes over 2 hours. The images of the phantoms are relatively blurred, which is caused by the long echo train (ETL) of 129 used to image the phantom. Figure 4.2 is a scatter plot of the phase change versus the temperature change in the heated agarose gel phantom where the slope of the regression line was found to be -0.019426 radians/ºC with a correlation confidence $r^2 = 0.9991$. The PRF-thermal coefficient α was calculated to be 0.011ppm/°C. The phantom in the heating experiment was designed to mimic tissue with high conductivity and therefore was expected to give the largest phase-shift offset. In the results shown in Figure 4.3, there is a clear

difference between the temperature map of a single slice after the first measurement and the temperature map of the same slice after 30 minutes of continuous scanning with the modified TSE sequence.

Figures 4.4 shows the plots of the mean values of phase and corresponding temperature change over a 16x11 pixel ROI chosen within the phantom and near the resonating coil loop during the course of the 32 measurements.

4.8 Discussions

The results obtained herein demonstrated the feasibility of proton resonance frequency shift-based thermometry with a modified TSE sequence. We have shown by shifting away the center of the readout echo from the time of the spin echo that the TSE sequence can be rendered sensitive to off-resonance effects, thus making it useful for MR thermometry.

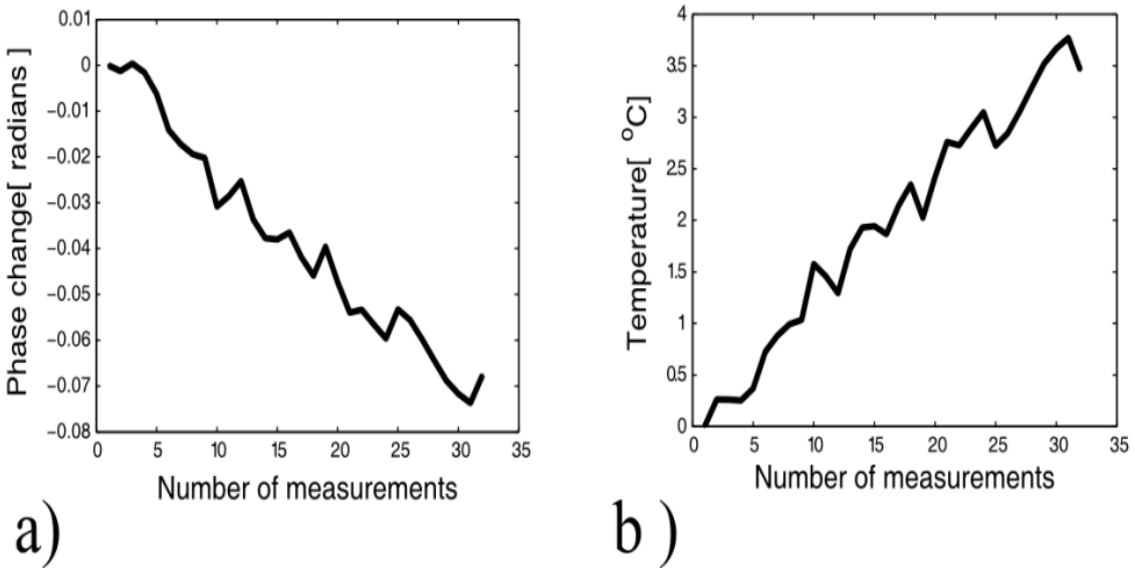

Figure 4.4: Phase and temperature plots. a) Plot of the mean values of 16x11 voxels ROI chosen within the phantom versus the number of measurements. b) Plot of the Corresponding temperature change versus the number of measurements within the same ROI.

Although the derived value of the PRF-thermal coefficient is slightly different from the expected value -0.01 ppm/ºC, the calibration curve shows a good correlation between the fiberoptic temperature reading and the phase change. The relatively high value of the PRF-thermal coefficient α can be explained by the relatively low value of the time offset τ (62,110). We did not consider experiments to determine the optimal echo time of this specific type of sequence, which could result in a compromise between the best achievable SNR and the best temperature sensitivity. However, it has been shown for gradient echo sequences that the optimum τ value for PRF thermometry is on the order of T_2^* of the phantom (111). Therefore, the sensitivity of the PRF shift method increases with the value of the time offset τ. Since τ is less than T_2^* of our phantom, we predicted a relatively noisy temperature map; however, these heating experiments demonstrated the temperature sensitivity of the TSE sequence.

Even though this experiment relied on a phantom temperature rise that was artificially induced using a resonating coil loop to focus RF energy from the transmit coil to the phantom, the ability to measure temperature using TSE sequences has been demonstrated. It is possible that for some subjects or sample geometries, enough power from the multiple RF pulses in the TSE sequence may be absorbed to result in some measurable tissue heating. In such cases, this TSE sequence applied with the same RF pulse protocol, but with a sufficient field of view to cover the object, should be able to detect the location of tissue heating. The modified TSE sequence, apart from having a short time offset τ which is imposed by the duration of the readout window, does not alter the speed or the high SNR of the standard TSE sequence. Therefore, the modified TSE sequence is expected to enable reasonable temperature measurements for the evaluation of any possible heating associated

with TSE sequences.

4.9 Conclusion

Although the proposed modified TSE sequence is in an early stage of development, we have shown that the TSE sequence can use the proton resonance frequency shift to monitor changes in temperature by shifting the gradient echo away from the spin echo. It could be hypothesized that this sequence will prevent short-term chemical shift instability which could cause spatial inconsistency of the thermal image. Temperature sensitivity improvement of the modified TSE sequence and a full comparison with the available thermometry sequences will be investigated in future work.

CHAPTER V

IRREVERSIBLE CHANGE IN THE T_1 TEMPERATURE DEPENDENCE WITH THE THERMAL DOSE USING THE PRF-T_1 TECHNIQUE

*This chapter is based on the paper titled "*Irreversible Change in the T_1 Temperature Dependence with the Thermal Dose Using the PRF-T_1 Technique*" authored by Mahamadou Diakite, Allison Payne, Nick Todd, and Dennis L. Parker. The paper is published in the journal of Magnetic Resonance in Medicine (MRM). Volume 69, issue 4, page 1122-1130, April 2013 (Reprinted with permission).*

PRECLINICAL AND CLINICAL IMAGING – Full Papers

Magnetic Resonance in Medicine 69:1122–1130 (2013)

Irreversible Change in the T_1 Temperature Dependence with Thermal Dose Using the Proton Resonance Frequency-T_1 Technique

Mahamadou Diakite,[1,2]* Allison Payne,[2] Nick Todd,[2] and Dennis L. Parker[2]

Denaturation of macromolecules within the tissues is believed to be the major factor contributing to the damage of tissues upon hyperthermia. As a result, the value of the spin-lattice relaxation time T_1 of the tissue water, which is related to the translational and rotational rates of water, represents an intrinsic probe for investigating structural changes in tissues at high temperature. Therefore, the goal of this work is to investigate whether the simultaneous measurement of temperature and T_1 using a hybrid proton resonance frequency (PRF)-T_1 measurement technique can be used to detect irreversible changes in T_1 that might be indicative of tissue damage. A new hybrid PRF-T_1 sequence was implemented based on the variable flip angle driven-equilibrium single-pulse observation (DESPOT)$_1$ method from a standard three dimensional segmented echo-planar imaging sequence by alternating two flip angles from measurement to measurement. The structural changes of the heated tissue volumes were analyzed based on the derived T_1 values and the corresponding PRF temperatures. Using the hybrid PRF-T_1 technique, we demonstrate that the change of spin lattice relaxation time T_1 is reversible with temperature for low thermal dose (thermal dose $\leq$ 240 cumulative equivalent minutes [CEM] 43°C) and irreversible with temperature after significant accumulation of thermal dose in ex vivo chicken breast tissue. These results suggest that the hybrid PRF-T_1 method may be a potentially powerful tool to investigate the extent and mechanism of heat damage of biological tissues. **Magn Reson Med 69:1122–1130, 2013.** © **2012 Wiley Periodicals, Inc.**

Key words: T_1 mapping; MR thermometry; focus ultrasound; thermal dose; chicken breast

Focused ultrasound surgery has been investigated for noninvasive destruction of deep-seated tumors for more than half a century (1,2). The effort to use high-intensity focused ultrasound surgery (HIFU) as a modality for cancer treatment has been hindered by the lack of reliable treatment monitoring and guidance. Using MRI, it has become possible to define the tissue to be treated, measure induced temperature changes in the tissue (3–5), and ensure proper targeting by localizing subthreshold heating (6). However, there is currently no good way to assess the extent of biological tissue damage during the treatment process. Three methods are commonly used to predict or assess tissue damage (7): the first method uses the power output of the treatment device and the exposure duration to predict tissue damage (8–12). The second method postulates a critical temperature, T_c, above which tissue damage occurs (13). The third method uses the entire temperature history of the tissue to estimate the thermal dose (14). Because it is believed that denaturation of macromolecules within the tissues is the major factor contributing to the damage of tissues upon hyperthermia (15,16), a fourth method to assess tissue damage might be the longitudinal relaxation time (T_1) of the tissue water, which is related to the translational and rotational rates of water and depends directly on the fraction of bound water. As water in biological tissues exchanges freely with the fraction of water that is bound to macromolecules including protein, fibers, and membranes, T_1 represents an intrinsic probe for investigating the structural changes in tissues at high temperature.

The water proton resonance frequency (PRF) shift is the currently accepted method to quantify temperature rises in aqueous soft tissues (4,17,18). PRF shows little dependence on the tissue changes that occur when the tissue is rapidly heated, such as with HIFU. The linearity of the PRF shift above the tissue necrosis threshold allows the tissue temperature to be estimated during the therapeutic ultrasound exposure.

The goal of this work is to investigate whether a hybrid PRF-T_1 measurement technique can be used to detect irreversible changes in tissue T_1 that might be indicative of tissue damage during an MRgHIFU procedure. A new hybrid PRF-T_1 sequence was implemented based on the variable flip angle (FA) DESPOT_1 method (19) from a standard three dimensional (3D) segmented echo-planar imaging (EPI) sequence by alternating two FAs every other image. Evidence for structural changes of the heated tissue volumes was inferred based on changes in the relationship between derived T_1 values and the corresponding PRF temperatures. These changes were compared with thermal dose measurements calculated using the Sapareto and Dewey (14) method.

THEORY

A conventional 3D segmented EPI sequence was modified to simultaneously determine the PRF shift and the

[1]Department of Physics & Astronomy, University of Utah, Salt Lake City, Utah, USA.

[2]Department of Radiology, University of Utah, Salt Lake City, Utah, USA.

Grant sponsor: The Ben B. and Iris M. Margolis Foundation; Grant sponsor: Siemens Medical Solutions; Grant sponsor: NIH; Grant number: R01 CA134599.

*Correspondence to: Mahamadou Diakite, B.S., UCAIR, Department of Radiology, 729 Arapeen Dr, Salt Lake City, Utah 84108.
E-mail: bijoumd@hotmail.com

Received 4 January 2012; revised 4 April 2012; accepted 11 April 2012.

DOI 10.1002/mrm.24322
Published online 10 May 2012 in Wiley Online Library (wileyonlinelibrary.com).

spin-lattice relaxation time, T_1, in all of the experiments presented in this work.

Measurement of T_1 Using the Variable Flip Angle Method

The variable flip angle method (19) using a 3D segmented EPI approach for T_1 measurement is based on the ideally spoiled steady-state gradient echo signal. When two measurements are made at different FAs, the signal equation canb el inearizeda nd T_1 extracted as described in Ref. 19. The two FAs should be chosen carefully to optimize precision of the measurement. Deoni et al. and Schabel et al. have each shown that the precision is best when the FAs are chosen such that they are on either side of the Ernst angle and each produces a signal that is 0.71 times the signal produced at the Ernst angle (19–21). The accuracy of the measurement is compromised when the actual FAs achieved in the region of interest (ROI) do not correspond with the nominal FAs prescribed by the user. This is often the case in practice due to inhomogeneities in the B_1 field and therefore a B_1 field map for correcting these variations needs to be obtained before the measurement. In this work, this was done using the double FA method (20).

$$\alpha_{\text{actual}} = \arccos\left|\frac{\text{SI}_{2\alpha}}{2 * \text{SI}_{\alpha}}\right| \quad [1]$$

Measurement of PRF Shift

The phase difference images are proportional to the temperature dependent PRF change and the echo time (TE). The phase difference can be converted to a temperature change as (22):

$$\Delta\text{T} = \frac{\Delta\Phi}{\gamma * \beta * B_0 * \text{TE}} \quad [2]$$

Where, γ is the gyromagnetic ratio, β is the apparent PRF-thermal coefficient, B_0 is the main magnetic field, and $\Delta\Phi$ is the phase change. The basic (nonreferenceless) PRF shift method relies on the subtraction of a baseline phase image acquired before heating from subsequent phase images that are acquired during the course of the heating experiment. This phase-image subtraction is necessary to exclude nonthermal contributions to the phase (e.g., phase due to radiofrequency [RF] coil sensitivity or B_0 field inhomogeneities) leaving only the spatially resolved phase-shift attributable to temperature induced shift in the PRF. The TE can be optimized to increase the phase contrast-to-noise ratio and thereby the temperature accuracy.

Pulse Sequence Design

To simultaneously calculate the PRF shift and the relaxation time, T_1, a new hybrid PRF-T_1 sequence based on the variable FA method described above was implemented from a standard 3D segmented EPI sequence. The modified 3D segmented EPI sequence consists of two FA's that alternate from measurement to measurement. Hence, the complete temperature maps can be acquired in either one or two measurements for PRF and T_1 methods, respectively.

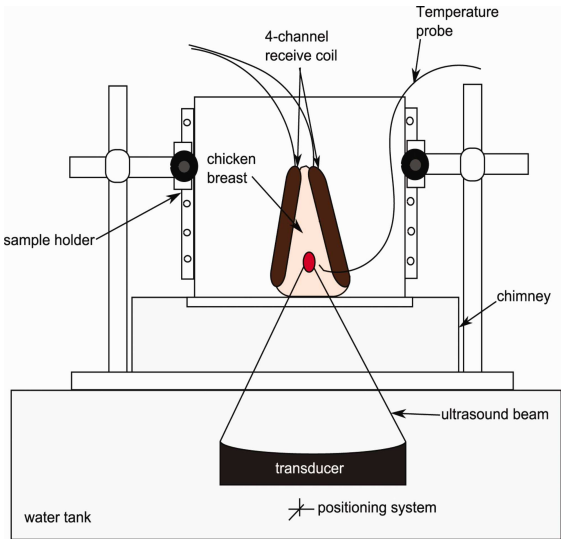

FIG. 1. Experiment setup. The chicken breast, sandwiched between the 4-channel receive coils, was placed within the sample holder container. A chimney filled with degassed water ensured an acoustic beam path to the tissue sample. A fiberoptic temperature probe was positioned near the focus to record temperature changes in real time. [Color figure can be viewed in the online issue, which is available at wileyonlinelibrary.com.]

METHODS

Experimental Setup

All imaging experiments were carried out on a Siemens TIM Trio 3T MRI scanner (Siemens Healthcare, Erlangen, Germany), using in-house built 4-channel RF receive surface coils. Multiple HIFU heating experiments were performed on ex vivo chicken breast tissue samples. Special care was taken to avoid any chicken breast with fat layers susceptible to corrupt the temperature measurement data. A 256-element MRI compatible phased-array ultrasound transducer (Imasonic, Besançon, France) was housed in a bath of deionized and degassed water. The transducer (1 MHz, 13 cm focal length) was mounted in a computer-controlled, mechanically driven, MRI compatible positioning system (Image Guided Therapy, Bordeaux, France). The ultrasound power was controlled outside the MR room via the controller computer. The tissue sample was sandwiched between the 4-channel RF receive coils for better imaging signal-to-noise ratio (SNR) at the ultrasound focus and was placed in a sample holder container. To provide proper acoustic coupling, a layer of degassed water was poured between the bottom of the container made of Mylar film and the tissue sample. After obtaining high-resolution images of the sample, a fiberoptic temperature probe (OpSens, Inc, Quebec, Canada) was positioned near the focus but outside of the direct ultrasound beam path. Figure 1 shows a diagram of the experimental setup. The whole unit fit inside the bore of the magnet and heating was performed simultaneously with MR imaging with no apparent artifacts.

Spin-Lattice Relaxation Time T_1 and Temperature Imaging

A series of three experiments, using three separate chicken breast samples, was conducted. In each experiment, the

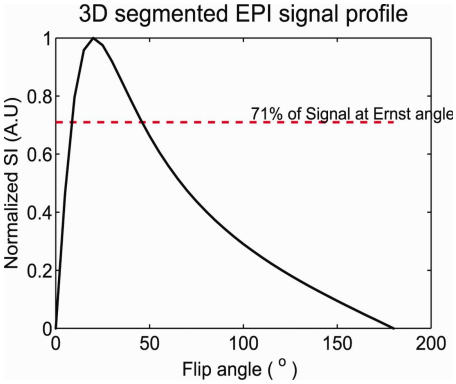

FIG. 2. Plot of the normalized signal intensity (SI) of the 3D segmented EPI versus the FAs. The maximum relaxation time T_1 precision is achieved by choosing the FAs such that: $SI(\alpha_1) = SI(\alpha_2) = 71\%$ of the signal intensity at Ernst angle α_E. [Color figure can be viewed in the online issue, which is available at wileyonlinelibrary.com.]

prescribed (nominal) FAs that would result in the best precision in T_1 measurements were empirically determined by measuring the signal intensity averaged over a large ROI using the PRF-T_1 sequence with a range of FAs from 5 to 95° in 10° increments. The two optimum FAs were derived from the plot of the normalized signal intensity versus the nominal FAs (see Fig. 2) as described in Ref.19. Furthermore, to minimize error in T_1, the FA map of each optimum FA was obtained using the steps described earlier (Eq. 1). For all experiments, the HIFU heating parameters are given in Table 1.

To supplement the PRF-T_1 method, a conventional inversion recovery (IR) spin echo pulse sequence (pulse repetition time [TR]/TE = 4100/17 ms, 2 × 2 × 2m m resolution, 128 × 64 image matrix, echo train = 11, inversion time = [50 200 400 800 2000 2500 3000]) was used for T_1 mapping of the chicken breast before and after the entire HIFU heating series. The values of T_1 obtained were used to verify any permanent change in T_1.

Experiment 1

The first experiment determined how T_1 changes with temperature over time (23,24), Two separate HIFU heating runs were performed. Our 3D hybrid PRF-T_1 sequence was used to acquire images during the heating and the cooling phases. Scan parameters for both heating runs were: TR/TE = 40/7 ms, readout bandwidth = 752 Hz/pixel, echo train length = 5, image matrix = 128 × 64, 12 slices, and 2 mm isotropic resolution for a scan time of 8.3 s per measurement. The empirically determined optimum FAs for this sample with these parameters were 3° and 20° respectively. Although, TE = T_2^* is the optimal TE for PRF temperature imaging [25 msec in muscle (25)], a shorter TE was used to increase the image SNR for improved accuracy of T_1 measurements and to potentially avoid exceeding 2π with the temperature-dependent phase shift at high-temperature elevation. To induce a uniform temperature rise in the target region, both heatings used a spiral trajectory (r = 2 mm, 19 focal points, 100 msec/point).

Experiment 2

Experiment 2, was designed to determine the repeatability of T_1 changes with temperature over time before permanent tissue damage occurs (thermal dose ≤ 240 cumulative equivalent minutes at 43°C [CEM_{43}]). Multiple sonications were applied at a single location in the chicken breast. Sonications were first applied at a relatively low-power level (5 acoustic watts for 20 s). The temperature information acquired during this sonication was scaled to find the power needed to produce the desired thermal dose in the subsequent heating runs. A series of 10 sonications were applied at several power levels as outlined in Table 1. All heating runs used a circular trajectory (r = 1 mm, 12 points, 100 msec/point). A variable time delay, ranging from 10 to 20 min was applied between ultrasound sonications to allow the heated region to cool to within about 5°Co f the starting temperature. The optimum FAs were derived to be 8° and 42°, respectively. All other scan parameters were equivalent to those used in experiment 1.

Experiment 3

Experiment 3 was performed to assess T_1 changes with temperature over time when tissue damage has already occurred (thermal dose ≥ 240 CEM_{43}). Five larger power values (Table 1) were used to sonicate the chicken breast. All the pulses were applied at the same location. The tissue was heated and cooled using the same timing described in experiment 2. The optimum FAs used were 7° and 34°.

Table 1
Experimental Parameters

	Flip angle 1(°)	Flip angle 2(°)	Acoustic power (watts)	Heating time (min)	Cooling time (min)
Experiment 1					
Run 1	3	20	22	5	6
Run 2	3	20	32	7	8
Experiment 2					
Run 1	8	42	7	3	5
Run 2	8	42	7	3	5
Run 3	8	42	11	3	5
Run 4	8	42	7	3	5
Run 5	8	42	14	3	5
Run 6	8	42	7	3	5
Run 7	8	42	21	3	5
Run 8	8	42	7	3	5
Run 9	8	42	24	3	5
Run 10	8	42	7	3	5
Experiment 3					
Run 1	7	34	27	3	5
Run 2	7	34	39	3	5
Run 3	7	34	39	3	5
Run 4	7	34	39	3	5
Run 5	7	34	39	3	5

The measurements were acquired with the following scan parameters for all heating runs: repetition time TR = 40 ms, echo time TE = 7 ms, bandwidth = 752 Hz/pixel, image matrix = 128 × 64, 12 slices, and 2 mm isotropic resolution.

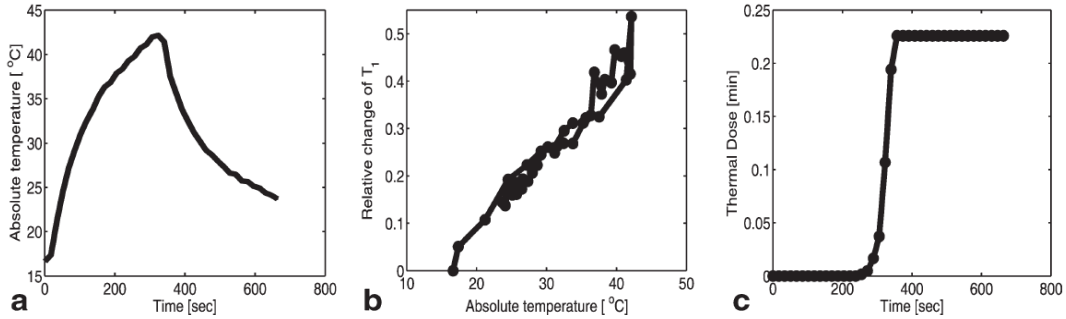

FIG. 3. Sonication results of chicken breast for experiment 1 run 1 (22 watts). **a**: Plot of the average absolute temperature versus time of 4 voxels centered at the focus. **b**: Plot of the relative change of T_1 versus the absolute temperature of the 4 voxels centered at the focus. The precision of the relative change of T_1 is 0.009. **c**: Plot of the mean thermal dose versus time of the 4 voxels centered at the focus.

Thermal Dose Calculation

To obtain an estimate of tissue thermal damage for comparison with the T_1 measurements, corresponding maps of the accumulated thermal dose, as defined by Sapareto and Dewey (14), were generated for each time point of each sonication based on the fiber optic probe and PRF temperature measurements.

$$t_{43} = \sum_{t=0}^{t=\text{final}} R^{(43-T)}\Delta t \qquad [3]$$

Where t_{43} is the thermal dose in CEM_{43}, T is the average absolute temperature during time Δt, and $t_{\text{final}} = t_{\text{heating}} + t_{\text{cooling}}$ is the final dose measurement time. T was determined by adding the fiber optic probe reading at the time of sonication to the PRF temperature change measurement. R is the isodose constant, which is temperature dependent, and was determined based on experimental data (26). Therefore, $R = 0$ for $T < 39°\text{C}$, $R = 0.25$ for $39 < T < 43°\text{C}$, and $R = 0.5$ for $T > 43°\text{C}$ (27). The dose maps for all the sonications at each location were summed to calculate the accumulated thermal dose. Based on literature values for muscle, 240 CEM43°C was used as a threshold dose for total necrosis (28,29).

Data Processing

For this work, all MR image reconstruction and postprocessing was performed off-line. The optimal SNR multicoil algorithm was used to combine the coils (30). Averaging over the phase maps of the two optimum FAs was used to improve the SNR of the temperature map. To avoid phase wraparound errors that would occur at sufficiently high temperature, a phase difference image $\Delta\Phi_i$ was constructed on a pixel-by-pixel basis from each image complex image, signal intensity $(\text{SI})_i$, acquired during the heating cycle such as:

$$\Delta\Phi_i = \text{phase}(\text{SI}_{i+1}\text{SI}_i^*)[\qquad 4]$$

The total phase change was obtained as the sum of $\Delta\Phi_i$ over time. For continuous heating experiments where images are acquired sequentially, this technique prevents the phase difference from exceeding $\pm 2\pi$. Magnitude images were used as masks to remove background noise in the phase and temperature images. While there exists temperature dependence values for muscle (31) or pure water (17) in the literature, our calibration experiments showed a value of -0.009 ppm/°C in ex vivo chicken breast. Finally, the temperature maps were converted to thermal dose maps using Eq. 3. The values of the spin-lattice relaxation time T_1 were calculated from the magnitude images of the two optimum FAs (Eq. 3). Before obtaining the T_1 maps, the image noise was reduced by applying a Hanning-filter to the raw data before reconstruction. To compensate for tissue variability of T_1, the data were plotted as relative change.

To examine whether dynamic changes in T_1 can be used to indicate irreversible changes in tissues the dependence of T_1 on temperature before tissue damage was determined on a voxel basis using all time points for which the accumulated thermal dose remained negligible. This voxel specific slope was then used dynamically to correct the T_1 measurement for all subsequent time points:

$$T_{1cor} = T_1(T) - \lambda\Delta T \qquad [5]$$

where, $\lambda = \frac{\partial T_1}{\partial T}$ is the voxel-specific dependence of T_1 on temperature.

RESULTS

The simultaneous water proton spin-lattice relaxation time T_1 and the temperature change (PRF) were measured for the chicken breast tissues over a 2×2 voxel ROI centered at the focus. Figure 3a shows the plot of the absolute temperature (fiberoptic temperature + PRF temperature change) versus the time for experiment 1, run 1 at 22 acoustic watts. The recorded temperatures via the fiberoptic temperature probe during the experiment vary from the PRF-derived temperature at an ROI chosen near the tip of the probe by $\pm 1°\text{C}$. Figure 3b and c are the corresponding plots of the relative change of T_1

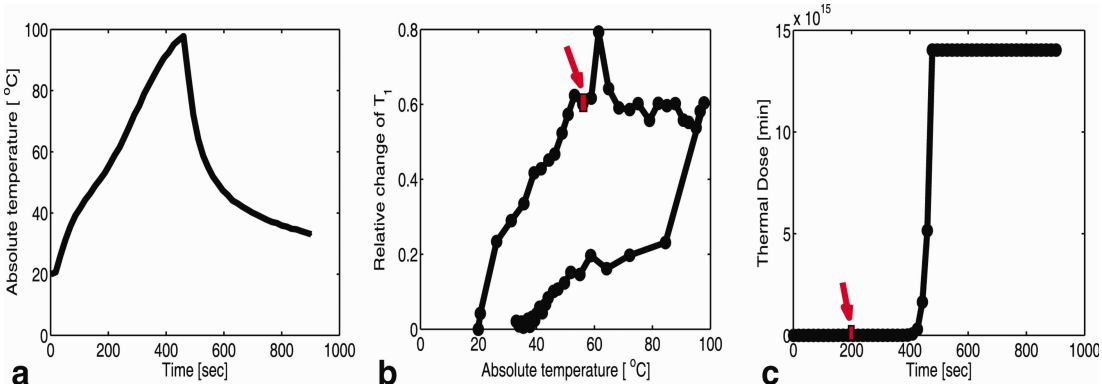

FIG. 4. Sonication results of chicken breast for experiment 1 run 2 (32 watts). **a**: Plot of the absolute temperature versus time of 4 voxels centered at the focus. **b**: Plot of the relative change of T_1 versus the absolute temperature of the 4 voxels centered at the focus. The precision of the relative change of T_1 is 0.014. **c**: Plot of the mean thermal dose versus the time of the 4 voxels centered at the focus. The arrows on parts **b** and **c** indicate the time at which 240 CEM was reached. [Color figure can be viewed in the online issue, which is available at wileyonlinelibrary.com.]

versus the absolute temperature and the cumulative equivalent minute thermal dose versus the time, respectively. To estimate precision, the standard deviation of relative change in T_1 measured in a uniform, nonheated region was found to be 0.009. From Fig. 3b,c, it can be seen that T_1 is reversible with temperature when the maximum cumulative equivalent minute thermal dose at the focus is very low (0 and 0.25 CEM) compared with the threshold value of 240 CEM.

Figure 4a shows the plot of the absolute temperature versus the time for experiment 1 run 2 at 32 acoustic watts. Figure 4b and c show that the relative change of T_1 versus temperature curve deviates from linearity when the thermal dose exceeds 240 CEM_{43}, and that T_1 is no longer reversible. The precision of the relative change in T_1 is 0.0014. The rectangle in Fig. 4b and c indicate the time point at which 240 CEM_{43} was reached.

The deviation of the T_1 versus temperature curve from linearity is observed in voxels in all five central slices from the 3D volume where significant thermal dose was accumulated (Fig. 5c). In this plot, the T_1 measurements in every voxel in a 21 × 21 voxel ROI (see the absolute temperature and the absolute T_1 maps shown in Fig. 5a,b for the five central slices covering the focal zone at all time points are corrected for the instantaneous temperature and then the T_{1cor} values are averaged based on accumulated dose. The thermal dose was subdivided in 10 different ranges of dose: [0–50], [50–100], [100–200], [200–240], [240–500], [500–1000], [1000–2000], [2000–3000], [3000–5000], and [5000–(higher dose)]. The mean corrected T_1 change for the range of thermal dose 5000 and higher is plotted at the location 6000 along the dose axis for better visualization. The error bars represent the standard error of the corrected T_1 change values in each dose range.

Figures 6a and b show the absolute temperature and the absolute T_1 maps of the focal zone for experiment 2 run 9. The black rectangle represents the ROI used to plot Fig. 6c and d. Figure 6c and d present the results of experiment 2 and plots the absolute T_1 versus the absolute temperature and the corresponding thermal dose versus the time for a series of 10 HIFU heating and cooling runs ranging from 7 to 24 acoustic watts. Figure 6c and d show that the relative T_1 is reversible with temperature before tissue damage occurs. Figure 7a and b present the absolute temperature and the absolute T_1 maps of experiment 3 run 1. Figure 7b and c show the results of experiment 3 and plot the absolute T_1 versus the absolute temperature and the corresponding thermal dose versus the time for five HIFU heating and cooling runs ranging from 27 to 39 acoustic watts. Figure 7c and d demonstrate that the irreversibility in T_1 is observed when the accumulated thermal dose exceeds the tissue damage threshold value of 240 CEM_{43}. The T_1 values calculated using the IR method as shown in Fig. 8a,b were obtained before any heating and after the last heating run in experiment 3. The irreversible tissue changes were visually detectable (Fig. 8i). Comparisons of the T_1 changes with thermal dose are also shown in Fig. 8e–h. The color of the chicken breast tissue changed from light pink to white, and free fluid was visible.

DISCUSSIONS AND CONCLUSION

The results we have obtained in ex vivo chicken breast tissue using the hybrid PRF- T_1 technique are consistent with the suggestion that the spin lattice relaxation time T_1 changes reversibly with temperature for low thermal dose accumulation and irreversibly with temperature after significant accumulation of thermal dose. According to the hyperthermia literature (16,32,33), the dose threshold of 240 CEM_{43} is adequate to coagulate all tissue and thus has been used as an indicator of tissue damage caused by focused ultrasound. Figure 6c and d shows that repeated MRgHIFU sonications at the same location with minimal thermal dose accumulation (<50 CEM_{43}) results in reversible changes in T_1. The results in Fig. 4b and c are consistent with the hypothesis that irreversible change in T_1 occurs at about 240 CEM_{43}. This conclusion is further confirmed by the results shown in Figs. 5d and 7c,d.

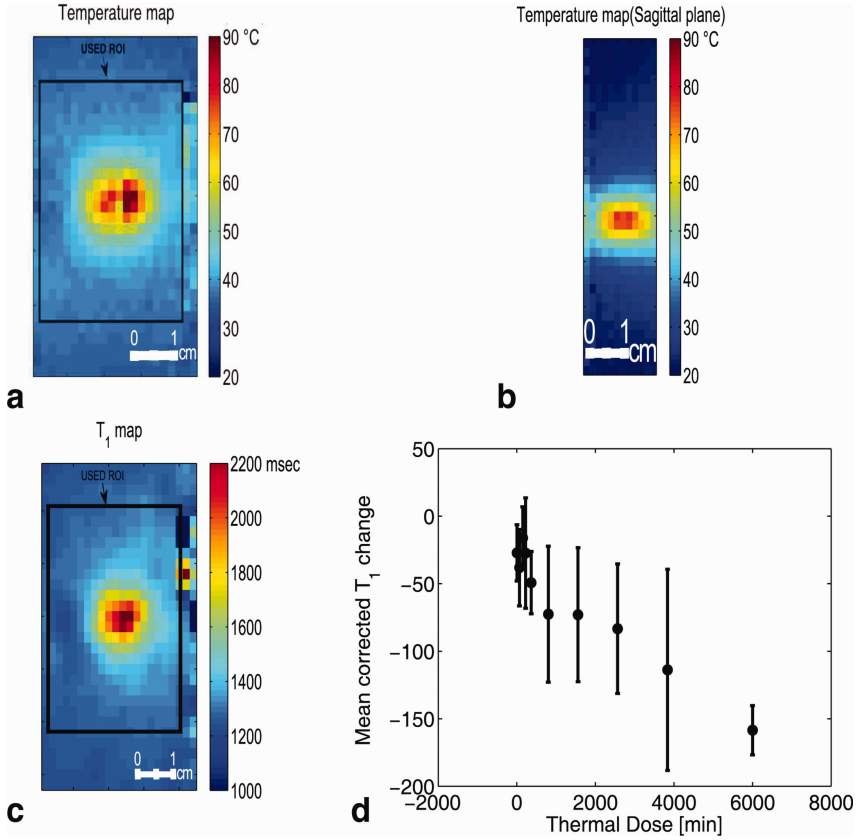

FIG. 5. Coronal (**a**) and sagittal (**b**) planes through the 3D PRF temperature map around the focal spot at the peak temperature in experiment 1 run 2 (32 watts). **c**: Corresponding T_1 map of the focal zone at the peak temperature for experiment 1 run 2 (32 watts). **d:** Plot of the dose-interval-averaged change of T_{1cor} versus the thermal dose. T_1cor values were calculated in the volume defined by the black rectangle in (c) (21 × 21 voxels) over the 5 central slices. For averaging, the thermal dose was subdivided in ten different ranges of dose: [0–50], [50–100], [100–200], [200–240], [240–500], [500–1000], [1000–2000], [2000–3000], [3000–5000], and (5000–[higher dose]). The mean value of T_{1cor} change for the range of thermal dose 5000 and higher is located at the point 6000 CEM on the dose axis for better visualization of all voxels used. The error bars represent the standard error of the mean value of the T_{1cor} change values averaged in each dose range. [Color figure can be viewed in the online issue, which is available at wileyonlinelibrary.com.]

Temperature measurements and indications of tissue changes are both important for the monitoring and quality control of thermal therapy treatments. Therefore, the hybrid PRF-T_1 method has the advantages of simultaneously producing two types of valuable information about the tissue during thermal therapy: a change in T_1 that depends on temperature and cell/tissue structure and a change in the PRF that depends only on temperature. The presented results indicate that monitoring the T_1 change along with temperature is a potential complementary indicator for assessing tissue damage due to hyperthermia.

One of the prerequisites for successful T_1 monitoring of thermal therapy is stability over the entire treatment period. The data presented in this article, such as that shown in Fig. 6c demonstrates the stability of T_1 determination for a treatment time of approximately 3 h during the application of several individual sonications. T_1 has the advantage of being less dependent on fluctuations of the magnetic field than the chemical shift at high field, and is highly dependent on temperature, providing improved measurement stability when compared with PRF temperature measurements. Therefore, while the hybrid PRF-T_1 technique requires several calibration steps, the obtained calibration does remain valid over a clinically feasible MRgHIFU treatment duration.

It may be feasible to improve the practicality of applying the hybrid PRF-T_1 technique by reducing the calibrations steps and the acquisition times. The temporal footprint of each image can be reduced by subsampling and using parallel image reconstruction (e.g., generalized autocalibrating partially parallel acquisitions (GRAPPA)) to reduce the acquisition time by 2 or more with minimal loss in accuracy of the temperature and T_1 maps. The reduction of acquisition time would allow a better evaluation of T_1 evolution during the treatment, and thus the assessment of thermal dose effects. The calibration steps described earlier in this article are necessary for an accurate T_1 calculation. Therefore, it should be noted that the accuracy of the variable FA technique is essentially dependent on using the actual local FAs. B_1 inhomogeneity causes a spatial variation in the FA

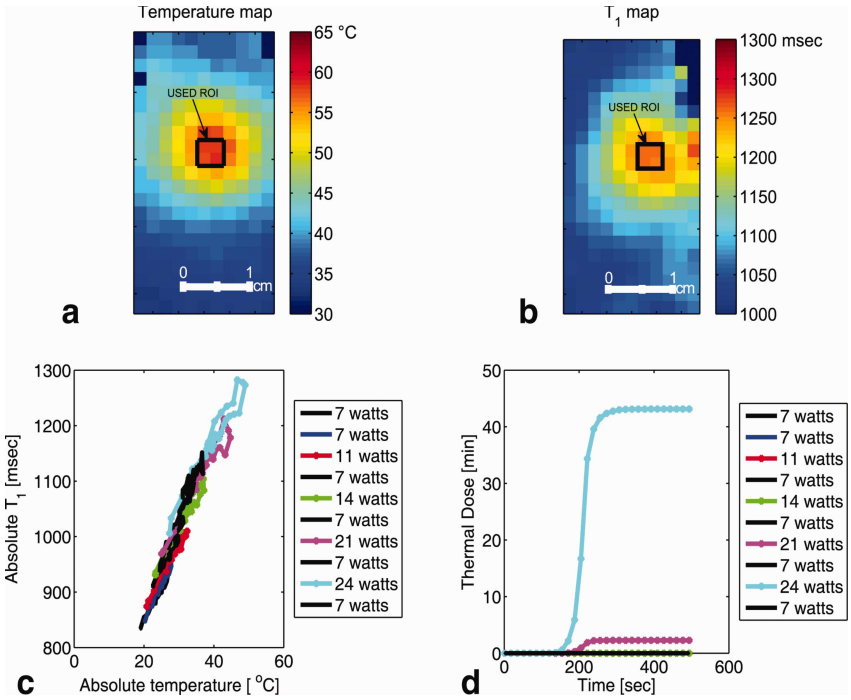

FIG. 6. Plot of absolute T_1 with low accumulated thermal dose. **a,b**: Temperature and T_1 maps of the focal zone for experiment 2 run 9. The black rectangle represents the ROI used to plot figure **c** and **d. c**: Plot of average T_1 versus the average absolute temperature of 4 voxels centered at the focus. A series of ten heating and cooling runs were performed at the acoustic powers: 7 watts, 7 watts, 11 watts, 7 watts, 14 watts, 7 watts, 21 watts, 7 watts, 24 watts, and 7 watts. **d**: Plot of the corresponding thermal dose versus time averaged over the same 4 voxels centered at the focus. [Color figure can be viewed in the online issue, which is available at wileyonlinelibrary.com.]

and therefore, needs to be corrected (34). Several other B_1 mapping techniques exist that are capable of producing accurate B_1 maps (35). We have chosen the double FA method because of its simplicity and accuracy. Although B_1 mapping over the entire volume can require several minutes of acquisition and processing, it has to be performed only once and then can be used throughout the procedure.

There are several limitations to the results in this study: The dose calculations assume that our PRF

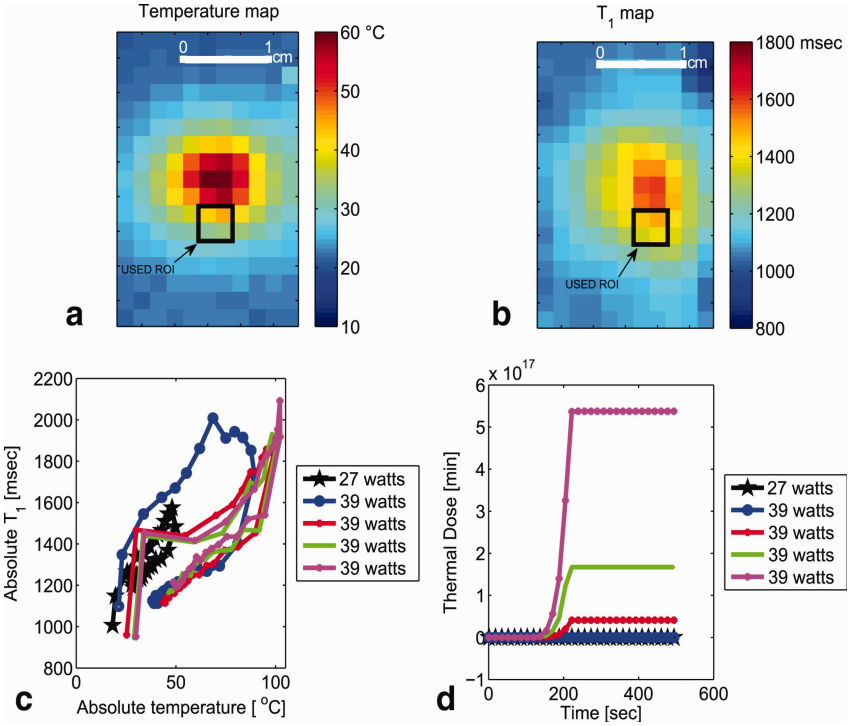

FIG. 7. Plot of absolute T_1 after high thermal dose. **a,b**: Temperature and T_1 maps of the focal zone for experiment 3 run 1. The black rectangle represents the ROI used to plot figure c and d. The ROI was chosen in region where no voxel were heated to boiling temperature. **c**: Plot of T_1 versus the absolute temperature of 4 voxels at the focus. A series of five heating and cooling runs were performed at the acoustic powers: 27 watts, 39 watts, 39 watts, 39 watts, 39 watts. **d**: Plot of the corresponding thermal dose versus time of the 4 voxels centered at the focus. [Color figure can be viewed in the online issue, which is available at wileyonlinelibrary.com.]

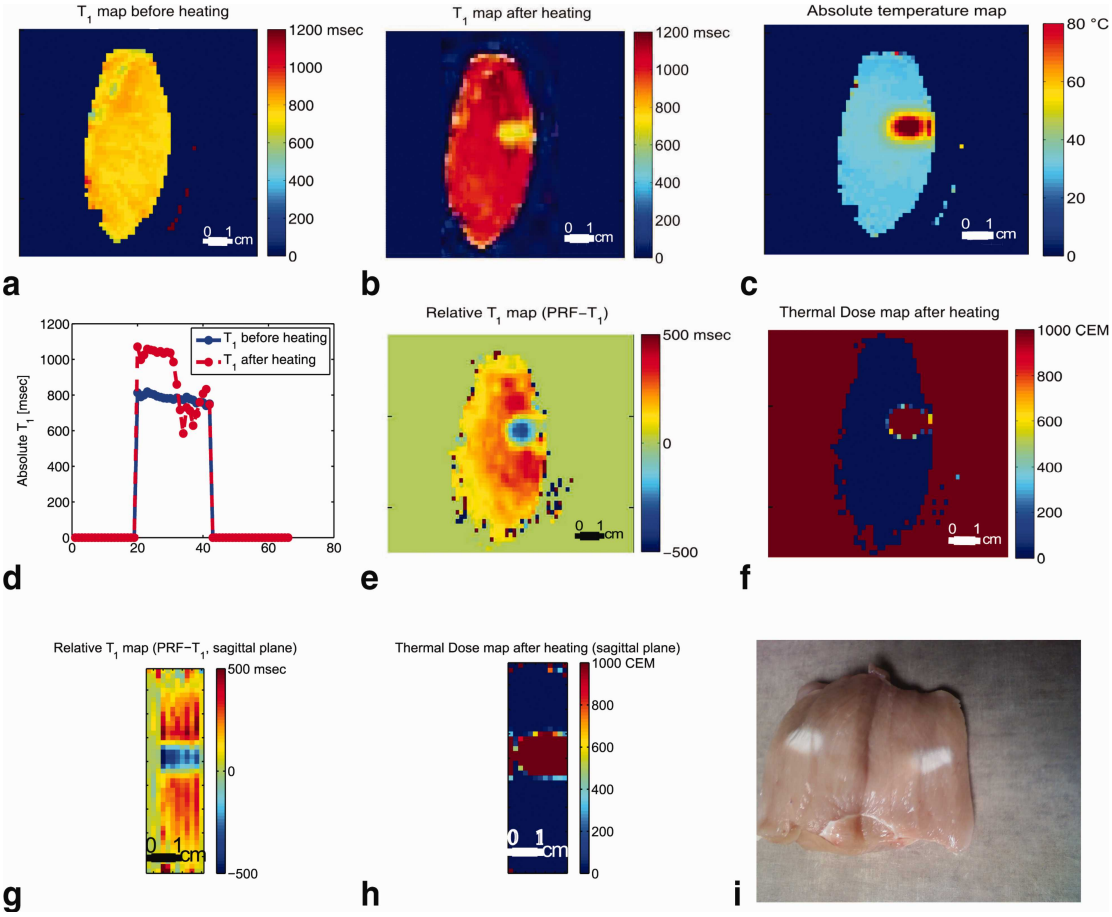

FIG. 8. Distribution of absolute and relative T_1 obtained using IR and PRF- T_1 T_1 in a coronal slice of the chicken breast. **a**:I R T_1 map before the HIFU heating. **b**:I R T_1 map of the same coronal slice after the five heating runs in experiment 3 were performed. **c**: Absolute temperature map of the slice at peak temperature during heating in experiment 3, run 5. **d**: Cross section taken centrally through IR T_1 maps before (blue line) and after heating (red dashed line) in experiment 3. The local drop in T_1 corresponds to the region of heating. **e**: T_1 change map derived from the PRF- T_1 method after the five heating runs in experiment 3. The T_1 changes map was obtained by subtracting the first time frame of run 1 from the last time frame of run 5. **f**: Corresponding thermal dose map of the same coronal slice. The local drop in T_1 corresponds to the region of heating as shown by the thermal dose map. Sagittal (**g,h**) through the 3D relative T_1 and thermal dose maps derived from the PRF- T_1 method. **i**: Picture of the chicken breast after the 5 runs of experiment 3. The color of the chicken breast tissue changed from light pink to white. The color change was the visual indicator that tissue damage has occurred. [Color figure can be viewed in the online issue, which is available at wileyonlinelibrary.com.]

temperature measurements are accurate. Small errors in the temperature measurement can lead to large errors in thermal dose calculation. While the measured PRF temperature localized around the fiberoptic probe were accurate to within $+/-1$°C that does not necessarily translate to accuracy across the entire region of interest. The dose calculations also assume that accumulated dose is additive over the relatively long time-course of each experiment. Furthermore, although the double angle method should be reasonably accurate, there were larger variations in T_1 than expected and are likely due to uncompensated variations in the B_1 across the sample. Although the dependence of tissue T_1 on the dynamic structure and amount of water in the tissue should make it a valuable index for reflecting the state of tissue, a major concern is whether water migration due to sublethal heating of tissue may cause a confounding change in T_1. Finally, we note that jumps in the T_1 values were observed in all experiments, as can be seen in Figs. 3b, 4b, and 7c. These jumps only occur in voxels in the ultrasound focus and correspond to a measured increase in T_1 when ultrasound is turned on and a decrease when it is turned off. These jumps are very consistent and are a subject of an ongoing investigation that will be reported subsequently.

In summary, this work has introduced and tested the 3D hybrid PRF-T_1 technique as a new method of evaluating the thermal exposure induced by focused ultrasound sonications. We have demonstrated in ex vivo tissue samples that the temperature-corrected T_1 values obtained using the hybrid PRF- T_1 method gives potentially very useful information about tissue damage that correlates with our estimates of accumulated thermal dose. However, further investigation is needed to more

completely assess the link between the T_1 temperature dependence and tissue damage. First, the reversibility of T_1 with temperature at low thermal dose and the transition to irreversibility at high dose needs to be validated in vivo. These experiments should test for the existence of a threshold at which such a transition occurs. Because tissue T_1 is influenced by a delicate balance of the water content, the macroscopic and microscopic distribution of water in different sites, and the macromolecular-water interactions (36), it is important to determine the effects of heating on T_1 in vivo. Although the T_1 dependence in vivo may be confounded by changes in water content or other tissue properties, a detectable change in the functional relationships between T_1 and temperature might be an indicator of the point at which damage occurs. Determining this functional relationship for a variety of tissues might be used during treatments to improve the success of the thermal therapy. For example, the T_1 temperature dependence may provide online information to the physician so that the desired target volume is exposed adequately. Furthermore, use of thermal imaging and the T_1 change threshold calculation might increase safety by providing warning before the surrounding normal tissue is overexposed. As the hybrid PRF-T_1 technique can produce simultaneously T_1 and PRF temperature maps and therefore the thermal dose map, it appears to be well suited for tissue damage assessment.

ACKNOWLEDGMENTS

The authors appreciate helpful contributions from Joshua de Bever, Dr. Robert B. Roemer, and other collaborators at the University of Utah.

REFERENCES

1. Hill CR, Bamber JC, ter Haar GR. Physical principles of medical untrasonics, 2nd Ed. Chichester, U. K.: Wiley; 2004.
2. Kremkau FW. Cancer therapy with ultrasound: a historical review. J Clin Ultrasound 1979;7:287–300.
3. Dickinson RJ, Hall AS, Hind AJ, Young IR. Measurement of changes in tissue temperature using MR imaging. J Comput Assist Tomogr 1986;10:468–472.
4. Ishihara Y, Calderon A, Watanabe H, Okamoto K, Suzuki Y, Kuroda K, Suzuki Y. A precise and fast temperature mapping using water proton chemical shift. Magn Reson Med 1995;34:814–823.
5. Parker DL, Smith V, Sheldon P, Crooks LE, Fussell L. Temperature distribution measurements in two-dimensional NMR imaging. Med Phys 1983;10:321–325.
6. Hynynen K, Vykhodtseva NI, Chung AH, Sorrentino V, Colucci V, Jolesz FA. Thermal effects of focused ultrasound on the brain: determination with MR imaging. Radiology 1997;204:247–253.
7. McDannold NJ, King RL, Jolesz FA, Hynynen KH. Usefulness of MR imaging-derived thermometry and dosimetry in determining the threshold for tissue damage induced by thermal surgery in rabbits. Radiology 2000;216:517–523.
8. Anzai Y, Lufkin RB, Castro DJ, Farahani K, Jabour BA, Layfield LJ, Udkoff R, Hanafee WN. MR imaging-guided interstitial Nd:YAG laser phototherapy: dosimetry study of acute tissue damage in an in vivo model. J Magn Reson Imaging 1991;1:553–559.
9. Carstensen EL, Becroft SA, Law WK, Barbee DB. Finite amplitude effects on the thresholds for lesion production in tissues by unfocussed ultrasound. J Acoust Soc Am 1981;70:302–309.
10. Dunn F, Fry FJ. Ultrasonic threshold dosages for the mammalian central nervous system. IEEE Trans Biomed Eng 1971;18:253–256.
11. Dunn F, Lohnes JE, Fry FJ. Frequency dependence of threshold ultrasonic dosages for irreversible structural changes in mammalian brain. J Acoust Soc Am 1975;58:512–514.
12. Fry FJ, Kossoff G, Eggleton RC, Dunn F. Threshold ultrasonic dosages for structural changes in the mammalian brain. J Acoust Soc Am 1970;48(suppl 2):1413.
13. Robinson TC, Lele PP. An analysis of lesion development in the brain and in plastics by high-intensity focused ultrasound at low-megahertz frequencies. J Acoust Soc Am 1972;51:1333–1351.
14. Sapareto SA, Dewey WC. Thermal dose determination in cancer therapy. Int J Radiat Oncol Biol Phys 1984;10:787–800.
15. Cheng KH, Hernandez M. Magnetic resonance diffusion imaging detects structural damage in biological tissues upon hyperthermia. Cancer Res 1992;52:6066–6073.
16. Damianou C, Hynynen K. The effect of various physical parameters on the size and shape of necrosed tissue volume during ultrasound surgery. J Acoust Soc Am 1994;95:1641–1649.
17. Hindman JC. Proton resonance shift of water in the gas and liquid states. J Chem Phys 1966;44:4582–4592.
18. Kuroda K, Abe K, Tsutsumi S, Ishihara Y, Suzuki Y, Sato K. Water proton magnetic resonance spectroscopic imaging. Advanced techniques and clinical applications in biomedical thermology. Chur, Switzerland: Harwood Academic Publishers; 1993.
19. Deoni SC, Rutt BK, Peters TM. Rapid combined T_1 and T_2 mapping using gradient recalled acquisition in the steady state. Magn Reson Med 2003;49:515–526.
20. Morrell GR, Schabel MC. An analysis of the accuracy of magnetic resonance flip angle measurement methods. Phys Med Biol 2010;55:6157–6174.
21. Schabel MC, Morrell GR. Uncertainty in T(1) mapping using the variable flip angle method with two flip angles. Phys Med Biol 2009;54:N1–N8.
22. Quesson B, de Zwart JA, Moonen CT. Magnetic resonance temperature imaging for guidance of thermotherapy. J Magn Reson Imaging 2000;12:525–533.
23. Kamman RL, Go KG, Brouwer W, Berendsen HJ. Nuclear magnetic resonance relaxation in experimental brain edema: effects of water concentration, protein concentration, and temperature. Magn Reson Med 1988;6:265–274.
24. Parker DL. Applications of NMR imaging in hyperthermia: an evaluation of the potential for localized tissue heating and noninvasive temperature monitoring. IEEE Trans Biomed Eng 1984;31:161–167.
25. Chung AH, Hynynen K, Colucci V, Oshio K, Cline HE, Jolesz FA. Optimization of spoiled gradient-echo phase imaging for in vivo localization of a focused ultrasound beam. Magn Reson Med 1996;36:745–752.
26. Meshorer A, Prionas SD, Fajardo LF, Meyer JL, Hahn GM, Martinez AA. The effects of hyperthermia on normal mesenchymal tissues. Application of a histologic grading system. Arch Pathol Lab Med 1983;107:328–334.
27. Arora D, Skliar M, Roemer RB. Minimum-time thermal dose control of thermal therapies. IEEE Trans Biomed Eng 2005;52:191–200.
28. Damianou C, Hynynen K, Fan X. Evaluation of accuracy of a theoretical mode for predicting the necrosed tissue volume during focused ultrasound surgery. IEEE Trans Ultrason Ferroelectrics Freq Control 1995;42:182–187.
29. Dewey WC. Arrhenius relationships from the molecule and cell to the clinic. Int J Hyperthermia 1994;10:457–483.
30. Bernstein MA, Grgic M, Brosnan TJ, Pelc NJ. Reconstructions of phase contrast, phased array multicoil data. Magn Reson Med 1994;32:330–334.
31. MacFall JR, Prescott DM, Charles HC, Samulski TV. 1H MRI phase thermometry in vivo in canine brain, muscle, and tumor tissue. Med Phys 1996;23:1775–1782.
32. Chung AH, Jolesz FA, Hynynen K. Thermal dosimetry of a focused ultrasound beam in vivo by magnetic resonance imaging. Med Phys 1999;26:2017–2026.
33. McDannold, Hynynen K, Wolf D, Wolf G, Jolesz F. MRI evaluation of thermal ablation of tumors with focused ultrasound. J Magn Reson Imaging 1998;8:91–100.
34. Cunningham CH, Pauly JM, Nayak KS. Saturated double-angle method for rapid B_1+ mapping. Magn Reson Med 2006;55:1326–1333.
35. Morrell GR. A phase-sensitive method of flip angle mapping. Magn Reson Med 2008;60:889–894.
36. Mathur-De Vre R. Biomedical implications of the relaxation behaviour of water related to NMR imaging. Br J Radiol 1984;57:955–976.

CHAPTER VI

TOWARD REAL-TIME TEMPERATURE MONITORING IN FAT AND AQUEOUS TISSUE DURING MAGNETIC RESONANCE-GUIDED HIGH-INTENSITY FOCUSED ULTRASOUND USING THREE-DIMENSIONAL PROTON RESONANCE FREQUENCY T_1 METHOD

*This chapter is based on the paper titled "*Toward Real-Time Temperature Monitoring in Fat and Aqueous Tissue During Magnetic Resonance-Guided High-Intensity Focused Ultrasound Using Three-Dimensional Proton Resonance Frequency T_1 Method*" authored by Mahamadou Diakite, Henrik Odéen, Nick Todd, Allison Payne, and Dennis L. Parker. The paper has been accepted for publication at the journal of Magnetic Resonance in Medicine (MRM) (Reprinted with permission).*

FULL PAPER

Magnetic Resonance in Medicine 00:00–00 (2013)

Toward Real-Time Temperature Monitoring in Fat and Aqueous Tissue During Magnetic Resonance–Guided High-Intensity Focused Ultrasound Using a Three-Dimensional Proton Resonance Frequency T_1 Method

Mahamadou Diakite,[1,2]* Henrik Odéen,[1,2] Nick Todd,[2] Allison Payne,[2] and Dennis L. Parker[2]

Purpose: To present a three-dimensional (3D) segmented echoplanar imaging (EPI) pulse sequence implementation that provides simultaneously the proton resonance frequency shift temperature of aqueous tissue and the longitudinal relaxation time (T_1) of fat during thermal ablation.
Methods: The hybrid sequence was implemented by combining a 3D segmented flyback EPI sequence, the extended two-point Dixon fat and water separation, and the double flip angle T_1 mapping techniques. High-intensity focused ultrasound (HIFU) heating experiments were performed at three different acoustic powers on excised human breast fat embedded in ex vivo porcine muscle. Furthermore, T_1 calibrations with temperature in four different excised breast fat samples were performed, yielding an estimate of the average and variation of dT_1/dT across subjects.
Results: The water only images were used to mask the complex original data before computing the proton resonance frequency shift. T_1 values were calculated from the fat-only images. The relative temperature coefficients were found in five fat tissue samples from different patients and ranged from 1.2% to 2.6%/°C.
Conclusion: The results demonstrate the capability of real-time simultaneous temperature mapping in aqueous tissue and T_1 mapping in fat during HIFU ablation, providing a potential tool for treatment monitoring in organs with large fat content, such as the breast. **Magn Reson Med 000:000–000, 2013. © 2013 Wiley Periodicals, Inc.**

Key words: temperature; aqueous tissue; fat

INTRODUCTION

MR-guided high-intensity focused ultrasound (HIFU) is a noninvasive technique for thermal ablation of solid tumors with real-time image guidance. For thermal therapy to be successful, it is essential that sufficient heat to cause ablation is delivered to the tumor while the heating of healthy surrounding tissue is minimized. Therefore, accurate temperature mapping in the tumor and surrounding tissue throughout a thermal therapy procedure is essential to ensure the safety and efficacy of the treatment.

MRI temperature measurement methods based on the temperature dependency of the water proton resonance frequency (PRF) shift have shown the best ability to quantify temperature rises in aqueous tissues (1,2). Furthermore, the temperature dependency of PRF shows little dependence on the tissue changes that occur when the tissue is rapidly heated, such as with HIFU.

Unfortunately, the PRF shift with temperature does not apply to lipid protons, since there is no hydrogen bonding among the methylene protons that supply the bulk of the fat signal (3). For tissues with large fat content, such as breast tissue (4), a thermometry technique for fat and aqueous tissues is desired. This can be technically challenging, particularly due to the complex chemical structure of the fat molecule. In vivo MR spectroscopy indicates that human breast fat is composed of a number of different fatty acids (5) that yield different chemical shifts. The dominant components in fat are methylene (CH_2) and methyl radicals (CH_3).

The relaxation times (T_1 and T_2) of tissues, which are sensitive to the dynamic structure and amount of water in the biological system, are also sensitive to temperature. The temperature sensitivity of the spin-lattice relaxation time, T_1, has been measured for a number of fatty tissues, and has been found to obey a nearly linear relationship with temperature (6,7). T_1 of CH_2, the dominant component of fat, was shown to be promising in terms of reliability and reproducibility for measuring temperature changes (8).

In this study, we present an MRI sequence for simultaneous three-dimensional (3D) fat and water temperature imaging based on the extended two-point Dixon fat and water separation and the double flip angle (DFA) T_1 mapping techniques. The technique was implemented using a 3D segmented flyback echoplanar imaging (EPI) sequence for real-time temperature monitoring during

[1]Department of Physics & Astronomy, University of Utah, Salt Lake City, Utah, USA.
[2]Department of Radiology, University of Utah, Salt Lake City, Utah, USA.
Grant sponsor: National Institutes of Health; Grant number: R01 CA134599; Grant sponsor: The Ben B. and Iris M. Margolis Foundation; Grant sponsor: Siemens Medical Solutions.
*Correspondence to: Mahamadou Diakite, Utah Clean Air Partnership, Department of Radiology, University of Utah, 729 Arapeen Drive, Salt Lake City, UT 84108. E-mail: bijoumd@hotmail.com
Received 15 November 2012; revised 1 July 2013; accepted 1 July 2013
DOI 10.1002/mrm.24900
Published online 00 Month 2013 in Wiley Online Library (wileyonlinelibrary.com).

HIFU sonication of a phantom consisting of human breast fat embedded in ex vivo porcine muscle. The mixture of these tissues was used as a substitute for the human breast.

METHODS

Extended Two-Point Dixon

The extended two-point Dixon method, which provides fat and water separation comparable to the three-point Dixon method (9), was applied for two flip angles (α_1 and α_2) as follows:

$$I_1 = (W_{a1} + F_{a1})\, e^{(i\phi_0)} \quad [1]$$

$$I_2 = (W_{a2} + F_{a2})\, e^{(i\phi_0)} \quad [2]$$

$$I_3 = (W_{a1} + F_{a1})\, e^{(i[\phi_0+\phi_1])} \quad [3]$$

$$I_4 = (W_{a2} + F_{a2})\, e^{(i[\phi_0+\phi_1])} \quad [4]$$

where I_1 and I_2 represent the two in-phase images acquired at echo time (TE) and I_3 and I_4 are the two out-of-phase images acquired at TE+Δ. W and F are real, nonnegative, and proportional to the amount of water and fat magnetization in each voxel, respectively. The flip angles α_1 and α_2 were computed to minimize the variance in fat T_1 as described previously (10). ϕ_1 is the phase accumulation induced by B_0 field inhomogeneity during the time Δ. ϕ_0 is the phase that accumulates from all sources during time TE.

Equations [1] and [3] can be solved for W and F by first eliminating ϕ_0 using:

$$S_{a1} = W_{a1} + F_{a1} = |\, I_1| \text{ and } S'_{a1} = I_3 * e^{(-i\phi_0)} = (W_{a1} - F_{a1})\, e(i\phi_1)$$

The phase of the image $\left(S'^2_{a1}\right)$ was unwrapped (11) before extracting the phase as: $\phi_1 = \frac{1}{2} arg\left(S'^2_{a1}\right)$. The final water and fat images were obtained as:

$$W = \frac{1}{2}\left(S_{a1} + S'_{a1} e^{(-i\phi_1)}\right) \text{ and } F = \frac{1}{2}\left(S_{a_1} + S'_{a_1} e^{(-i\phi_1)}\right)$$

where W and F are the resulting water and fat-only images at flip angle α_1. Similarly, I_2 and I_4 were used to obtain fat and water images at flip angle α_2.

PRF Temperature Measurement

The PRF shift uses the temperature-dependent change of the proton chemical shift relative to a baseline value (nonheated). The phase difference is converted to temperature change as (12–14):

$$\Delta T = \frac{\Delta\phi}{\gamma * \beta * B_0 * TE} \quad [5]$$

where γ is the gyromagnetic ratio, β is the thermal coefficient, B_0 is the main magnetic field, and $\Delta\phi$ is the phase change. Phase subtraction was performed to exclude nonthermal contributions to the phase (e.g., radiofrequency [RF] coil sensitivity or B_0 field inhomogeneities), leaving only the spatially resolved phase shift attributable to temperature-induced PRF shift. PRF temperature changes were estimated in aqueous tissue by using the water-only images, derived from the Dixon water/fat separation, as a mask on the original complex data.

Furthermore, in the regions where fat and water voxels overlapped due to the chemical shift (usually at the fat/water interface regions), the water phase was calculated in a straightforward manner based on the fraction of the fat and water in each voxel, the fat background phase, and the resulting signal intensity in those voxels before the fat/water separation. From a schematic representation of fat ($\vec{F}$) and water ($\vec{W}$) magnetization vectors as well as the resultant signal vector ($\vec{SI}$) in a single overlapped fat/water voxel, one can obtain the scalar form as:

$$\begin{cases} wcos(\phi_w) + fcos\left(\phi_f\right) = SIcos(\phi) \\ wsin(\phi_w) + fsin\left(\phi_f\right) = SIsin(\phi) \end{cases} \quad [6]$$

where (w, ϕ_w) and (f, ϕ_f) are the magnitudes and phases of the vectors $\vec{F}$ and $\vec{W}$, respectively. Similarly, SI and ϕ are the magnitude and phase of the resultant signal. The fat background phase, ϕ_f, for a mixed fat/water voxel is set equal to the phase of the nearest fat-only voxel.

From Equation [6], one can solve for the water phase as:

$$\phi_w = tan^{-1}\left(\frac{\sin(\phi) - \Im.\sin\left(\phi_f\right)}{cos(\phi) - \Im.\cos\left(\phi_f\right)}\right) \quad [7]$$

where $\Im = \frac{f}{SI}$ is the fat fraction in the mixed fat/water voxel.

Because the fat phase changes very little with a rise in temperature, it can be assumed that ϕ_f remains constant and ϕ_w can be extracted for measuring the PRF temperature throughout the treatment. However, it is important to note that if a small change in fat phase were to occur, this would be a source of error in the computation of the water phase in mixed fat/water voxels.

Furthermore, it has been shown that the susceptibility change in fat is a source of error in the PRF temperatures in mixed fat/water tissue (15). These errors are not eliminated by fat suppression, and they originate from several factors, which range from the shape and orientation of the heating pattern to the water and fat distribution inside the heated area. In general, they are small and difficult to quantify and should be evaluated on an experiment-by-experiment basis for tissues with large fat content.

T_1 Temperature Measurement Using the DFA Method

The DFA method uses the equation describing the T_1 dependence of the signal of an ideally spoiled steady state gradient echo sequence. We calculated a single longitudinal relaxation time assuming that fat can be represented by its dominant methylene peak.

Two measurements made at different flip angles are used to linearize the signal equation and therefore T_1 can be extracted by linear regression as described in Deoni et al. (10). The two flip angles must be chosen carefully to optimize the precision of the measurement.

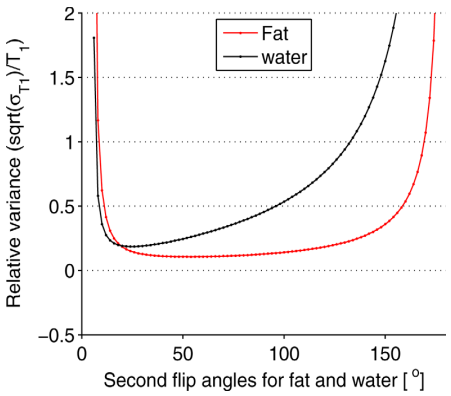

FIG. 1. Simulation result of the relative variance of T_1 when the two optimal flip angles of water are used to estimate T_1 in mixed fat/water tissue. For the simulation, the first flip angle for fat was set equal to the first optimum flip angle of water $(a_{1water} = a_{1fat} = 5^\circ$ and the second flip angles for fat a_{2fat} and water a_{2water} were found by varying the flip angles from 6° to 180° in 2° increments. The plot shows that T_1 can be computed simultaneously in fat and water with minimal loss in T_1 precision in fat by just using the two optimal flip angles of water.

Deoni et al (16) and Schabel and Morrell (17) have each shown that the precision is best when the flip angles chosen are on either side of the Ernst angle and the signal for each is 71% of the signal intensity produced at the Ernst angle. Measurement accuracy is compromised when the flip angles used in the calculations do not equal the actual flip angles applied. Because B_1 is not homogeneous, a B_1 field map for accurate flip angle determination needs to be obtained prior to the measurement. In gradient echo sequences, the B_1 field map at a given flip angle, α, can be obtained by dividing two acquisitions performed with flip angles α and 2α (18). This approach of the B_1 field mapping is T_1-dependent and requires that the repetition time (TR) during the acquisition at the two flip angles is long (e.g. 5 times T_1) compared with T_1 of the sample. Because the goal of these experiments was to determine T_1 in fat, the TR used for B_1 determination was five times the T_1 of fat. B_1 is then determined from the local flip angle:

$$a = cos^{-1}\left(\frac{SI_{2a}}{2 * SI_a}\right) \quad [8]$$

Furthermore, T_1 can be simultaneously calculated in fat and water with minimum loss of T_1 precision in fat. In this case, our simulations (Fig. 1) show that a good precision in T_1 in both fat and water can be achieved by solely considering the optimum two flip angles of water and setting the TR to equal five times T_1 of the water for B_1 field mapping. The simulation was performed using the parameters TR = 20 ms, $T_{1,fat}$ = 300 ms, and $T_{1,water}$ = 1200 ms, which yielded two sets of optimal flip angles (9°,4 8°) and (5°,2 5°) for fat and water, respectively. The plot of the relative variance of T_1 versus the second flip angles of fat and water in Figure 1 was obtained by setting the first flip angle of fat equal to the first optimal flip angle of water $(a_{1fat} = a_{1water} = 5^\circ$, and changing the second flip angle from 6° to 180° in 2° increments for fat and water, respectively.

The dependence of T_1 with temperature has been demonstrated experimentally (19,20) and can be approximated as:

$$T_1(T) = T_1(T_{ref}) + \lambda(T) - T_{ref} \quad [9]$$

where $\lambda = \frac{dT_1}{dT}$ is tissue-dependent, T is the absolute temperature during heating, and T_{ref} is the absolute temperature of the reference time point where no heating has occurred.

Experimental Setup and Pulse Sequences Design

We conducted experiments on excised human breast fat embedded in ex vivo porcine muscle using a Siemens TIM Trio 3T MRI scanner (Siemens Healthcare, Erlangen, Germany). The sample was sandwiched between two custom-built two-channel RF receiver surface coils for better imaging signal-to-noise ratio (SNR) at the ultrasound focus and was placed in a sample holder. For the experiment, the excised breast fat was kept refrigerated and was used within the first 2 days after excision. To provide proper acoustic coupling, a layer of degassed water was poured between the bottom of the container made of mylar film, and the tissue sample and water filled any space between the excised fat and porcine tissue. Sample heating was performed using a 256-element MRI compatible phased-array ultrasound transducer (Imasonic, Besançon, France) that was housed in a bath of deionized and degassed water. The transducer (1 MHz, 13 cm focal length) was mounted in a computer-controlled, mechanically driven, MRI-compatible positioning system (Image Guided Therapy, Bordeaux, France). The ultrasound power was controlled outside the MR room via the controller computer. A fiber optic temperature probe (OpSens, Inc, Quebec, Canada) was placed at the interface between the fat and the aqueous tissue and high-resolution images of the sample were taken to position the ultrasound focus near the tip of the probe but outside of the direct ultrasound beam path. Figure 2 shows a schematic of the experimental setup used in our experiment.

To simultaneously measure PRF and T_1, the new hybrid Dixon PRF-T_1 sequence was implemented as a modification of a standard segmented EPI sequence. The sequence was implemented by alternating two flip angles every other time frame and two TEs (TE, TE+Δ) every other two time frames, respectively. TE and TE+Δ (where Δ = 1.15 ms at 3T) represent the echo times when water and fat are in phase and 180° out phase, respectively. Finally, flyback lobes were added to the readout echo train to ensure that all k-space lines were acquired in one direction, therefore providing a highly efficient method for acquiring extended 2-point Dixon data in the presence of fat and aqueous tissue. The temperature maps were acquired in four measurements as described in Figure 3.

In practice, temperature quantification using T_1 method necessitates the calibration of T_1 with temperature. Therefore, T_1 calibrations with temperature in

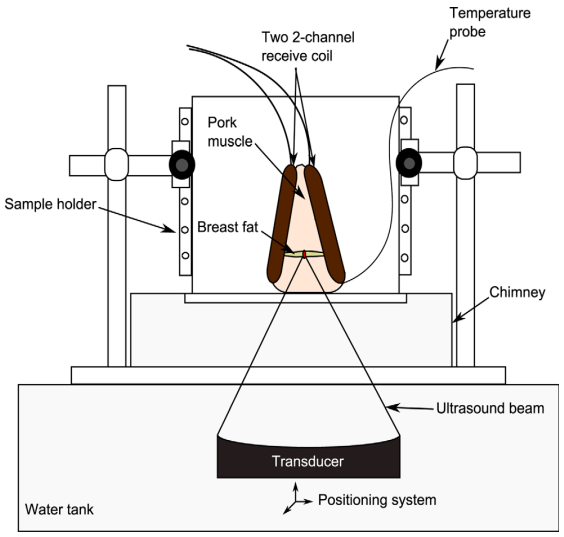

FIG. 2. Experimental setup. Human breast fat, embedded in porcine muscle, was used as a substitute for human breast. The sample was sandwiched between the two custom-built two-channel RF receiver surface coils and placed within the sample holder container. A chimney filled with degassed water ensured an acoustic beam path to the tissues sample.

breast fat samples for four different patients were performed to determine the variability of the average temperature coefficient dT_1/dT and consequently the average relative temperature coefficient (%/°C). These calibration experiments consisted of imaging two vials (inside diameter = 2 cm, height = 5.5 cm) containing breast fat sample while they were cooling. The vials were preheated in a water bath and placed within a thermal insulating Styrofoam block. The temperature of the fat samples were recorded during the cooling phase using two temperature probes (OpSens, Inc, Quebec, Canada) that were inserted in the vials before placing the ensemble within a 16-channel Siemens head coil (Siemens Healthcare, Erlangen, Germany). The temperatures were sampled every 3 minutes for all experiments for 105 minutes on average. Table 1 lists the imaging parameters of the different experiments.

Experiment and Data Processing

T_1 values of the sample were obtained at the beginning of the experiment using the null-point (21) of a conventional two-dimensional inversion recovery (IR) turbo spin echo pulse sequence (TR/TE = 5000/17 ms, 2 × 2 × 3 mm resolution, 7 slices, 128 × 90 image matrix, echo train = 11, TI = [50 200 300 400 800 1000 1200]).

The T_1 values obtained were used to select a minimum TR that provided a good SNR for the two optimum flip angles. The prescribed flip angles that would result in the best T_1 measurement precision were empirically determined from the signal intensity averaged over a large region of interest using the 3D segmented flyback EPI sequence with a range of flip angles from 7° to 87° in 10° increments. The two optimum flip angles were derived from the plot of the normalized signal intensity versus the prescribed flip angles (Fig. 4). To minimize error in T_1, a correct flip angle map of each selected optimum flip angle was obtained using the steps described for Equation [8].

The HIFU heating experiment was performed at three different acoustic powers: 10, 20, and 26 W. The sequence was used to acquire images with coronal slice orientation during the heating and the cooling phases. Scan parameters for the three heating runs were as follows: TR/TE = 20/9.8 ms, readout bandwidth = 640 Hz/pixel, echo train length = 5, image matrix = 128 × 90, 8 slices, and 2 × 2 × 3 mm resolution for a scan time of 3.7 s for a single flip angle. The scan time of 3.7 s included a prescan time of 0.8 s to reach steady state in addition to the actual acquisition time [(90 × 8 × 20)/5 = 2.88 s]. The prescan time was needed before

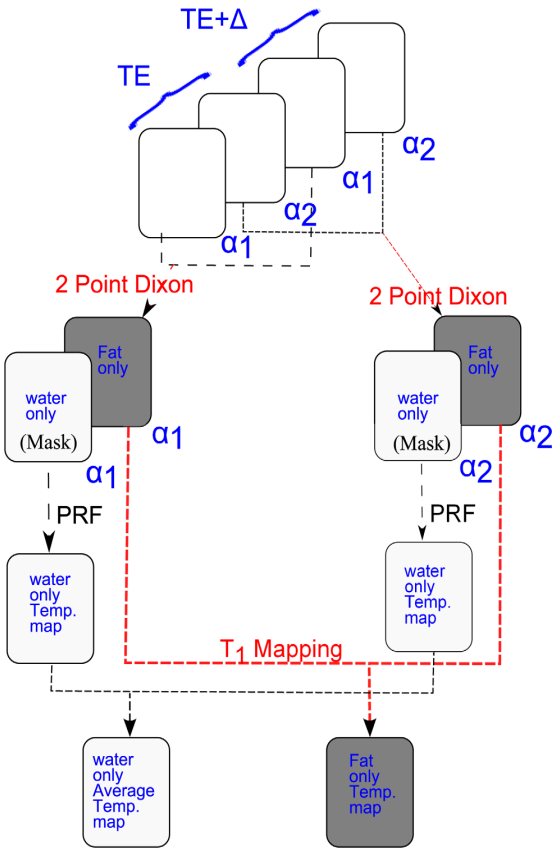

FIG. 3. Schematic diagram of the simultaneous fat and aqueous tissue temperature imaging using the two-point Dixon hybrid PRF-T_1 acquisition method. The two temperature maps, PRF and T_1, are acquired in a series of four images. Images acquired at the same flip angle are combined using the extended two-point Dixon methods to separate fat and aqueous tissues. The water-based tissue-only images are used to mask the original complex images to remove the fat signal. The phases of the aqueous tissue in regions where fat and water voxels overlapped due the chemical shift were computed using Equation [7]. A high SNR PRF temperature map was obtained by averaging over the phase maps of the two FAs. The T_1 map of the fat was computed from the fat-only images using the DFA method.

Table 1
Temperature Dependence of the Spin-Lattice Relaxation Time (T_1) in Breast Fat of Four Patients Acquired during Cooling Experiments

	Patient 1	Patient 2	Patient 3	Patient 4
TR/TE (ms)	30/8	30/11	30/9.8	30/8.6
Image matrix	128 × 31	128 × 39	128 × 31	128 × 31
Voxel size (mm^3)	1.3 × 1.3 × 31	× 1 × 3	1.2 × 1.2 × 32	× 2 × 3
EPI factor	3	3	3	3
Bandwidth (Hz/pixels)	550	454	368	448
Slices	10	18	18	8
Averages	5	5	5	10
Flip angles (°)	13/57	16/63	15/58	15/66
ROI size	5 × 55	× 55	× 55	× 5
Average temperature coefficient (ms/°)	10.97	8.15	6.76	6.21
Average relative temperature coefficient (%/°C)	1.58	1.20	1.37	1.29
Temperature range (°C)	24–65	26–78	25–67	25–68
Correlation coefficient R	0.9875	0.9980	0.9973	0.9956

acquiring each time frame, because the flip angles were alternating from time frame to time frame. Although short TR and TE allow for fast measurement, the PRF method yields the best precision if $TE = T_2^*$ (22–25). The T_2^* value for the muscle is approximately 25 ms (26); therefore, a compromise between short measurement time (short TE, high SNR) and accuracy of the temperature map was necessary.

The readout bandwidth and the echo spacing used in this experiment resulted in a chemical shift of the fat with respect to the aqueous tissue of 1 pixel along the readout direction and 4 pixels in the phase-encoding direction. The empirically determined optimum flip angles were 8° and 35°, respectively. The first two heating runs (10 W and 20 W) focused the beam on a single point and were performed for a duration of 2 min each. The last run of the experiment (26 W) heated a circular trajectory (radius = 2 mm, 13 points, 50 ms/point) for 3 min. A variable time delay, ranging from 10 to 15 min was applied between ultrasound sonications to allow the heated region to cool to within about 5°C of the starting temperature.

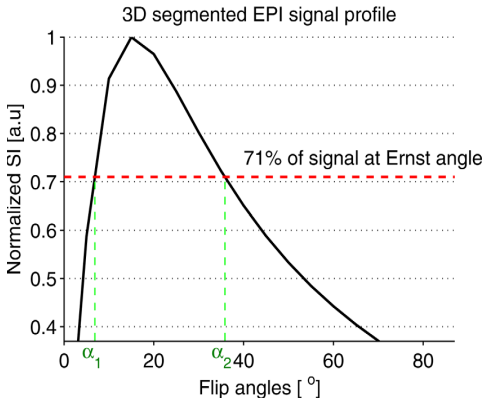

FIG. 4. Plot of the normalized signal intensity (SI) of the 3D segmented flyback EPI sequence versus the flip angles. The maximum T_1 precision is achieved by choosing the flip angles such that $SI_{a1} = SI_{a2} = 71\%$ of the SI at Ernst angle α_E. The plot is zoomed in to show the locations of the two optimal flip angles.

Image reconstruction, fat-water image processing, and the calculation of temperature maps were performed offline with MATLAB (MathWorks, Natick, MA). The individual coil images of each heating run were decomposed into fat and water magnitude images using the extended two-point Dixon method. The decomposed fat and water magnitude images from each coil were then combined using the "sum-of-squares" method (27), which effectively computes the root-mean-square average of the images associated with the different coils. To calculate the PRF temperature maps, the original complex images were reconstructed using a multicoil algorithm that combines the phase differences between adjacent time frames weighted by the square of the magnitudes. The water-only images were used to mask the combined complex images before computing the PRF shift. Averaging of the phase maps of the two optimum flip angles was used to improve the SNR of the temperature maps. The thermal coefficient $\beta = -0.01$ ppm/°C was used for PRF thermometry calculation.

The values of the spin-lattice relaxation time T_1 were calculated from the fat-only images at the two optimum flip angles following the steps described earlier. Before obtaining the T_1 maps, the image noise was reduced by applying a Hanning filter to the raw data.

RESULTS

Temperature images of the 3D volume of the phantom were obtained with a 14.8 s temporal resolution and 2 × 2 × 3 mm spatial resolution. Figure 5 shows the T_1 maps of the fat in slices 4, 5, and 6, which were computed using the DFA method as described earlier. Figure 5b shows T_1 rise with temperature at the focal point in the fat sample during the HIFU heating.

Figure 6 shows on the top row the zoomed in PRF temperature maps of the eight coronal slices of the aqueous tissue of the phantom during the HIFU heating run 2. All coronal slices show temperature rise at the focus of the ultrasound beam except slice 5 (Fig. 6e) which contains fat at that location. Because fat does not show a temperature-dependent frequency shift, the localized fat signals have been removed from slices 4, 5, and 6

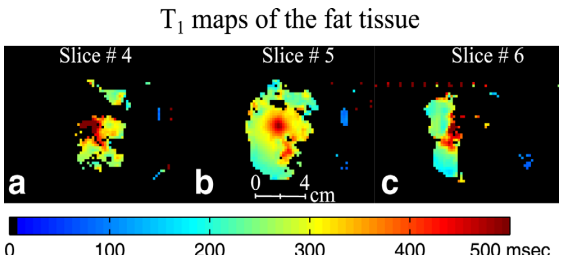

FIG. 5. HIFU heating experiment results for run 2 (20 watts). T_1 maps at the peak temperature of the fat in slice 4 (**a**), slice 5 (**b**), and slice 6 (**c**). After separating water and fat signals using the extended two-point Dixon method, the T_1 maps of fat were obtained using the DFA method.

(Fig. 6d, 6e, and 6f) using the extended two-point Dixon method beforehand. The locations of the fat signal in these slices are indicated by arrows. All the slices are shown in the plane perpendicular to the HIFU beam path. The bottom row of Figure 6 shows the temperature maps of the fat tissue obtained from the T_1 maps from Figure 5 using the results of the calibration of T_1 with temperature in Figure 8.

To validate T_1 values derived from the DFA method, T_1 maps were calculated using the IR and the DFA methods of the 10 coronal slices of the two samples of the breast fat tissue from patient 1 (Fig. 7a). The images of IR and DFA were acquired with the same spatial resolution ($1.3 \times 1.3 \times 0.3$ mm), and the locations of the slices were identical. Although the fat sample did not contain a large amount of water (<5%), T_1 images using DFA were computed on fat-only images as described in Figure 3, while IR images were computed in mixed fat and water. Figure 7b shows the line plots along the green dashed line in Figure 7a. Figure 7c shows the error bar plots of the means and the standard deviations of T_1 computed over a 7×7 pixel region of interest (ROI) in the 10 coronal slices using the IR and the DFA methods, respectively. The means and standard deviations were calculated from the combined T_1 values from the two vials over the ROIs shown by the black squares on the T_1 maps of slice 2 derived from the IR and the DFA methods. The average mean values of T_1 from the 10 slices were found to be 280 ± 25 ms for IR and 282 ± 18 ms for DFA.

T_1 calibration with temperature for the HIFU experiment was performed in fat over a 2x2 voxel ROI chosen

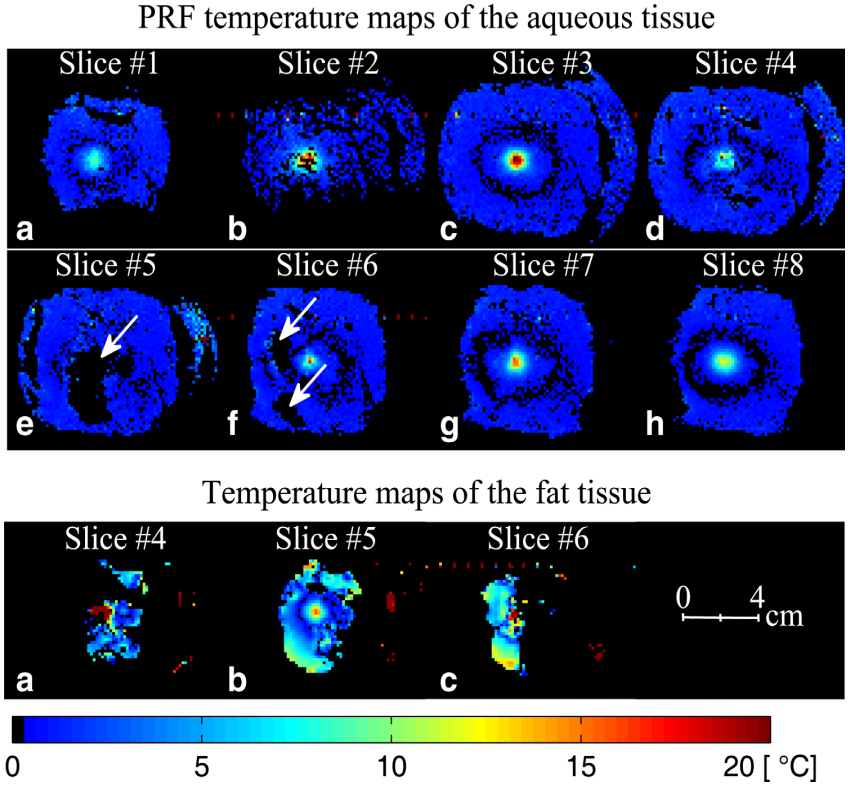

FIG. 6. HIFU heating experiment results for run 2 (20 W). The top two rows show PRF temperature maps at the peak temperature of the eight coronal slices (perpendicular to the HIFU beam) of the aqueous tissue in the 3D volume. PRF temperature maps of these coronal slices were obtained by removing the fat signal using the extended two-point Dixon methods. The arrows indicate the locations of the removed fat signal. In the regions where fat and water voxels overlapped due to the chemical shift, the water phase was calculated based on the fraction of fat and water in each voxel, the fat background phase, and the resulting signal intensity in those voxels before the fat/water separation. The bottom row shows temperature maps of the fat tissue in slices 4, 5, and 6 obtained from the T_1 maps in Figure 5. The temperature maps were calculated using the average T_1 calibration coefficients obtained in Figure 8.

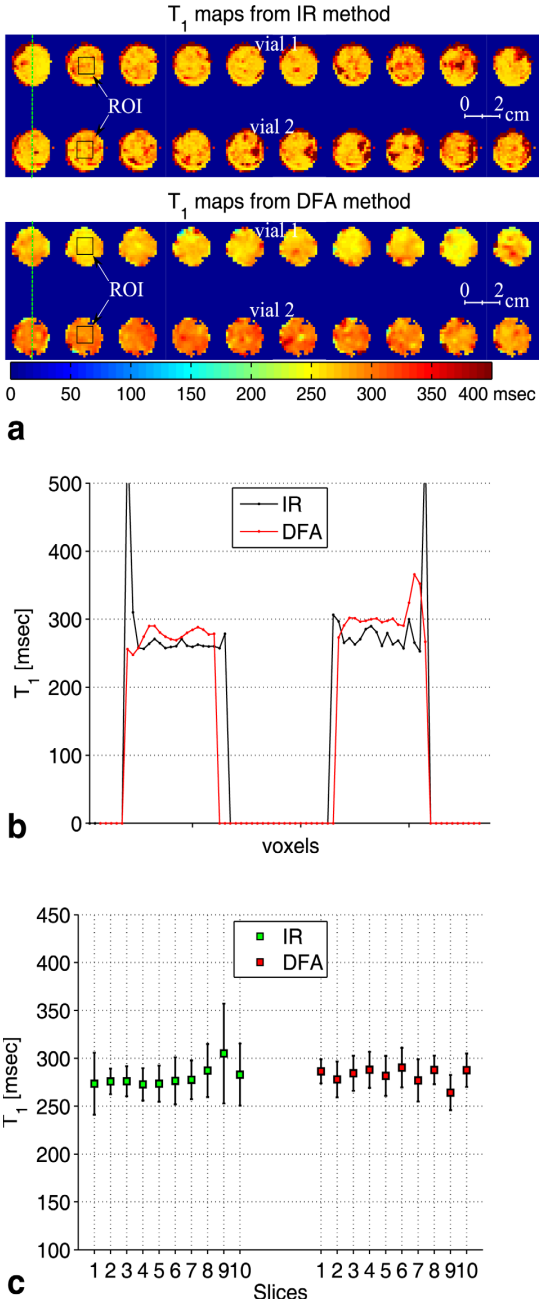

FIG. 7. a: The top row shows zoomed-in T_1 maps of the 10 coronal slices in ascending order of the breast fat tissue from patient 1 (see Table 1) computed using the inversion recovery (IR) method. The bottom row shows T_1 maps of the same coronal slices using the DFA method. **b:** Line plots along the green dashed lines on the IR and the DFA T_1 maps of slice 1. **c:** Error bar plots of the T_1 maps of the 10 slices. The error bar plots show the mean and the standard deviation of T_1 calculated over an ROI of 7×7 pixels shown by the black squares on slice 2 of the T_1 maps obtained from the IR and the DFA methods.

near the tip of the fiber optic temperature probe. Figure 8 is a plot of the absolute T_1 versus the temperature reading of the fiber optic temperature probe during the HIFU heating and cooling phases of the sample for the heating runs at 10, 20 and 26 watts respectively. The recorded temperatures via the fiber optic temperature probe during the experiment have a precision of ± 0.5°C below 40°C according to the temperature probe manufacturer. To estimate the precision of T_1 values, the standard deviation of the absolute T_1 have been measured in a uniform, non-heated region and was found to be ± 5 ms. From Figure 8a-c, it can be seen that T_1 changes linearly with temperature with an average temperature coefficient of 11.2 ms/°C.

Similarly, PRF temperature rise in aqueous tissue for the three HIFU heating runs over the same ROI location in all eight slices was calculated and plotted versus the time in Figure 9. The offset between the location of the fat and water spins due to the chemical shift was corrected while choosing the corresponding ROI in aqueous tissue. The plots of the PRF temperature versus the time show that the fat voxels in slice 5 experienced a small change of PRF temperature over time, which is either the result of the B_0 field drift of the MRI scanner or to the result of a susceptibility change due to heating of the tissue sample.

The cooling experiments show that T_1 of breast fat is linear with temperature over a larger temperature range up to 78°C. Similarly, the temperature coefficients vary from 6.21 to 10.97 ms/°C, which confirms the tissue dependence of T_1. To compensate for tissue variability of T_1, the relative temperature coefficients were also calculated and ranged from 1.2 to 1.58 %/°C.

DISCUSSION AND CONCLUSION

The results presented herein demonstrate the 3D fat and water temperature imaging capability of a new acquisition scheme based on an extended two-point Dixon fat and water separation and the DFA T_1 mapping techniques. Visual inspection of the PRF temperature maps of the eight slices in Figure 5 and the T_1 map values of the fat in Figure 6 demonstrate the effectiveness of the extended two-point Dixon method in separating fat and water signals.

The carefully chosen TE value used for this experiment provided high imaging SNR, which has improved the accuracy of the fat water decomposition method. Furthermore, in voxels where fat and water signals overlap due to the chemical shift, the method presented in this paper allows the phase of water to be calculated with minimum error. The calculation is made possible by assuming that the fat phase is the same as that of the nearest fat-only voxel and remains constant throughout the treatment. This assumption appears reasonable from the results shown in Figure 9, as the phase from the fat region in slice 5 (the only slice without partial water signal) changes very little during heating and only slightly more during cooling. These small changes will induce only a small error in the water phase calculation and affect only mixed fat/water voxels.

Although B_1 mapping can be challenging and is prone to errors in DFA T_1 calculation, the comparison of our T_1 maps with the ones derived from the IR method (Fig. 7) shows that the DFA method achieved the same

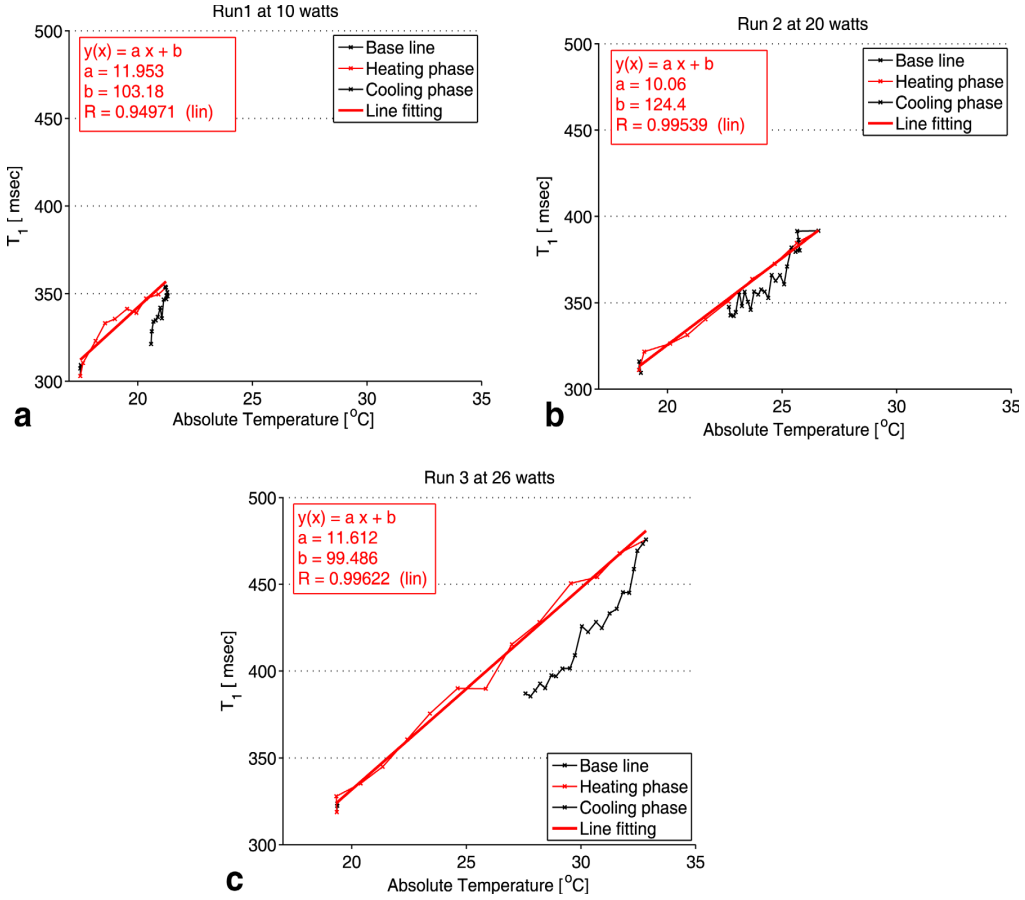

FIG. 8. T_1 profile in slice 5. All measurements were performed in adipose tissue. The plot of the absolute T_1 versus the temperature reading of the fiber optic temperature probe is shown for each of the three HIFU heating runs: 10W (**a**), 20 W (**b**), and 26 W (**c**). T_1 was computed over an ROI of 2 × 2 pixels near the tip of the fiber optic temperature probe. The standard deviation of the absolute T_1 change was ±5 ms.

bulk of T_1 values in the 10 coronal slices of the fat sample from patient 1.

Additionally, one of the prerequisites for successful T_1 monitoring of thermal therapy is stability over the entire treatment period. The data from our study demonstrate the stability of T_1 determination during the application of several individual sonications. Moreover, the average temperature coefficients dT_1/dT was found to be 11.2 ms/°C with a relative value of 2.6%/°C in the HIFU heating experiments and values ranging from 6.21 to 10.97 ms/°C with relative values from 1.2 to 1.58 %/°C in the water bath cooling experiments. Although the voxels for

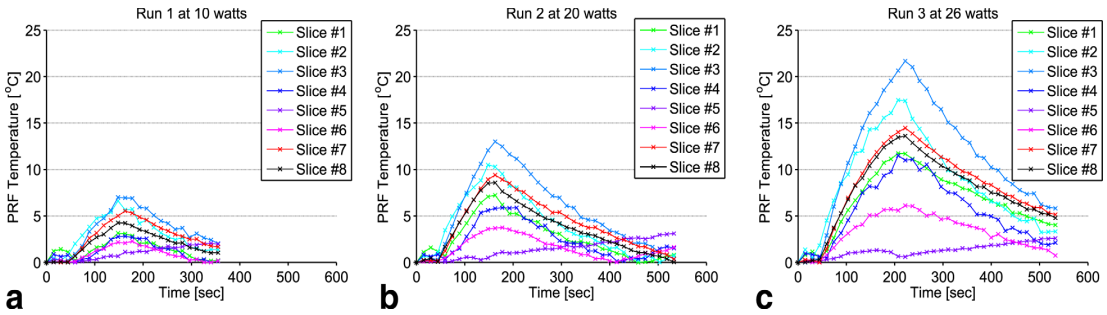

FIG. 9. (a-c) Plots of the PRF temperature versus the time of the corresponding ROI of 2 × 2 pixels described in Figure 8**.** All of the measurements were made in the aqueous tissue for each of the three heating runs: 10W (**a**), 20 W (**b**), and 26 W (**c**). The offset between the location of the fat and the water voxels due to the chemical shift was corrected while choosing the ROI in aqueous tissue.

T_1 measurement were chosen to be as close as possible to the fiber optic probe location, uncertainty in that location also has an effect on the value of the slope obtained. To reduce that error, the voxels were chosen to minimize the hysteresis in the plot of T_1 versus the probe temperature. When the T_1 measurement and the probe are not in the same location, hysteresis occurs because of the difference in time for the heat from the ultrasound focus to diffuse to the two locations.

A small variation was noted in the T_1 dependence on temperature for the four subjects included in Table 1. If this range of sensitivities is typical of the population of women to be encountered in thermal therapies, this intersubject variation could result in some error in the fat temperatures estimated during thermal procedures. For example, using the T_1 thermal coefficient of patient 4 to estimate the temperature change in the 40°C range in the fat tissue of patients 1, 2, and 3 could result in 43%, 23%, and 8% overestimation, respectively, of the temperature of the fat in those patients during real-time thermal therapy. Note that breast cancer usually originates in the fibroglandular tissue, and the goal of T_1 estimation is to monitor and minimize temperature rise in the surrounding healthy fatty tissue. However, if the range of T_1 dependencies is large, it may be useful to find a way to calibrate the temperature dependence on each subject. This calibration might be done by using voxels that contain both fat and water. In fact, it might be possible to use the knowledge of PRF temperature in water in mixed fat/water voxels to calibrate the temperature dependence of T_1 in fat. The accuracy of this method will require (a) a voxel that is large enough to yield sufficient signal from both fat and water and (b) a small temperature gradient across the voxel.

Imaging time is often a concern with any MR thermometry technique requiring multiple image acquisitions. Therefore, real-time control of thermal ablation procedures in immobilized organs such as the human breast (28) requires a method that has good temporal and spatial resolution, provides sufficient thermometry precision, and is easy to implement. The pulse sequence used in our study is easy to implement and has good spatial resolution. Although the proposed technique for simultaneous temperature mapping in fat and water is not currently practical for clinical applications due to the long acquisition time (14.8 s for the four image volumes of one complete set of temperature maps), the temporal resolution can be considerably improved by calculating PRF temperatures from each pair of flip angles and also by implementing a parallel acquisition technique. For instance, GRAPPA [GeneRalized Autocalibrating Partially Parallel Acquisitions (29–31)] with an accelerated factor of 4, which is common for 3D sequences in the clinical setting, can reduce the acquisition time by four-fold with little sacrifice in accuracy of the temperature maps. In addition to increased temporal resolution at a given spatial resolution, the time savings of a parallel acquisition technique can also be used to improve the spatial resolution in a given imaging time. However, the time can also be reduced by having more echoes in the EPI echotrain.

The precision of T_1 measurements using the variable flip angle technique depends on using an accurate estimate of the actual local flip angles. B_1 inhomogeneity causes a spatial variation in the flip angle and therefore needs to be corrected. Simulations investigating T_1 accuracy as a function of the nominal flip angle, demonstrated that the results were highly sensitive to imprecision in flip angle, with T_1 error $> 10\%$ with a 5% deviation in flip angle (32). Although B_1 mapping over the entire volume requires several minutes of acquisition and processing, it has to be performed only once and then can be used throughout the procedure. Moreover, in 3D imaging, RF pulse profile errors are minimal if the region of interest is centered in the excited 3D slab, like the fat slices in this experiment, or if the slab-select gradient is turned off. Additionally, a custom-designed Shinnar-Le Roux selective excitation pulse (33) or fast passage adiabatic pulses can be used to optimize T_1 accuracy.

In conclusion, the ability of real-time simultaneous temperature mapping in fat and aqueous tissue during HIFU ablation has been demonstrated in ex vivo tissue samples. The sequence uses a segmented EPI read-out to shorten the scanning time and an acquisition method to produce simultaneous temperature maps of fat and aqueous tissue during thermal therapy. The technique has shown stability and reliability during the thermal ablation. Studies demonstrating the applicability of this new technique in vivo are ongoing. The results of this investigation in conjunction with reducing the acquisition time of the temperature maps will be presented in future work.

ACKNOWLEDGMENTS

The authors appreciate helpful contributions from Joshua de Bever, Leigh Neumayer, and other collaborators at the University of Utah.

REFERENCES

1. Hynynen K, McDannold N, Mulkern RV, Jolesz FA. Temperature monitoring in fat with MRI. Magn Reson Med 2000;43:901–904.
2. Graham SJ, Bronskill MJ, Henkelman RM. Time and temperature dependence of MR parameters during thermal coagulation of ex vivo rabbit muscle. Magn Reson Med 1998;39:198–203.
3. Kuroda K OK, Mulkern RV, Jolesz FA. Optimization of chemical shift selective suppression of fat. Magn Reson Med 1996;40:505–510.
4. Vandeweyer E, Hertens D. Quantification of glands and fat in breast tissue: an experimental determination. Ann Anat 2002;184:181–184.
5. Dimitrov IE, Douglas D, Ren J, Smith NB, Webb AG, Sherry AD, Malloy CR. In vivo determination of human breast fat composition by ^{1}H magnetic resonance spectroscopy at 7 T. Magn Reson Med 2012; 67:20–26.
6. Gandhi S, Daniel B, Butts K. Temperature Dependence of Relaxation Times in Bovine Adipose Tissue. In Proceedings of the 6th Annual Meeting of ISMRM, Sydney, Australia, 1998. p. 701.
7. Lam MK IT, Saito K, Kuruda K. Effect of Water Resonace Thermal Shift on Methylene T1 Estimation with Multiple Flip Angle Multipoint Dixon Technique for Fat Temperature Imaging. In Proceedings of the 19th Annual Meeting of ISMRM, Stockholm, Sweden, 2010. p. 4128.
8. Kuroda K, Iwabuchi T, Obara M, Honda M, Saito K, Imai Y. Temperature dependence of relaxation times in proton components of fatty acids. Magn Reson Med Sci 2011;10:177–183.
9. Skinner TE, Glover GH. An extended two-point Dixon algorithm for calculating separate water, fat, and B0 images. Magn Reson Med 1997;37:628–630.
10. Deoni SC, Rutt BK, Peters TM. Rapid combined T1 and T2 mapping using gradient recalled acquisition in the steady state. Magn Reson Med 2003;49:515–526.

11. Cusack R, Papadakis N. New robust 3-D phase unwrapping algorithms: application to magnetic field mapping and undistorting echo-planar images. Neuroimage 2002;16:754–764.
12. Quesson B, de Zwart JA, Moonen CT. Magnetic resonance temperature imaging for guidance of thermotherapy. J Magn Reson Imaging 2000;12:525–533.
13. Rieke V, Butts Pauly K. MR thermometry. J Magn Reson Imaging 2008;27:376–390.
14. Ishahara Y, Calderon A, Watanabe H, Okamoto K, Suzuki Y, Kuroda K, Suzuki Y. A precise and fast temperature mapping using water proton chemical shift. Magn Reson Med 1995;34:814–823.
15. Sprinkhuizen SM, Bakker CJ, Ippel JH, Boelens R, Viergever MA, Bartels LW. Temperature dependence of the magnetic volume susceptibility of human breast fat tissue: an NMR study. MAGMA 2012;25: 33–39.
16. Deoni SC, Peters TM, Rutt BK. Determination of optimal angles for variable nutation proton magnetic spin-lattice, T1, and spin-spin, T2, relaxation times measurement. Magn Reson Med 2004;51:194–199.
17. Schabel MC, Morrell GR. Uncertainty in T(1) mapping using the variable flip angle method with two flip angles. Phys Med Biol 2009;54: N1–N8.
18. Stollberger Rudolf, Paul W. Imaging of the active B1 field in vivo. Magn Reson Med 2005;35:246–251.
19. Parker DL. Applications of NMR imaging in hyperthermia: an evaluation of the potential for localized tissue heating and noninvasive temperature monitoring. IEEE Trans Biomed Eng 1984;31:161–167.
20. Cline HE, Schenck JF, Watkins RD, Hynynen K, Jolesz FA. Magnetic resonance-guided thermal surgery. Magn Reson Med 1993;30:98–106.
21. Melhem ER, Jara H, Shakir H, Gagliano TA. Fast inversion-recovery MR: the effect of hybrid RARE readout on the null points of fat and cerebrospinal fluid. AJNR Am J Neuroradiol 1997;18:1627–1633.
22. Stafford RJ, Price RE, Diederich CJ, Kangasniemi M, Olsson LE, Hazle JD. Interleaved echo-planar imaging for fast multiplanar magnetic resonance temperature imaging of ultrasound thermal ablation therapy. J Magn Reson Imaging 2004;20:706–714.
23. Kuroda K, Mulkern RV, Oshio K, Panych LP, Nakai T, Moriya T, Okuda S, Hynynen K, Jolesz FA. Temperature mapping using the water proton chemical shift: self-referenced method with echo-planar spectroscopic imaging. Magn Reson Med 2000;44:167.
24. de Zwart JA, van Gelderen P, Kelly DJ, Moonen CT. Fast magnetic-resonance temperature imaging. J Magn Reson B 1996;112:86–90.
25. Oros-Peusquens AM, Laurila M, Shah NJ. Magnetic field dependence of the distribution of NMR relaxation times in the living human brain. MAGMA 2008;21:131–147.
26. Chung AH, Hynynen K, Colucci V, Oshio K, Cline HE, Jolesz FA. Optimization of spoiled gradient-echo phase imaging for in vivo localization of a focused ultrasound beam. Magn Reson Med 1996;36: 745–752.
27. Roemer PB, Edelstein WA, Hayes CE, Souza SP, Mueller OM. The NMR phased array. Magn Reson Med 1990;16:192–225.
28. de Senneville BD, Ries M, Bartels LW, Moonen CTW. MRI-guided high-intensity focused ultrasound sonication of liver and kidney. In: Kahn T, Busse H, editors. Interventional magnetic resonance imaging. Heidelberg, Germany: Springer-Verlag; 2011. p. 349–366.
29. Blaimer M, Breuer F, Mueller M, Heidemann RM, Griswold MA, Jakob PM. SMASH, SENSE, PILS, GRAPPA: how to choose the optimal method. Top Magn Reson Imaging 2004;15:223–236.
30. Blaimer M, Breuer FA, Mueller M, Seiberlich N, Ebel D, Heidemann RM, Griswold MA, Jakob PM. 2D-GRAPPA-operator for faster 3D parallel MRI. Magn Reson Med 2006;56:1359–1364.
31. Blaimer M, Breuer FA, Seiberlich N, Mueller MF, Heidemann RM, Jellus V, Wiggins G, Wald LL, Griswold MA, Jakob PM. Accelerated volumetric MRI with a SENSE/GRAPPA combination. J Magn Reson Imaging 2006;24:444–450.
32. Deoni SC, Peters TM, Rutt BK. High-resolution T1 and T2 mapping of the brain in a clinically acceptable time with DESPOT1 and DESPOT2. Magn Reson Med 2005;53:237–241.
33. Pauly J, Le Roux P, Nishimura D, Macovski A. Parameter relations for the Shinnar-Le Roux selective excitation pulse design algorithm (NMR imaging). IEEE Trans Med Imaging 1991;10:53–65.

CHAPTER VII

SUMMARY AND FUTURE WORKS

Over the last several years, focused ultrasound therapy under MRI guidance has gained momentum with several applications getting FDA approval. For many applications using real-time MRI temperature monitoring, PRF is the method of choice due to its simplicity, linearity with temperature, and ease of use. However, its inability to measure temperature in fatty tissue limits the scope of its application. Nonetheless, T_1 which is related to the translational and rotational rates of water represents an intrinsic probe for investigating structural changes in tissues at high temperature. It has also shown temperature dependence and has been proven to work in all types of tissue. Therefore, we demonstrated that by combining these two methods, one can get more useful information which will ultimately improve the safety of the thermal treatment.

In this dissertation, a number of challenges affecting MRI thermometry have been covered. A TSE pulse sequence design has been proposed that provides extra information such as temperature and is expected to enable reasonable temperature measurements for the evaluation of any possible heating associated with TSE sequences.

Monitoring temperature during thermal therapy is essential for the safety and efficacy of the treatment. PRF has shown the best ability to provide in real time the temperature of a tumor and its surrounding tissues (except fat). Unfortunately, it cannot determine directly the

degree of damage induced in the tumor. Therefore, we have developed a method that combines PRF and T_1 which allows real time assessment of the tissue damage.

Moreover, temperature monitoring during thermal therapy of mixed fat/aqueous tissue can be particularly challenging. Therefore, we have also addressed the issue by developing a new pulse sequence and acquisition scheme that provide simultaneously the temperature map of aqueous tissue and T_1 map of fat. The methods proposed in this dissertation can be summarized as follows.

7.1 Modified Turbo Spin Echo Sequence-Based Thermometry

The high-contrast properties and inherent insensitivity of a TSE sequences to RF and magnetic field inhomogenities makes it an attractive sequence in a high field clinical setting where susceptibility effects can be quite a problem. However, the increase of RF power deposition can severely limit the coverage possible in multislice application at high field (3T and higher), since SAR increases as the square of the field strength as well as the flip angle. Therefore, the sequence has been rendered sensitive to off-resonance by shifting the echo away from the time of the spin echo. Thus, this simple sequence modification allows TSE to be used safely and prevents the temperature change due to SAR from exceeding a threshold temperature set by the user of the sequence.

7.2 Irreversible Change in the T_1 Temperature Dependence with Thermal Dose Using the PRF-T_1 Technique

Assessment of tissue damage during thermal therapy is essential for the safety and efficacy of any thermal treatment. Several methods have been developed and published in

the literature for assessing the extent of thermal damage. Herein we have proposed a hybrid PRF-T_1 method that can provide simultaneously in real time during a thermal treatment the temperature information (indirectly the thermal dose) and T_1 information which is a good indication of the state of the tissue. HIFU heating experiments on chicken breast samples have shown that T_1 is reversible with temperature before tissue damage and irreversible with temperature after tissue damage has occurred. The simplicity and the real-time capability of the newly developed hybrid PRF-T_1 makes it an ideal tool for assessing tissue damage.

However, more in vivo experiments need to be performed to confirm the hereby presented results. Also the knowledge of T_1 change threshold calculation might increase the safety of this technique by providing warning to the physician before the surrounding normal tissue is overexposed.

7.3 Toward Real-Time Temperature Monitoring in Fat and Aqueous Tissue during MRgHIFU Using 3D PRF-T_1 Method

Thermal therapy in organs with large fat content such as breast has been hindered by the inability of MRI thermometry in fat since there is no hydrogen bonding among the methylene protons that supply the bulk of the fat signal. Therefore, we have presented in this dissertation a pulse sequence implementation and a new acquisition scheme that allow simultaneously the determination of the PRF temperature in aqueous tissue and T_1 map in fat. T_1 calibration with temperature has been also investigated in five breast fat samples from different patients. A small variation was noted in the T_1 dependence on temperature for the subjects included in this study. However, the results have shown the feasibility of real time temperature monitoring in mixed fat/water tissue.

The variability of the temperature coefficient of T_1 with fatty tissues which is an intrinsic characteristic of T_1 is being investigated to find a noninvasive way to calibrate T_1 with temperature.

7.4 Conclusions

In this dissertation, several pulse sequence implementations and techniques have been described to improve and to overcome some of the limitations of the current methods in MRI thermometry. A pulse sequence was developed to monitor temperature rise while using TSE sequence, a hybrid PRF-T_1 sequence was implemented to assess in real time tissue damage during thermal therapy, and an image acquisition scheme and a sequence implementation were shown to monitor simultaneously temperature in mixed fat/water tissue. The proposed methods provide a step towards more robust and reliable temperature monitoring during thermal therapy under MRI guidance.

7.5 Future Works

Thermal therapy using HIFU under MRI guidance is making good progress towards its acceptance as one of the clinical routines. However, there are still a lot of technical issues that need attention and remain to be solved. During the experiments presented in this dissertation, several limitations have been found where some improvements in those areas can significantly increase the accuracy and the precision of the results presented herein. In this section, some of the main limitations are briefly addressed with potential solutions and suggestions.

- The precision of T_1 calculation using the VFA method is highly sensitive to B_1 map across the imaged object. In this dissertation, the method presented for B_1 mapping (DFA) assumes the linearity of the gain of the RF transmitter with B_1

field which is not always the case, specifically at low flip angle (1^o to ~20^o) depending on the pulse sequence. This hardware limitation can be sometimes a dominant factor of bias in T_1 measurement. In this case, one can explore other methods for accurate B_1 mapping at low flip angle such as Low Angle Mapping (LAM) (154). This method is based on the approximation that B_1 inhomogeneities have a negligible effect on the signal at 90^o flip angle. The method has shown good results for small flip angles compare to the others B_1 mapping methods and should be used in conjunction with the DFA method.

REFERENCES

1. Tanaka H, Eno K, Kato H, Ishida T. Possible application of non-invasive thermometry for hyperthermia using NMR. Nihon Igaku Hoshasen Gakkai Zasshi 1981;41(9):897-899.

2. Parker DL, Smith V, Sheldon P, Crooks LE, Fussell L. Temperature distribution measurements in two-dimensional NMR imaging. Med Phys 1983;10(3):321-325.

3. Abragam, A. The principles of nuclear magnetism. Oxford University Press, Oxford; 1983.

4. Johnson F, Eyring H, Stover B. Theory of rate processes in biology and medecine. New York: John Wiley & Sons; 1974.

5. Chen J, Daniel BL, Pauly KB. Investigation of proton density for measuring tissue temperature. J Magn Reson Imaging 2006;23(3):430-434.

6. Bloembergen N, Purcell EM, RV P. Relaxation effects in nuclear magnetic resonance absorption. Phys Rev 1948;73:679-712.

7. Parker DL. Applications of NMR imaging in hyperthermia: an evaluation of the potential for localized tissue heating and noninvasive temperature monitoring. IEEE Trans Biomed Eng 1984;31(1):161-167.

8. Bottomley PA, Foster TH, Argersinger RE, Pfeifer LM. A review of normal tissue hydrogen NMR relaxation times and relaxation mechanisms from 1-100 MHz: dependence on tissue type, NMR frequency, temperature, species, excision, and age. Med Phys 1984;11(4):425-448.

9. Cline HE, Schenck JF, Watkins RD, Hynynen K, Jolesz FA. Magnetic resonance-guided thermal surgery. Magn Reson Med 1993;30(1):98-106.

10. Lewa CJ, Majewska Z. Temperature relationships of proton spin-lattice relaxation time T1 in biological tissues. Bull Cancer 1980;67(5):525-530.

11. Cline HE, Hynynen K, Hardy CJ, Watkins RD, Schenck JF, Jolesz FA. MR temperature mapping of focused ultrasound surgery. Magn Reson Med 1994;31(6):628-636.

12. Matsumoto R, Oshio K, Jolesz FA. Monitoring of laser and freezing-induced ablation in the liver with T1-weighted MR imaging. J Magn Reson Imaging 1992;2(5):555-562.

13. Hynynen K, McDannold N, Mulkern RV, Jolesz FA. Temperature monitoring in fat with MRI. Magn Reson Med 2000;43(6):901-904.

14. Graham SJ, Bronskill MJ, Henkelman RM. Time and temperature dependence of MR parameters during thermal coagulation of ex vivo rabbit muscle. Magn Reson Med 1998;39(2):198-203.

15. Gandhi S, Cain C, Butts K. Temperature Dependence of Relaxation Times in Bovine Adipose Tissue. Proceedings of the 5th Annual Meeting of ISMRM, Vancouver, Canada1996, p. 701.

16. Le Bihan D, Delannoy J, Levin RL. Temperature mapping with MR imaging of molecular diffusion: application to hyperthermia. Radiology 1989;171(3):853-857.

17. Stejskal EO, Tanner JE. Spin diffusion measurements. J Chem Phus 1965;42:288-292.

18. Morvan D, Leroy-Willig A, Malgouyres A, Cuenod CA, Jehenson P, Syrota A. Simultaneous temperature and regional blood volume measurements in human muscle using an MRI fast diffusion technique. Magn Reson Med 1993;29(3):371-377.

19. Moseley ME, Cohen Y, Kucharczyk J, Mintorovitch J, Asgari HS, Wendland MF, Tsuruda J, Norman D. Diffusion-weighted MR imaging of anisotropic water diffusion in cat central nervous system. Radiology 1990;176(2):439-445.

20. Young IR, Hand JW, Oatridge A, Prior MV. Modeling and observation of temperature changes in vivo using MRI. Magn Reson Med 1994;32(3):358-369.

21. Graham SJ, Stanisz GJ, Kecojevic A, Bronskill MJ, Henkelman RM. Analysis of changes in MR properties of tissues after heat treatment. Magn Reson Med 1999;42(6):1061-1071.

22. Hindman JC. Proton resonance shift of water in gas and in liquid states. J Chem Phys 1966;44:4582-4592.

23. Ishahara Y CA, Watanabe H, Okamoto K, Suzuki Y, Kuroda k, Suzuki Y. A precise and fast temperature mapping using water proton chemical shift. Magnetic Resonance in Medecine 1995;34:814-823.

24. De Poorter J, De Wagter C, De Deene Y, Thomsen C, Ståhlberg F, Achten E. Noninvasive MRI thermometry with the proton resonance frequency (PRF) method:

in vivo results in human muscle. Magn Reson Med 1995;33(1):74-81.

25. De Poorter J. Noninvasive MRI thermometry with the proton resonance frequency method: study of susceptibility effects. Magn Reson Med 1995;34(3):359-367.

26. Nemethy G, Ha S. Structure of water and hydrophobic bonding in proteins. J Chem Phys 1962;36:3386-3392.

27. Schneider WG, Bernstein HJ, JA P. Proton magnetic resonance chemical shift of free (gaseous) and associated (liquid) hydride molecules. J Chem Phys 1958;28:601-607.

28. Rieke V, Butts Pauly K. MR thermometry. J Magn Reson Imaging 2008;27(2):376-390.

29. Quesson B, de Zwart JA, Moonen CT. Magnetic resonance temperature imaging for guidance of thermotherapy. J Magn Reson Imaging 2000;12(4):525-533.

30. Lam MK, Iwabbuchi T, Saito K, Kuruda K. Effect of Water Resonace Thermal Shift on Methylene T1 Estimation with Multiple Flip Angle Multipoint Dixon Technique for Fat Temperature Imaging. Proceedings of the 19th Annual Meeting of ISMRM, Stockholm, Sweden2010, p 4128.

31. Haacke EM, Brown RW, Thompson MR, R V. Magnetic Resonance imaging Physical principles and Sequences Design. New York: Wiley & Sons; 1999.

32. Lauterbur P. Image formation by induced local interactions: examples employing nuclear magnetic resonance. Nature 1973:190-242.

33. Mansfield P. NMR 'diffraction' in solids? Phys C:Solid State Phys 1973;6:L422-L427.

34. Damadian R. Tumor detection by nuclear magnetic resonance. Science 1971;171(3976):1151-1153.

35. kumar A, Welti D, Ernst R. NMR Fourier zeugmatography. J Magn Reson 1975;18:69-83.

36. Levitt MH. Spin Dynamics: Basics of Nuclear Magnetic Resonance. edition n, editor. New York: John Wiley & Sons; 2008.

37. Chen CN, Hoult D. Biomedical Magnetic Resonance Technology. New York: IOP Publishing Ltd; New York 1993.

38. Debye P. Polar Molecules (Chemical Catalogue). 1929. p-90.

39. Liang Z, Lauterbur PC. Principles of Magnetic Resonance Imaging, A signal

Processing Perspective. New York: IEEE PRESS; 1999.

40. Woesser D.E. Effects of Diffusion in Nuclear Magnetic Resonance Spin-echo experiments. J Chem Phys 1961;34:2057-2061.

41. Likes R.S. Moving Gradient Zeugmatography. US patent 4307343 issued 1981-12-22, assigned to General Electric Compagny.

42. Kuroda K, Iwabuchi T, Obara M, Honda M, Saito K, Imai Y. Temperature dependence of relaxation times in proton components of fatty acids. Magn Reson Med Sci 2011;10(3):177-183.

43. Press W, Flannery B, Teukolsky S, W. V. Numerical Recipes in C: The Art of Scientific computing. New York: Cambridge University Press; 1992.

44. Look DC, Locker DR. Time Saving in Measurement of NMR and EPR Relaxation Times. The Review of Scientific Instruments 1970;41(2).

45. Christensen KA, Grand DM, Schulman EM, C W. Optimal Determination of Relaxation Times of Fourier Transform nuclear Magnetic Resonance. Determination of Spin-Lattice Relaxation Times in Chemically Polarized Species. J Phys Chem 1974;78:1971-1977.

46. Holmes J, Roberts JK. Conditions for the Driven Equilibrium Single Pulse Observation of Spin-Lattice Relaxation Times. J Magn Reson 1987;74:424-432.

47. Homer J, Beevers MS. Driven-Equilibrium Single-Pulse observation of T1 Relaxation. A Re-evaluation of a Rapid "new" Method for Determining NMR Spin-Lattice Times. J Magn Reson 1985;63:287-297.

48. Wang HZ, Riederer SJ, Lee JN. Optimizing the precision in T1 relaxation estimation using limited flip angles. Magn Reson Med 1987;5(5):399-416.

49. Deoni SC, Rutt BK, Peters TM. Rapid combined T1 and T2 mapping using gradient recalled acquisition in the steady state. Magn Reson Med 2003;49(3):515-526.

50. Deoni SC, Peters TM, Rutt BK. Determination of optimal angles for variable nutation proton magnetic spin-lattice, T1, and spin-spin, T2, relaxation times measurement. Magn Reson Med 2004;51(1):194-199.

51. Schabel MC, Morrell GR. Uncertainty in T(1) mapping using the variable flip angle method with two flip angles. Phys Med Biol 2009;54(1):N1-8.

52. Cunningham CH, Pauly JM, Nayak KS. Saturated double-angle method for rapid B1+ mapping. Magn Reson Med 2006;55(6):1326-1333.

53. Insko EK, Bolinger L. Mapping of Radiology Field. J Magn Reson 1993;103:82-85.

54. Stollberger Rudolf, Paul W. Imaging of the Active B1 Field in Vivo. Magnetic Resonance in Medicine 2005;35(2):246-251.

55. Wang J, Qiu M, Constable RT. In vivo method for correcting transmit/receive nonuniformities with phased array coils. Magn Reson Med 2005;53(3):666-674.

56. Hornak JP, Szumowski J, Bryant RG. Magnetic field mapping. Magn Reson Med 1988;6(2):158-163.

57. Dowel NG, Tofts PS. Fast, accurate, and precise mapping of the RF field in vivo using the 180 signal null. . Magn Reson Med 2007;58:622-630.

58. Morrell GR. A phase-sensitive method of flip angle mapping. Magn Reson Med 2008;60(4):889-894.

59. Yarnykh VL. Actual flip-angle imaging in the pulsed steady state: a method for rapid three-dimensional mapping of the transmitted radiofrequency field. Magn Reson Med 2007;57(1):192-200.

60. Ishihara Y, Calderon A, Watanabe H, Okamoto K, Suzuki Y, Kuroda K. A precise and fast temperature mapping using water proton chemical shift. Magn Reson Med 1995;34(6):814-823.

61. Muller N, RC R. Temperature dependence of chemical shifts of protons in hydrogen bonds. Journal of Chemical Physics 1965;42:3265-3269.

62. Vogel MW, Pattynama PM, Lethimonnier FL, Le Roux P. Use of fast spin echo for phase shift magnetic resonance thermometry. J Magn Reson Imaging 2003;18(4):507-512.

63. Gudbjartsson H, Patz S. The Rician distribution of noisy MRI data. Magn Reson Med 1995;34(6):910-914.

64. Pelc NJ, Bernstein MA, Shimakawa A, Glover GH. Encoding strategies for three-direction phase-contrast MR imaging of flow. J Magn Reson Imaging 1991;1(4):405-413.

65. Kuroda K, Mulkern RV, Oshio K, Panych LP, Nakai T, Moriya T, Okuda S, Hynynen K, Jolesz FA. Temperature mapping using the water proton chemical shift: self-referenced method with echo-planar spectroscopic imaging. Magn Reson Med 2000;44(1):167.

66. Cline HE, Hynynen K, Schneider E, Hardy CJ, Maier SE, Watkins RD, Jolesz FA. Simultaneous magnetic resonance phase and magnitude temperature maps in muscle. Magn Reson Med 1996;35(3):309-315.

67. Chung AH, Hynynen K, Colucci V, Oshio K, Cline HE, Jolesz FA. Optimization of spoiled gradient-echo phase imaging for in vivo localization of a focused ultrasound beam. Magn Reson Med 1996;36(5):745-752.

68. Ghiglia DC, MD P. Two-Dimensinal Phase Unwrapping Theory, Algorithms, and Softwares. USA: John WILEY & SON, INC 1998.

69. De Poorter, De Wagter C, De Deene Y, Thomsen C, Stahlberg F, E. A. The proton-resonance-frequency-shift method compared with molecular-diffusion for quantitative measurement of 2-dimensional time-dependent temperature distribution in a phantom. Journal of Magnetic Resonance Series B 1994(103):234-241.

70. Bohris C, Schreiber WG, Jenne J, Simiantonakis I, Rastert R, Zabel HJ, Huber P, Bader R, Brix G. Quantitative MR temperature monitoring of high-intensity focused ultrasound therapy. Magn Reson Imaging 1999;17(4):603-610.

71. Yamada N, Imakita S, Sakuma T, Nishimura Y, Yamada Y, Naito H, Nishimura T, Takamiya M. Evaluation of the susceptibility effect on the phase images of a simple gradient echo. Radiology 1990;175(2):561-565.

72. Sprinkhuizen SM, Bakker CJ, Ippel JH, Boelens R, Viergever MA, Bartels LW. Temperature dependence of the magnetic volume susceptibility of human breast fat tissue: an NMR study. MAGMA 2012;25(1):33-39.

73. Stollberger R, Ascher PW, Huber D, Renhart W, Radner H, Ebner F. Temperature monitoring of interstitial thermal tissue coagulation using MR phase images. J Magn Reson Imaging 1998;8(1):188-196.

74. Young IR, Hajnal JV, Roberts IG, Ling JX, Hill-Cottingham RJ, Oatridge A, Wilson JA. An evaluation of the effects of susceptibility changes on the water chemical shift method of temperature measurement in human peripheral muscle. Magn Reson Med 1996;36(3):366-374.

75. Robert D. P, R. Scott Hinks, Henkelman RM. Heat-source orientation and geometry dependence in proton-resonance frequency shift magnetic resonance thermometry. Magnetic Resonance in Medecine 1999;41:909-918.

76. Korin HW, Ehman RL, Riederer SJ, Felmlee JP, Grimm RC. Respiratory kinematics of the upper abdominal organs: a quantitative study. Magn Reson Med 1992;23(1):172-178.

77. Salomir R, Palussiere J, Grenier N, Dumont E, Quesson B, C. M. Local hyperthermia with focus ultrasound (FUS) or interstitial laser applicator (LITT) under PRF-based MR-Temperature monitoring in the living kidney of the rabbit. Proceedings 10th ISMRM. Honolulu, Hawaii2002. p 2202.

78. Morikawa S, Inubushi T, Kurumi Y, Naka S, Seshan V, T T. Feasibility of simple respiratory triggering in MR-guided interventional procedures for liver tumors under general anesthesia. Proceedings 10th ISMRM. Honolulu, Hawaii2002. p 2240.

79. Rieke V, Vigen KK, Sommer G, Daniel BL, Pauly JM, Butts K. Referenceless PRF shift thermometry. Magn Reson Med 2004;51(6):1223-1231.

80. Thomsen S. Pathologic analysis of photothermal and photomechanical effects of laser-tissue interactions. Photochem Photobiol 1991;53(6):825-835.

81. Daniel BL. Intraprocedural magnetic resonance imaging-guided interventions in the breast. Top Magn Reson Imaging 2000;11(3):184-190.

82. Kamimura Y, Y A. An NMR technique for non-invasive thermometry using M0 as temperature-sensitive parameter. Automedica 1987;8:295-313.

83. MacFall J, Prescott DM, Fullar E, Samulski TV. Temperature dependence of canine brain tissue diffusion coefficient measured in vivo with magnetic resonance echo-planar imaging. Int J Hyperthermia 1995;11(1):73-86.

84. Samulski TV, MacFall J, Zhang Y, Grant W, Charles C. Non-invasive thermometry using magnetic resonance diffusion imaging: potential for application in hyperthermic oncology. Int J Hyperthermia 1992;8(6):819-829.

85. Delannoy J, Chen CN, Turner R, Levin RL, Le Bihan D. Noninvasive temperature imaging using diffusion MRI. Magn Reson Med 1991;19(2):333-339.

86. Hall AS, Prior MV, Hand JW, Young IR, Dickinson RJ. Observation by MR imaging of in vivo temperature changes induced by radio frequency hyperthermia. J Comput Assist Tomogr 1990;14(3):430-436.

87. Bleier AR, Jolesz FA, Cohen MS, Weisskoff RM, Dalcanton JJ, Higuchi N, Feinberg DA, Rosen BR, McKinstry RC, Hushek SG. Real-time magnetic resonance imaging of laser heat deposition in tissue. Magn Reson Med 1991;21(1):132-137.

88. Wolff SD, Balaban RS. Magnetization transfer contrast (MTC) and tissue water proton relaxation in vivo. Magn Reson Med 1989;10(1):135-144.

89. Henkelman RM, Stanisz GJ, Graham SJ. Magnetization transfer in MRI: a review. NMR Biomed 2001;14(2):57-64

90. Parker DL, Buswell HR, Goodrich KC, Alexander AL, Keck N, Tsuruda JS. The application of magnetization transfer to MR angiography with reduced total power. Magn Reson Med 1995;34(2):283-286.

91. Petrella JR, Grossman RI, McGowan JC, Campbell G, Cohen JA. Multiple sclerosis lesions: relationship between MR enhancement pattern and magnetization transfer effect. AJNR Am J Neuroradiol 1996;17(6):1041-1049.

92. Silver NC, Lai M, Symms MR, Barker GJ, McDonald WI, Miller DH. Serial magnetization transfer imaging to characterize the early evolution of new MS lesions. Neurology 1998;51(3):758-764.

93. van Buchem MA, Grossman RI, Armstrong C, Polansky M, Miki Y, Heyning FH, Boncoeur-Martel MP, Wei L, Udupa JK, Grossman M, Kolson DL, McGowan JC. Correlation of volumetric magnetization transfer imaging with clinical data in MS. Neurology 1998;50(6):1609-1617.

94. Lindstrom P.A. Prefrontal ultrasonic irradiation-a substitute for lobotomy. AMA Arch Neurol Psychiatry 1954;72(4):399-425.

95. Fry WJ, Barnard JW, Fry EJ, Krumins RF, Brennan JF. Ultrasonic lesions in the mammalian central nervous system. Science 1955;122(3168):517-518.

96. Hynynen K, Lulu BA. Hyperthermia in cancer treatment. Invest Radiol 1990;25(7):824-834.

97. Sanghvi NT, Foster RS, Bihrle R, Casey R, Uchida T, Phillips MH, Syrus J, Zaitsev AV, Marich KW, Fry FJ. Noninvasive surgery of prostate tissue by high intensity focused ultrasound: an updated report. Eur J Ultrasound 1999;9(1):19-29.

98. Wu J, W N. Emerging therapeudic ultrasound. Word Scientific Publishing CoPteLtd 2006.

99. Bamber JC, Hill CR. Ultrasonic attenuation and propagation speed in mammalian tissues as a function of temperature. Ultrasound Med Biol 1979;5(2):149-157.

100. Hedrick W, Hykes D, D S. Ultrasound Physics and Instrumentation. Edition F, editor: Elsevier Mosby; 2005. 48-49 p.

101. Goss SA, Frizzell LA, Dunn F. Ultrasonic absorption and attenuation in mammalian tissues. Ultrasound Med Biol 1979;5(2):181-186.

102. Bernstein M, King K, X Z. Handbook of MRI, Pulse Sequence. Amsterdam: Elsevier Inc;2004.

103. Bottomley PA. Turning up the heat on MRI. J Am Coll Radiol 2008;5(7):853-855.

104. Wlodarczyk W, Hentschel M, Wust P, Noeske R, Hosten N, Rinneberg H, Felix R. Comparison of four magnetic resonance methods for mapping small temperature changes. Phys Med Biol 1999;44(2):607-624.

105. Peters RD, Hinks RS, Henkelman RM. Ex vivo tissue-type independence in proton-resonance frequency shift MR thermometry. Magn Reson Med 1998;40(3):454-459.

106. Carr H, E P. Effect of diffusion on free precession in nuclear magnetic resonance experiments. Phys Rev 1954;94:630-638.

107. Le Roux P. Non-CPMG Fast Spin Echo with full signal. J Magn Reson 2002;155(2):278-292.

108. Slichter C.P. Principle of Magnetic Resonance. New York: Springer-Verlag; 1990. 367 p.

109. Och JG, Clarke GD, Sobol WT, Rosen CW, Mun SK. Acceptance testing of magnetic resonance imaging systems: report of AAPM Nuclear Magnetic Resonance Task Group No. 6. Med Phys 1992;19(1):217-229.

110. Peters RD, Henkelman RM. Proton-resonance frequency shift MR thermometry is affected by changes in the electrical conductivity of tissue. Magn Reson Med 2000;43(1):62-71.

111. Conturo TE, Smith GD. Signal-to-noise in phase angle reconstruction: dynamic range extension using phase reference offsets. Magn Reson Med 1990;15(3):420-437.

112. Hill CR, Bamber JC, Ter Haar GR. Physical Principles of Medical Ultrasonics. Willey, editor. Chichester, U.K2004.

113. Kremkau FW. Cancer therapy with ultrasound: a historical review. J Clin Ultrasound 1979;7(4):287-300.

114. Dickinson RJ, Hall AS, Hind AJ, Young IR. Measurement of changes in tissue temperature using MR imaging. J Comput Assist Tomogr 1986;10(3):468-472.

115. Hynynen K, Vykhodtseva NI, Chung AH, Sorrentino V, Colucci V, Jolesz FA. Thermal effects of focused ultrasound on the brain: determination with MR imaging. Radiology 1997;204(1):247-253.

116. McDannold NJ, King RL, Jolesz FA, Hynynen KH. Usefulness of MR imaging-derived thermometry and dosimetry in determining the threshold for tissue damage induced by thermal surgery in rabbits. Radiology 2000;216(2):517-523.

117. Anzai Y, Lufkin RB, Castro DJ, Farahani K, Jabour BA, Layfield LJ, Udkoff R, Hanafee WN. MR imaging-guided interstitial Nd:YAG laser phototherapy: dosimetry study of acute tissue damage in an in vivo model. J Magn Reson Imaging 1991;1(5):553-559.

118. Carstensen EL, Becroft SA, Law WK, Barbee DB. Finite amplitude effects on the thresholds for lesion production in tissues by unfocussed ultrasound. J Acoust Soc Am 1981;70:302-309.

119. Dunn F, Fry FJ. Ultrasonic threshold dosages for the mammalian central nervous system. IEEE Trans Biomed Eng 1971;18(4):253-256.

120. Dunn F, Lohnes JE, Fry FJ. Frequency dependence of threshold ultrasonic dosages for irreversible structural changes in mammalian brain. J Acoust Soc Am 1975;58(2):512-514.

121. Fry FJ, Kossoff G, Eggleton RC, Dunn F. Threshold ultrasonic dosages for structural changes in the mammalian brain. J Acoust Soc Am 1970;48(6):Suppl 2:1413+.

122. Robinson TC, Lele PP. An analysis of lesion development in the brain and in plastics by high-intensity focused ultrasound at low-megahertz frequencies. J Acoust Soc Am 1972;51(4):1333-1351.

123. Sapareto SA, Dewey WC. Thermal dose determination in cancer therapy. Int J Radiat Oncol Biol Phys 1984;10(6):787-800.

124. Cheng KH, Hernandez M. Magnetic resonance diffusion imaging detects structural damage in biological tissues upon hyperthermia. Cancer Res 1992;52(21):6066-6073.

125. Damianou C, Hynynen K. The effect of various physical parameters on the size and shape of necrosed tissue volume during ultrasound surgery. J Acoust Soc Am 1994;95(3):1641-1649.

126. Kuroda k, Abe K, Tsutsumi S, Ishihara Y, Suzuki Y, Sato K. Water proton magetic resonance spectroscopic imaging. Advanced techniques and clinical applications in biomedical thermology. Chur,. Switzerland: Harwood Academic Publishers1993.

127. Morrell GR, Schabel MC. An analysis of the accuracy of magnetic resonance flip angle measurement methods. Phys Med Biol 2010;55(20):6157-6174.

128. Kamman RL, Go KG, Brouwer W, Berendsen HJ. Nuclear magnetic resonance relaxation in experimental brain edema: effects of water concentration, protein concentration, and temperature. Magn Reson Med 1988;6(3):265-274.

129. Meshorer A, Prionas SD, Fajardo LF, Meyer JL, Hahn GM, Martinez AA. The effects of hyperthermia on normal mesenchymal tissues. Application of a histologic grading system. Arch Pathol Lab Med 1983;107(6):328-334.

130. Arora D, Skliar M, Roemer RB. Minimum-time thermal dose control of thermal therapies. IEEE Trans Biomed Eng 2005;52(2):191-200.

131. Damianou C, Hynynen K, Fan X. Evaluation of accuracy of a theoretical mode for predicting the necrosed tissue volume during focused ultrasound surgery. IEEE Trans Ultrason Ferroelectrics Freq Control 1995;42:182-187.

132. Dewey WC. Arrhenius relationships from the molecule and cell to the clinic. Int J Hyperthermia 1994;10(4):457-483.

133. Bernstein MA, Grgic M, Brosnan TJ, Pelc NJ. Reconstructions of phase contrast, phased array multicoil data. Magn Reson Med 1994;32(3):330-334.

134. MacFall JR, Prescott DM, Charles HC, Samulski TV. 1H MRI phase thermometry in vivo in canine brain, muscle, and tumor tissue. Med Phys 1996;23(10):1775-1782.

135. Chung AH, Jolesz FA, Hynynen K. Thermal dosimetry of a focused ultrasound beam in vivo by magnetic resonance imaging. Med Phys 1999;26(9):2017-2026.

136. McDannold, Hynynen K, Wolf D, Wolf G, Jolesz F. MRI evaluation of thermal ablation of tumors with focused ultrasound. J Magn Reson Imaging 1998;8(1):91-100.

137. Mathur-De Vre R. Biomedical implications of the relaxation behaviour of water related to NMR imaging. British J Radiol 1984;57:955-976.

138. Kuroda K OK, Mulkern RV, Jolesz FA,. Optimization of Chemical Shift Selective Suppression of Fat. Magnetic Resonance in Medecine 1996;40:505-510.

139. Vandeweyer E, Hertens D. Quantification of glands and fat in breast tissue: an experimental determination. Ann Anat 2002;184(2):181-184.

140. Dimitrov IE, Douglas D, Ren J, Smith NB, Webb AG, Sherry AD, Malloy CR. In vivo determination of human breast fat composition by ^{1}H magnetic resonance spectroscopy at 7 T. Magn Reson Med 2012;67(1):20-26.

141. Skinner TE, Glover GH. An extended two-point Dixon algorithm for calculating separate water, fat, and B0 images. Magn Reson Med 1997;37(4):628-630.

142. Cusack R, Papadakis N. New robust 3-D phase unwrapping algorithms: application to magnetic field mapping and undistorting echoplanar images. Neuroimage 2002;16(3 Pt 1):754-764

143. Melhem ER, Jara H, Shakir H, Gagliano TA. Fast inversion-recovery MR: the effect of hybrid RARE readout on the null points of fat and cerebrospinal fluid. AJNR Am J Neuroradiol 1997;18(9):1627-1633.

144. Stafford RJ, Price RE, Diederich CJ, Kangasniemi M, Olsson LE, Hazle JD. Interleaved echo-planar imaging for fast multiplanar magnetic resonance temperature imaging of ultrasound thermal ablation therapy. J Magn Reson Imaging 2004;20(4):706-714.

145. de Zwart JA, van Gelderen P, Kelly DJ, Moonen CT. Fast magnetic-resonance temperature imaging. J Magn Reson B 1996;112(1):86-90.

146. Oros-Peusquens AM, Laurila M, Shah NJ. Magnetic field dependence of the distribution of NMR relaxation times in the living human brain. MAGMA 2008;21(1-2):131-147.

147. Roemer PB, Edelstein WA, Hayes CE, Souza SP, Mueller OM. The NMR phased array. Magn Reson Med 1990;16(2):192-225.

148. Senneville B RM, Bartels LW, Moonen CW. MRI-Guided High-Intensity Focused Ultrasound Sonication of Liver and Kidney. Interventional Magnetic Resonance Imaging 2011:p.349-366.

149. Blaimer M, Breuer F, Mueller M, Heidemann RM, Griswold MA, Jakob PM. SMASH, SENSE, PILS, GRAPPA: how to choose the optimal method. Top Magn Reson Imaging 2004;15(4):223-236.

150. Blaimer M, Breuer FA, Mueller M, Seiberlich N, Ebel D, Heidemann RM, Griswold MA, Jakob PM. 2D-GRAPPA-operator for faster 3D parallel MRI. Magn Reson Med 2006;56(6):1359-1364.

151. Blaimer M, Breuer FA, Seiberlich N, Mueller MF, Heidemann RM, Jellus V, Wiggins G, Wald LL, Griswold MA, Jakob PM. Accelerated volumetric MRI with a SENSE/GRAPPA combination. J Magn Reson Imaging 2006;24(2):444-450.

152. Deoni SC, Peters TM, Rutt BK. High-resolution T1 and T2 mapping of the brain in a clinically acceptable time with DESPOT1 and DESPOT2. Magn Reson Med 2005;53(1):237-241.

153. Pauly P LRP, Nishimura D, Macovski A. Parameter Relations for the Shinnar-Le Roux Selective Excitation Pulse Design Algorithm IEEE Trans Med Imag 1991;10:53-65.

154. Balezeau F, Eliat PA, Cayamo AB, Saint-Jalmes H. Mapping of low flip angles in magnetic resonance. Phys Med Biol 2011;56(20):6635-6647.